Protein Dynamics in Cytochrome b_6f Explored by Spectral Hole Burning

Golia Shafiei

A Thesis
In
The Department
of
Physics

Presented in Partial Fulfillment of the Requirements
for the Degree of Master of Science (Physics) at
Concordia University
Montréal, Québec, Canada

March 2016

CONCORDIA UNIVERSITY

School of Graduate Studies

This is to certify that the thesis prepared

By: Golia Shafiei

Entitled: Protein Dynamics in Cytochrome b_6f Explored by Spectral Hole Burning

and submitted in partial fulfillment of the requirements for the degree of

Master of Physics

complies with the regulations of this University and meets the accepted standards with respect to originality and quality.

Signed by the final examining commitee:

_____ Chair
Dr. Barry Frank

_____ Examiner
Dr. Laszlo Kalman

_____ Examiner
Dr. Pablo Bianucci

_____ Supervisor
Dr. Valter Zazubovits

Approved _____
Chair of Department or Graduate Program Director

_____ 2016 _____

André Roy, Dean
Faculty of Arts and Sciences

ABSTRACT

Protein Dynamics in Cytochrome b_6f Explored by
Spectral Hole Burning

Golia Shafiei

Proteins are very important biomolecules that perform vital functions in the living organisms. Proteins need to fold into their final tertiary structure in order to function properly. However, knowing the static tertiary structure of a protein is not enough to understand how it functions since proteins are not rigid bodies. The fact that the proteins go through structural fluctuations has to be taken into account in studying these complex biomolecules. Optical techniques, such as spectral hole burning, can be used in studying the dynamics of proteins. However, most proteins must be doped with dye molecules as probes since most of the proteins do not absorb light in visible region. Pigment-protein complexes involved in photosynthesis process are good options for studying protein dynamics. The pigment molecules are embedded in these proteins naturally. Understanding the dynamics of proteins involved in photosynthesis and the way they function is important from the perspective of photosynthesis research and renewable energy. The focus of this study is on the dynamics and the barrier distributions on the energy landscape of Cytochrome b_6f Protein Complex at low temperatures. Qualitatively, the distributions of barriers between protein sub-states involved in the light-induced conformational changes (i.e. - Non-Photochemical Hole Burning (NPHB)) are close to glass-like $\backsim 1/\sqrt{V}$ (V is the barrier height), and not to Gaussian. Spectral dynamics of Cytochrome b_6f manifesting in NPHB experiments appears to be independent of the deuteration of the buffer/glycerol glassy matrix containing the protein. Two plausible explanations for this dynamics remain. The observed dynamics can be the genuine protein dynamics, despite the $\backsim 1/\sqrt{V}$ shape of barrier distributions. Alternatively, the chlorophylls may be sensing the dynamics of water/glycerol outside environment, involving specifically the tunneling of the whole -OH groups. Proton tunneling in the water/glycerol solvent environment can be excluded as the origin of the observed NPHB and recovery dynamics. Entities involved in the light-induced conformational changes are characterized by $md^2 \backsim$ 2.7-3.6 $\times\ 10^{-46}\ kg{\cdot}\mathrm{m}^2$. Evidence is presented for excitation energy transfer between chlorophyll molecules of the adjacent monomers. The magnitude of the dipole-dipole coupling deduced from the Δ-FLN spectra is in good agreement with the structural data, indicating that explored protein was intact.

Acknowledgements

First and foremost, I would like to express my deepest gratitude to my supervisor, Dr. Valter Zazubovits, for his guidance, support and patience. Thank you for not only guiding me knowledgeably through my research, but also for being so helpful, nice and understanding throughout my studies in Concordia University.

I would like to thank Dr. Laszlo Kalman for his kind support and guidance during my studies in Concordia University, and for kindly letting me use his research laboratory whenever I needed to. I am also extremely grateful to my committee members, Dr. Laszlo Kalman and Dr. Pablo Bianucci, for their assistance and time.

My special thanks to all my fellow graduate students, office mates and colleagues for making my experience at Concordia University pleasant and for the support and help they have provided.

Thanks to my parents and brother for their care and encouragements throughout my whole life. I extremely appreciate your kindness, love and support in all stages of my life.

Last, but not the least, I would like to say a heartfelt thank to my husband and best friend, Pooya, for his constant support and endless love. Thank you for always being there for me and for believing in me all the time.

Contents

List of Figures

List of Tables

Abbreviations

Chl	**Chl**orophyll
Cyt	**Cyt**ochrome
HB	**H**ole **B**urning
HGK	**H**ole **G**rowth **K**inetics
HR	**H**ole **R**ecovery
FLN	**F**luorescence **L**ine **N**arrowing
NPHB	**N**on-**P**hotochemical **H**ole **B**urning
PHB	**P**hotochemical **H**ole **B**urning
PSI	**P**hotosystem **I**
PSII	**P**hotosysthem **II**
PSB	**P**honon **S**ide **B**and
PSBH	**P**honon **S**ide **B**and **H**ole
RC	**R**eaction **C**enter
SDF	**S**ite **D**istribution **F**unction
SHB	**S**pectral **H**ole **B**urning
SSA	**S**ingle **S**ite **A**bsorption
TLS	**T**wo **L**evel **S**ystem
ZPH	**Z**ero **P**honon **H**ole
ZPL	**Z**ero **P**honon **L**ine

Chapter 1

Introduction

Proteins are important biomolecules that perform vital functions in the living organisms. Proteins are functional when they are folded into their final tertiary structure. The static tertiary structure of a protein can be determined by means of different methods such as X-ray diffraction or Nuclear Magnetic Resonance (NMR) Spectroscopy. However, knowing the static tertiary structure of a protein is not enough to understand how it functions since proteins are *dynamic* systems rather than rigid bodies. A specific protein may have to fluctuate between its various conformational states in order to be functional. Therefore, these structural fluctuations has to be taken into account, as well as the tertiary structure, in studying these complex biomolecules and their functions. The protein dynamics and the balance between structural order and disorder are reflected in the *Energy Landscape* of a protein [1]. The energy landscape of a protein includes the energy minima corresponding to the conformational substates and the separating barriers between those.

Optical techniques, such as spectral hole burning, can be used in studying the dynamics of proteins at low temperatures since the fluctuations in the structure of condensed phases of matter affect the resonance frequencies of optical transitions of optical centers in the solid [1]. In other

words, the fluctuations of the energy landscape of proteins are reflected in the spectroscopic measurements.

However, most proteins are not suitable for optical studies at first place since they do not absorb light in visible region. In these cases, the proteins must be artificially doped with dye molecules as the optical centers. The downside of this approach is that the dynamics observed in these artificially doped proteins might not be completely correct since the original structure of the protein might have been modified as a result of chemical manipulations and doping. Alternatively, pigment-protein complexes involved in photosynthesis process are good candidates for studying protein dynamics. The pigment molecules (Chlorophylls) are naturally embedded in the protein complexes involved in photosynthesis process. Therefore, one can be sure that the observed dynamics are not the results of artificial modifications introduced to the protein structure. In addition, understanding the dynamics of proteins involved in photosynthesis and the way they function is important from the perspective of photosynthesis research and renewable energy since the photosynthetic protein complexes are involved in the whole photosynthesis process from capturing the light energy to converting it to the chemical energy. The exact transition energies of chlorophylls in those complexes depend on the structure (and dynamics) of the respective protein pockets.

In general, proteins are structurally disordered and as a result, their absorption spectra are inhomogeneously broadened. In order to study the protein dynamics, one has to overcome the problem with the inhomogeneous broadening of the absorption spectrum. Optical line narrowing techniques, such as spectral hole burning (SHB), can be used for this purpose.

In spectral hole burning, narrow band lasers (to eliminate the inhomogeneous broadening effect) are used for exciting only a fraction of molecules of the protein sample that are in resonance with the laser frequency. This is called the hole burning process. As a result of hole burning, the resonant molecules stop absorbing photons at the laser/burning frequency and a hole occurs

in the absorption spectrum of the sample. The way the hole growth and its shape, width and area change as well as the way the hole recovers as a function of time and temperature contain useful information about the dynamics and energy landscape of the protein.

In this study, we focus on the dynamics and the barrier distributions on the energy landscape of Cytochrome b_6f Complex, a protein involved in photosynthesis process, at low temperatures. We employed non-photochemical hole burning (NPHB) technique for these purposes.

Chapter 2 includes an overview of photosynthesis process and the protein complexes involved in it. A brief description of protein dynamics and protein energy landscape is provided in Chapter 3. Then, the methods used in studying the protein energy landscape, such as Spectral Hole Burning, and the theory behind these methods are described in Chapter 4. Finally, the experimental results obtained for the Cytochrome b_6f protein complex along with the discussion and the concluding remarks are presented in Chapter 5. The last chapter, Chapter 6, is dedicated to the conclusion of this study and the possible future research.

Chapter 2

Photosynthetic Protein Complexes

Photosynthesis is a biological process that has been used by nature for the past 3.5 billion years to make life possible on Earth. Photosynthesis provides food and oxygen required to maintain life, by converting solar energy to chemical energy. This process has several steps and proteins play a vital role in these steps. This chapter is an introduction to the photosynthesis process, and to some protein complexes that are involved in this process.

2.1 Photosynthesis

There are two main varieties of photosynthesis: Oxygenic Photosynthesis and Anoxygenic Photosynthesis [2]. The main difference between these two different types is that oxygen is not a product of anoxygenic photosynthesis and water is not used as an electron donor in this process. However, the details of anoxygenic photosynthesis are not provided in this thesis since the focus of this study is on a protein originating from organisms involved in oxygenic photosynthesis.

Oxygenic Photosynthesis is used by nature to produce various organic compounds such as sugars, with oxygen as an important by-product. During this process, the light energy from the

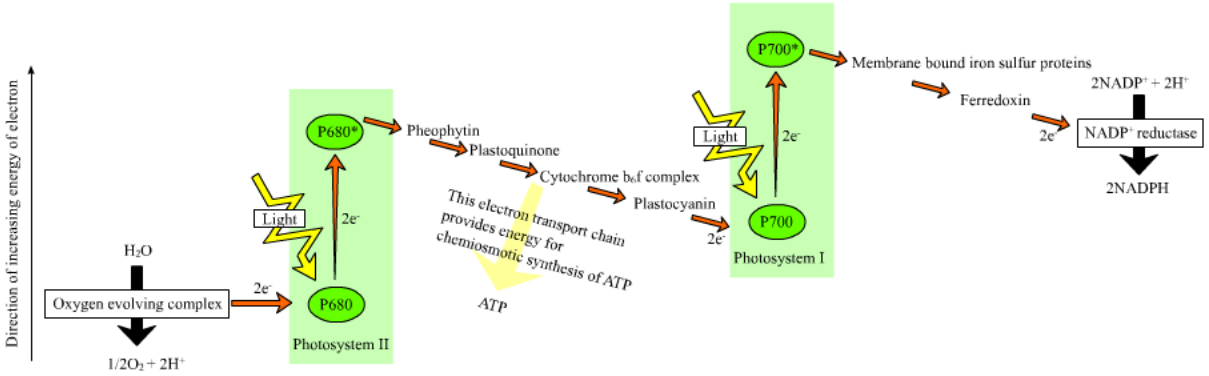

FIGURE 2.1: Z-Scheme of Photosynthesis Process [3] - During the photosynthesis process, light energy is absorbed by PSII and is used to transfer electrons across the membrane. The electrons are obtained from water, which is split into protons and oxygen. The electrons are transported, via Cytochrome b_6f complex, to PSI. The latter again absorbs light, and light energy is used for charge separation. Eventually, electrons are used in the synthesis of NADPH. Proton gradient is used to synthesize ATP. Finally, ATP and NADPH are used to power synthesis of sugars from CO_2.

Sun is absorbed by the pigment (e.g. a chlorophyll) in the antenna complex and is transferred to the photosynthetic reaction center. Chlorophyll *a* and *b* are the pigments that are in charge of the initial photon absorption in plants, algae and cyanobacteria. The absorbed energy is used to transfer electrons through the membrane and between two main photosynthetic complexes, called Photosystem II and Photosystem I, and is converted to chemical energy [2]. The details of this process is shown in the so called Z-Scheme in Figure 2.1 [3].

The oxygenic photosynthesis happens in two stages of "Light" and "Dark" reactions. Light reactions start with photon absorption. The energy absorbed by antenna chlorophylls is transferred to the reaction center. The charge separation starts from the primary electron donor (P680) in the reaction center of PSII. This creates the redox potential of 1.1 V that is enough to split water. The required electrons for the oxygenic photosynthesis are provided by water when it is split into oxygen and hydrogen (protons). The electrons are transferred from P680 to pheophytin (the primary electron acceptor molecule) to quinones within PSII complex, and then to PSI through the electron transfer chain and Cytochrome b_6f complex. Finally, the $NADP^+$ is reduced to NADPH in Photosystem I. Also, the proton gradient created in previous steps is used to drive the high energy molecule ATP (adenosine triphosphate) synthesis. The

dark reactions take place after the production of NADPH and ATP molecules. During the dark reactions, these molecules are used with CO_2 to produce carbohydrates and glucose through the Calvin cycle [2].

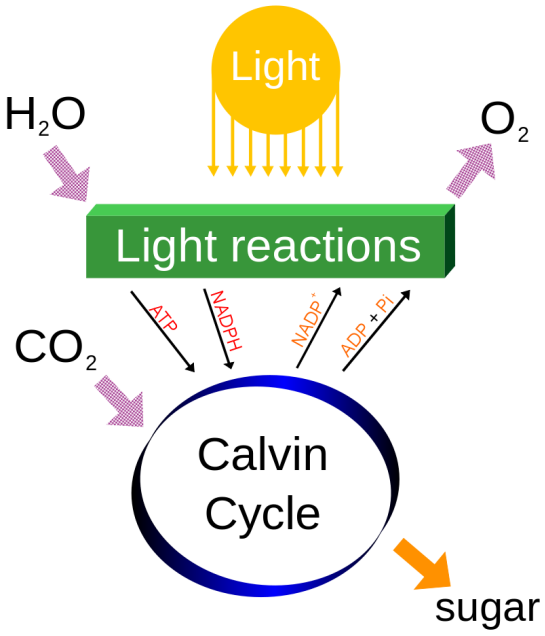

FIGURE 2.2: Photosynthesis converts sunlight into chemical energy and provides O_2 and sugar. [4]

A simple schematic of oxygenic photosynthesis process is shown in Figure 2.2. The main source of the food and the oxygen, both essential for maintaining life on Earth, are the products of oxygenic photosynthesis. Without this process, it would not be possible to live on Earth.

2.2 Chlorophyll

Chlorophyll is a vital molecule and it is essential for photosynthesis. Plants can absorb light energy from the Sun by means of this biomolecule. Tissues containing chlorophyll have green color since chlorophyll does not absorb the green portion of electromagnetic spectrum. However, this molecule is an extremely strong absorber of light in the blue and red portions of the

spectrum [5]. Chlorophyll *a* and Chlorophyll *b* are the two common types of chlorophyll found in plants. These chlorophylls exist in photosystems located in the thylakoid membranes of chloroplasts. Chl *b* absorbs at shorter wavelengths than Chl *a* and energy absorbed by Chl b is transferred to Chl a (this difference is due to internal properties of the molecules, that are slightly different, as discussed below). Additionally, the spectral properties of chlorophyll molecules are fine-tuned by the protein environment.

2.2.1 Chlorophyll a

Chlorophyll *a* is the most common pigment that exists in photosynthetic organisms and it is the specific form of chlorophyll used in oxygenic photosynthesis. The molecular structure of chlorophyll *a* is shown in Figure 2.3. This structure consists of a chlorin ring, with a magnesium ion in its center which is surrounded by four nitrogen atoms. The chlorin ring is attached to a long hydrocarbon tail.

The absorption spectrum of chlorophyll *a* in diethyl ether solution peaks at two wavelengths of 430 nm (violet-blue portion of visible light) and 662 nm (red portion of visible light). The range of wavelengths that can be used by plants to absorb light energy in photosynthesis is usually increased because of the existence of accessory photosynthetic pigments. The accessory pigments, such as chlorophyll *b* and carotenoids, absorb light in a slightly different wavelengths than chlorophyll *a*.

2.2.2 Chlorophyll b

Chlorophyll *b* is the other common type of chlorophyll that exists in photosynthetic organisms. As mentioned before, Chlorophyll *a* is used in all oxygenic photosynthetic systems. However, Chlorophyll *b* is considered an accessory pigment in oxygenic photosynthesis. The molecular

structure of chlorophyll b is shown in Figure 2.3. This structure is slightly different than the structure of chlorophyll a (the methyl group (CH_3) is substituted by aldehyde group (CHO)).

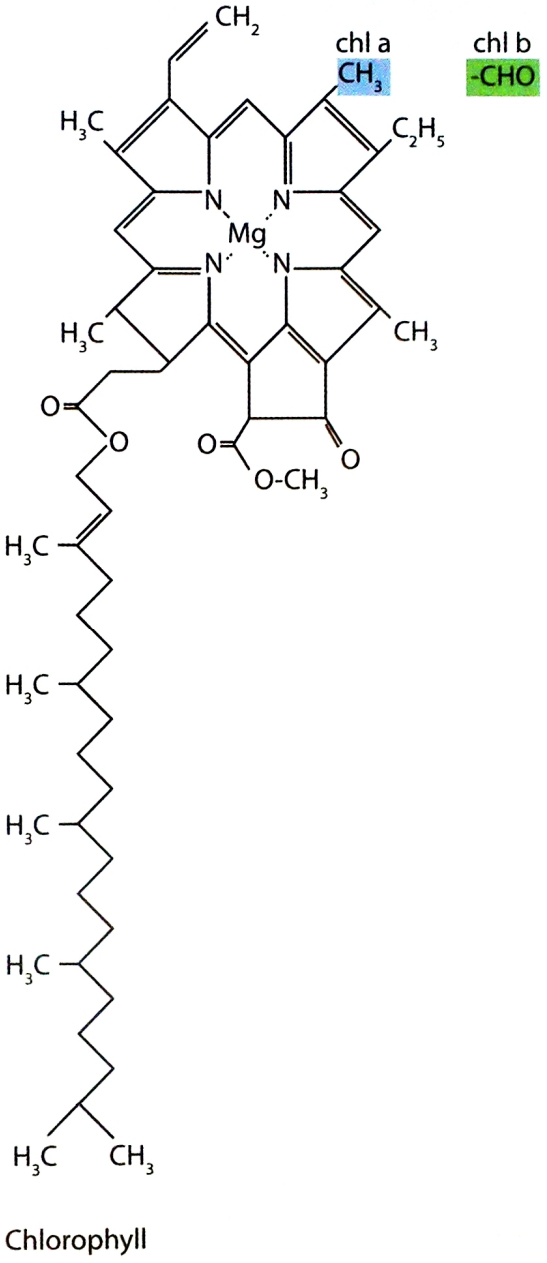

FIGURE 2.3: Molecular Structure of Chlorophyll *a* and *b*. The structures of Chlorophyll *a* (blue highlight) and *b* (green highlight) are similar. The the methyl group (CH_3) in the structure of Chl *a* is substituted by aldehyde group (CHO) in the structure of Chl *b* [6].

The absorption spectrum of Chlorophyll *b* in diethyl ether has two peaks at 453 nm and 642 nm which are close to the peaks of absorption spectrum of Chlorophyll *a*. The slight difference

in the absorption spectra of Chlorophyll a and b extends the total absorption spectrum of light in oxygenic photosynthetic process. The absorption spectra of chlorophyll a and b are shown in Figure 2.4.

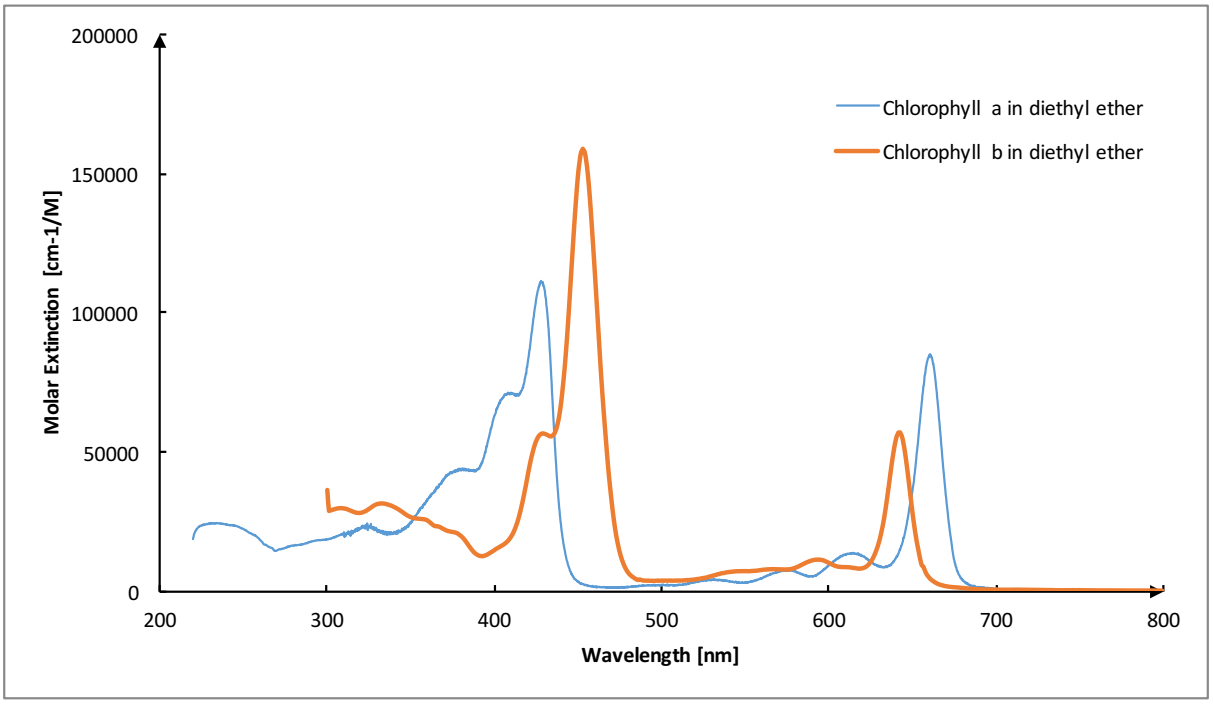

FIGURE 2.4: The absorption spectra of Chlorophyll a and b in diethyl ether [7]

2.3 Protein Complexes of Oxygenic Photosynthesis

Membrane proteins are responsible for most of the light reactions in photosynthesis [2]. Determining the structure and dynamics of these proteins is vital to understand the photosynthesis process completely. Figure 2.5 shows the relationship between different proteins involved in the light reactions and the electron transfer chain in oxygenic photosynthesis. Among these protein complexes, Photosystem II, Photosystem I and Cytochrome b_6f Complex are introduced in this section.

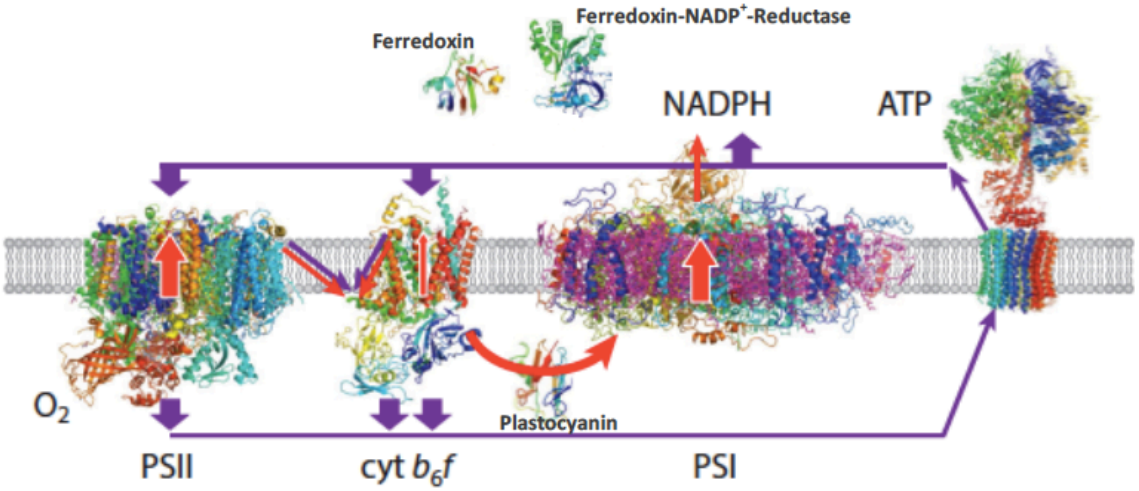

FIGURE 2.5: Electron and proton transfer in oxygenic photosynthesis. Electron transfer (red arrows) and proton transfer (purple arrows) involving photosystems I and II (PSI and PSII), and Cytochrome b_6f (Cyt b_6f) [8].

2.3.1 Photosystem II

Light reactions in oxygenic photosynthesis start in Photosystem II and the production of oxygen through water oxidation. The process continues further through Photosystem I later. This photosystem is called PSII since, historically, it was found after Photosystem I (PSI). Therefore, the names are irrelevant to the order of actual process and the path of electron transfer.

Photosystem II (PS II) is a large protein complex that is present in cyanobacteria, green algae and plants [2]. PS II core is a dimer and each one of its monomers are considered one functional unit. Each functional unit(monomer) of PSII consists of around 20 protein subunits. The proteins are responsible for binding almost 99 cofactors which are 35 chlorophyll a molecules, 12 carotenoids, 25 integral lipids, 2 hemes, 1 non-heme iron, and a water-oxidizing cluster, Mn_4Ca [2], [9]. The structure of Photosystem II is shown in Figure 2.6 [10]. The core complex of PSII monomer is composed of D1 and D2 protein subunits in the reaction center, and the CP43 and CP47 as the antenna proteins [2]. CP stands for Chlorophyll Protein and the number stands for corresponding protein's molecular mass in kDa. Proteins in the reaction center of

PSII (D1 and D2) are responsible for binding the redox cofactors that make the electron transfer possible in this photosystem, and the antenna proteins (CP43 and CP47) are in charge of binding the antenna chlorophylls. The core complex is then surrounded by CP24, CP26, CP29 and LHCII (Light-Harvesting Complex Proteins) which are called peripheral antenna complexes.

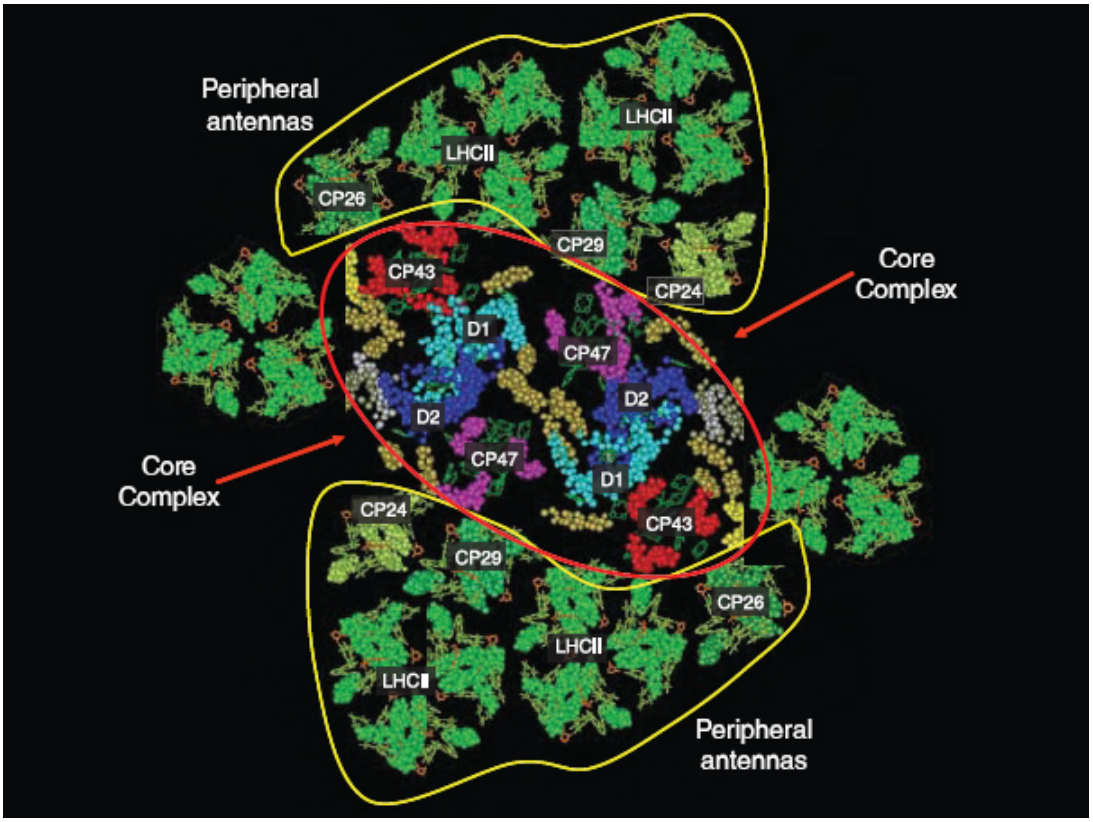

FIGURE 2.6: The top view of PSII (along the line perpendicular to the membrane). This large photosynthetic complex contains pigment-protein complexes such as CP43, CP47, CP24, CP26, CP29, LHCII [10]

The primary electron donor in the reaction center of PSII is called P680, which has the maximum absorption of light energy at 680 nm. P680 is excited to a higher energy level by means of absorption of a photon with suitable energy or excitation energy transfer from neighbour chlorophylls (see section 2.4) and it is converted to $P680^*$. The primary electron acceptor in PSII (pheophytin) captures the electron produced by the excitation of P680 and passes it to Q_A, then Q_B and then eventually to PSI through the electron transfer chain. On the other hand, $P680^+$

(the oxidized P680) behaves like a very strong oxidizing agent and splits water by oxidizing it with the help of Mn_4Ca (oxygen evolving complex). As a result, oxygen molecule(O_2) and H^+ are released and $P680^+$ is reduced to P680 by means of the electrons produced in the water splitting process. This cycle starts over by the absorption of a new photon by P680. (Figure 2.1)

2.3.2 Photosystem I

Photosystem I (PSI) is the second photosystem that is involved in oxygenic photosynthesis process. PSI is responsible of transferring electrons from plastocyanin to ferredoxin (Figure 2.1), and help the conversion of light energy to chemical energy. The same as PSII, PSI is present in cyanobacteria, green algae and plants [2]. PSI is also a large protein complex and it is even larger than PSII. 12 protein subunits exist in each monomer of PSI trimer in cyanobacteria. These proteins are in charge of binding 127 cofactors which are 96 chlorophylls, 22 carotenoids, 4 lipids, 3 clusters of 4Fe4S, 2 phylloquinones, and 1 Ca^{2+} ion [2].

The structure of the the reaction centers of PSI and PSII are similar to each other. The main difference is in the absorption wavelength of the primary electron donors in the two photosystems. The primary electron donor in PSI is P700 which has the maximum light absorption at 700 nm. As a result of light absorption, P700 gets excited to $P700^*$ and the produced electrons are captured by the electron acceptors, iron-sulfur clusters (4Fe4S). The electrons are then passed to ferredoxin. Finally, ferredoxin transfers the electrons to $NADP^+$ to reduce it to NADPH [11]. In addition, $P700^+$ is reduced to P700 by the electrons that are transferred from PSII to plastocyanin through the electron transfer chain and Cytochrome b_6f Complex.

2.3.3 Cytochrome b_6f

Cytochrome b_6f Complex [12], [13], [14], [15] is present in the thylakoid membrane of cyanobacteria, green algae and plants. This protein complex participates in the electron transfer from PSII to PSI through the electron transfer chain [16] (from plastoquinol to plastocyanin, Figure 2.1). It also transfers protons across the thylakoid membrane from stroma to lumen. Cytochrome b_6f exists in vivo in dimeric form and it has only one Chlorophyll *a* molecule per each protein monomer. The exact function of Chl *a* in Cytochrome b_6f is not completely understood, yet [13], [14], [15], as it is not believed to be a part of the electron transport chain.The structure of Cytochrome b_6f is shown in Figure 2.7.

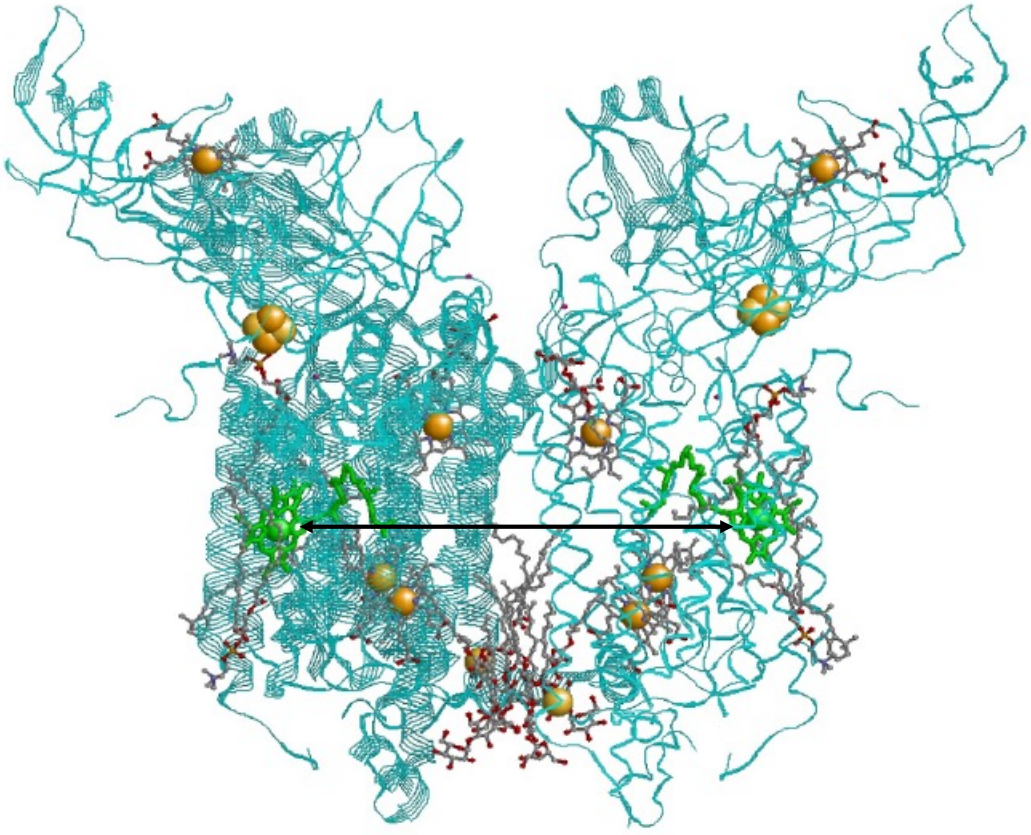

FIGURE 2.7: Structure of the Cytochrome b_6f dimer. PDB ID: 2E74 [12]. Chlorophyll *a* molecules are highlighted in green. Iron atoms of hemes and iron-sulfur clusters are highlighted in gold. The Mg-to-Mg distance is shown with black arrow, and is $\backsim$ 6.1 nm .

The other cofactors of Cyt b_6f absorb light in different wavelengths compared to Chl *a* and most of these cofactors participate in the charge transfer process from PSII to PSI. The distance between the centers of the two Chl a molecules (the Mg-to-Mg distance) of the dimer is 6.1 nm, which means the chlorophylls are relatively far from each other and the interaction between them should be very weak.

In this study, we investigate the energy landscape of Cytochrome b_6f complex isolated from spinach.

2.4 Excitation Energy Transfer

The photosynthetic process starts when a pigment (Chlorophyll) absorbs the correct amount of energy and goes to an excited state. The transition to the excited state is initiated either by the light energy with the suitable wavelength or by the excitation energy transfer between pigments. The latter takes place when there is a strong overlap between the fluorescence and the absorption bands of the two pigments, called donor and acceptor, respectively [17]. These pigments may be chemically same or different (e.g. Chl *b* and Chl *a*). Excitation energy transfer also depends on the distance and orientations of the neighbouring pigments [18]. The simple model of energy transfer, applicable for weak to moderate interaction between the pigments, is known as Förster Resonance Energy Transfer (FRET) or Förster's theory [18]. According to the Förster's theory, Equation 2.1, the excitation energy transfer probability is inversely proportional to R^6 due to the dipole-dipole coupling mechanism [19], where R is the distance of the donor and the acceptor pigments [20].

$$E = \frac{R_0^6}{R_0^6 + R^6} \tag{2.1}$$

R_0 is the Förster Radius / Distance, which is the distance where the energy transfer efficiency reaches the 50% of its maximum amount. R_0 is given by:

$$R_0^6 = \frac{9000(ln10)k^2 Q_D J}{128\pi^5 n^4 N_{AV}} \tag{2.2}$$

where k is the orientation factor, Q_D is fluorescence quantum yield of the donor in the absence of acceptor, J is overlap between donor emission and acceptor absorption, n is the refraction index and N_{AV} is the Avogadro's number [21]. Figure 2.8 shows the simplified mechanism of excitation energy transfer and highlights the spectral overlap.

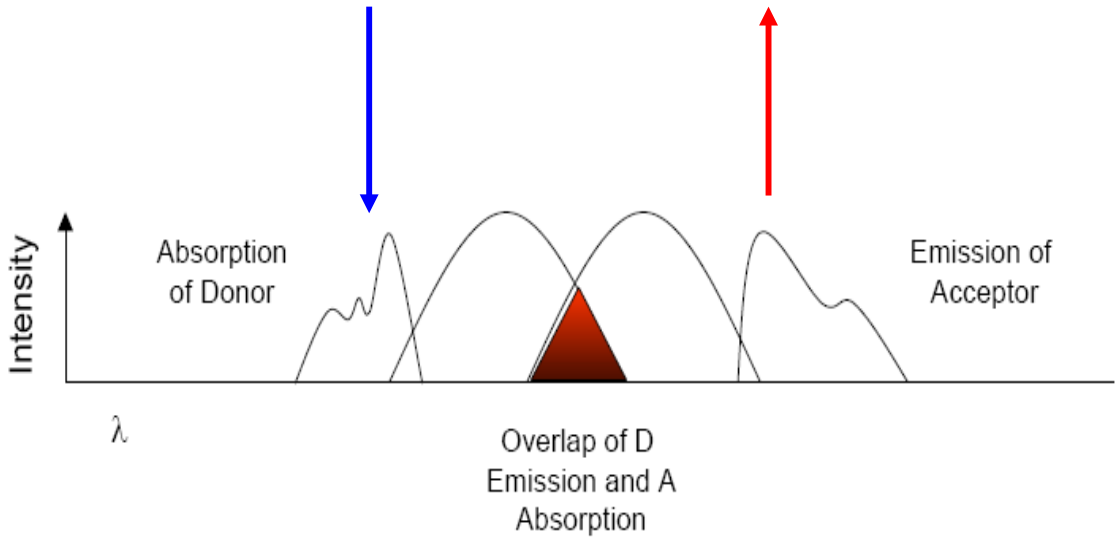

FIGURE 2.8: Simplified Mechanism of Excitation Energy Transfer (EET). The blue arrow shows the light absorption of donor pigment. The red arrow shows the fluorescence emission of the acceptor pigment after EET. The red area under the curves shows the overlap of the emission spectrum of the donor pigment with the absorption spectrum of the acceptor pigment.

The dependance of EET rate on R^{-6} makes it very sensitive to the smallest changes in R. In Chapter 5 of this work, it is shown that EET is very slow in Cytochrome b_6f where the inter-pigment distance is as large as $\backsim 6.1nm$. (See Section 5.3.2 in Chapter 5)

2.5 Photosynthesis and Renewable Source of Energy

Humankind will eventually run out of the available non-renewable sources of energy, such as fossil fuels. Therefore, it is essential to substitute the nonrenewable sources of energy with the renewable ones as soon as possible to maintain life and modern civilization in the future. Light energy of the Sun is considered one of the most abundant sources of energy that is available to humankind. Nature has been taking advantage of solar energy through the photosynthesis process. The primary light-induced steps of the photosynthesis process can operate with up to 100% energy conversion efficiency under the optimum conditions [22], [23]. Modern technology is trying to use the photosynthesis mechanism in making practical artificial photosynthesis systems that are capable of converting solar energy to other types of energy. Despite all the developments, the current technology is still far from using the solar energy to the full extent [22], [23]. A comparison between the energy conversion efficiencies in natural photosynthesis (in the reaction center of PSII) and in artificial photosynthesis (in Dye-sensitized solar cells (DSSCs)) is shown in Table 2.1 [23].

Reaction Center	λ_{max} **at RC**[a]	**Fraction of Absorbed Photons**[b]	**Energy Efficiency**[c]
PSII	680nm	0.92	84% (46% [d])
Dye-Sensitized Solar Cells	550nm	0.90	24% (11.18% [e])

TABLE 2.1: Quantum and Energy Efficiencies for Absorbed Photons with Respect to Charge Separation in Photosystem II and Dye-Sensitized Solar Cells for Photons at the λ_{max} of Each Reaction Center (RC) [23]. *"a"* shows the absorbtion maximum of pigments in reaction center performing initial charge separation; *"b"* shows the fraction of absorbed photons that result in stable charge separation; *"c"* shows the ratio of the first *stable* charge separated state energy over the energy of a photon of energy with λ_{max}; *"d"* shows (the number in parentheses) the efficiency based upon energy stored by charge separation between water and Q_B using photons at λ_{max} and includes the effect of quantum efficiency; and *"e"* shows (the number in parentheses) the overall solar energy conversion efficiency [23].

Photosynthetic protein complexes are involved in the whole photosynthesis process from capturing the light energy to converting it to the chemical energy. Thus, it is vital to understand the

role of these proteins fully to be able to improve the artificial photosynthesis systems. Furthermore, the exact transition energies of chlorophylls in those complexes depend on the structure (and dynamics) of the respective protein pockets. Therefore, understanding protein dynamics is essential in order to better understand the photosynthesis process.

Chapter 3

Protein Dynamics

Proteins are very important biomolecules that are made of long chains of amino acids (polypeptides). These biomolecules perform vital roles in living organisms, such as DNA replication, carrying small molecules and catalyzing chemical reactions in the human body, and also transporting charge and energy during photosynthetic process [24]. The primary structure of a particular protein is determined by the linear sequence of amino acids that make up a polypeptide chain. However, a protein needs to fold to its tertiary structure in order to function properly. Tertiary structure is a well-defined three-dimensional structure of a protein in its native state [1]. Human Creutzfeldt-Jakob Disease (CJD), a nervous system degenerative disorder, is a good example of the effects of malfunctioning misfolded proteins [25]. The static tertiary structure of a protein can be determined by means of different methods such as X-ray diffraction or Nuclear Magnetic Resonance (NMR) Spectroscopy; however, knowing the tertiary structure of a protein is not enough to understand the way it functions [1]. It is true that the biochemical function of a particular protein is related to its tertiary structure, but the fact that proteins are not rigid bodies has to be taken into account in studying these complex biomolecules. A particular protein with a given primary structure can exist in various conformational states [26]. Hemoglobin and Myoglobin are good examples involving relatively large conformational changes [26], [27].

These proteins must go through structural fluctuations in order to make it possible for oxygen to bind to the heme iron in their structure reversibly [26]. Therefore, Myoglobin must be a dynamic system to be able to fluctuate between an oxygen-poor state (Mb) and an oxygen-rich state (MbO_2) and, as a result, to function properly [27].

In other words, protein function requires a certain degree of flexibility in its tertiary structure that makes the protein a dynamic system. In fact, *dynamics* is switching between multiple available conformational substates, and the existence of those multiple substates is manifestation of *disorder*. In order to function, a protein needs to have a delicate balance between these states [1]. Therefore, it is necessary to study the dynamics of proteins as well as their tertiary structures to be able to successfully understand the functioning of the proteins. The protein dynamics and the balance between structural order and disorder are reflected in the *Energy Landscape* of a protein [1].

3.1 Protein Energy Landscape

A particular protein can have various overall structures that differ slightly from each other, and are called conformational substates [26]. The existence of the various conformational substates is due to the fact that proteins are complex biomolecules and even the smallest protein consists of a large of number of atoms. In different substates of a protein, the hydrogen bonds and the side chains of the amino acids might have different positions [26]. As it was mentioned before, transition between different states is often required for a protein to function properly. Conformational substates can be shown as the energy minima on the *Energy Landscape* of a protein. The energy landscape of a protein also includes the separating barriers between the individual substates. In other words, the energy landscape refers to the potential energy surface of a protein versus relative coordinates of its atoms [1]. The energy landscape determines the

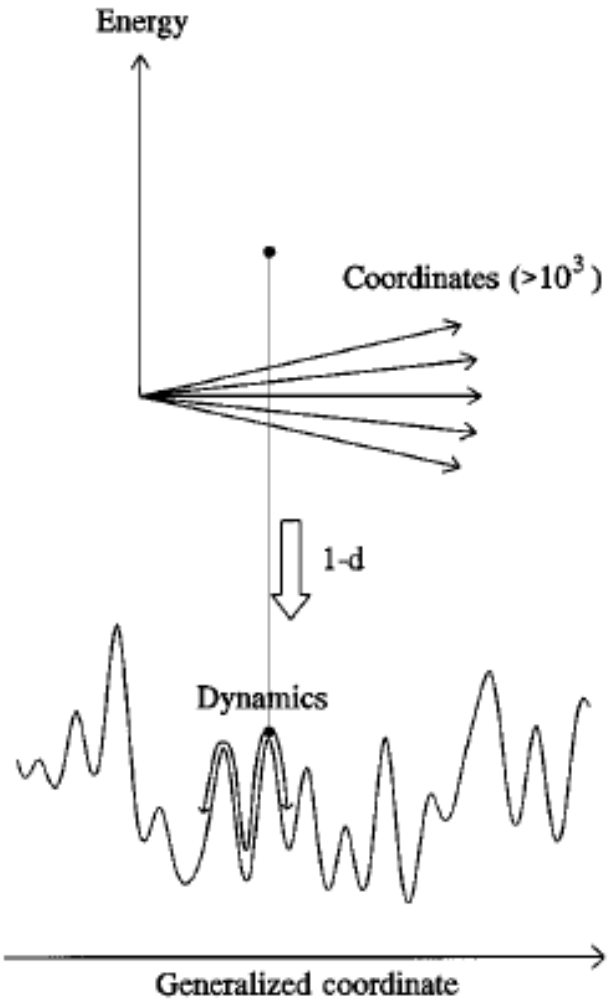

FIGURE 3.1: The Overall Concept of Energy Landscape [1]

structural dynamics of a protein including the folding and unfolding processes as well as local atomic fluctuations. Figure 3.1 shows the overall concept of the energy landscape [1].

The exact energy landscape of a protein is extremely complex since a protein has a large number of atoms (and as a result, a large number of coordinates) that interact in complex cooperative fashion. The aperiodic nature of the protein structure (the same as amorphous materials such as glasses) also adds to this complexity [1]. Thus, the protein energy landscape is multidimensional and a protein can fluctuate between the substates in various ways.

Despite all this complexity, it is well known that the overall structure of the energy landscape

must resemble a funnel (the so-called *folding funnel*), the bottom of which reflects the well-defined native state of a protein [1]. The native structure corresponds to the structure of a folded protein which has an energy lower than the unfolded one or of some intermediate states where the folding is incomplete and the system has not yet reached the native structure. The steep well (folding funnel) on the energy landscape of a protein has a rugged structure itself, which consists of a numerous almost degenerate energy minima (conformational substates) [1]. It is believed that the energy landscapes of proteins have hierarchical organizations with different tiers [26]. In each tier, the conformational substates are separated by energy barriers in the way that the lower tiers are characterized by a lower average energy barriers between the conformational substates. The average energy barrier height, as well as the distance between neighbouring wells (energy minima), increases in the higher tiers [1]. A schematic of the hierarchical organization of the energy landscape of a protein with different tiers is shown in Figure 3.2. Hierarchy Level -2 in Figure 3.2 shows the lower tier in the energy landscape which is a part of a higher tier shown in Level -1 of the same figure. Level -1 itself is a part of a higher tier, hierarchy level 0.

The hierarchical organization of the protein energy landscape makes the structural dynamics of the protein to be hierarchically organized. In other words, a protein can go through small fluctuations on short time scales as well as larger fluctuations on longer time scales. However, the larger fluctuations can be frozen out by lowering the temperature to focus on the dynamics of smaller fluctuations that occur in the lower hierarchical tiers of the protein energy landscape [1].

In this work, the dynamics and the barrier distributions in the energy landscape of Cytochrome b_6f Complex at low temperature is studied by means of optical techniques.

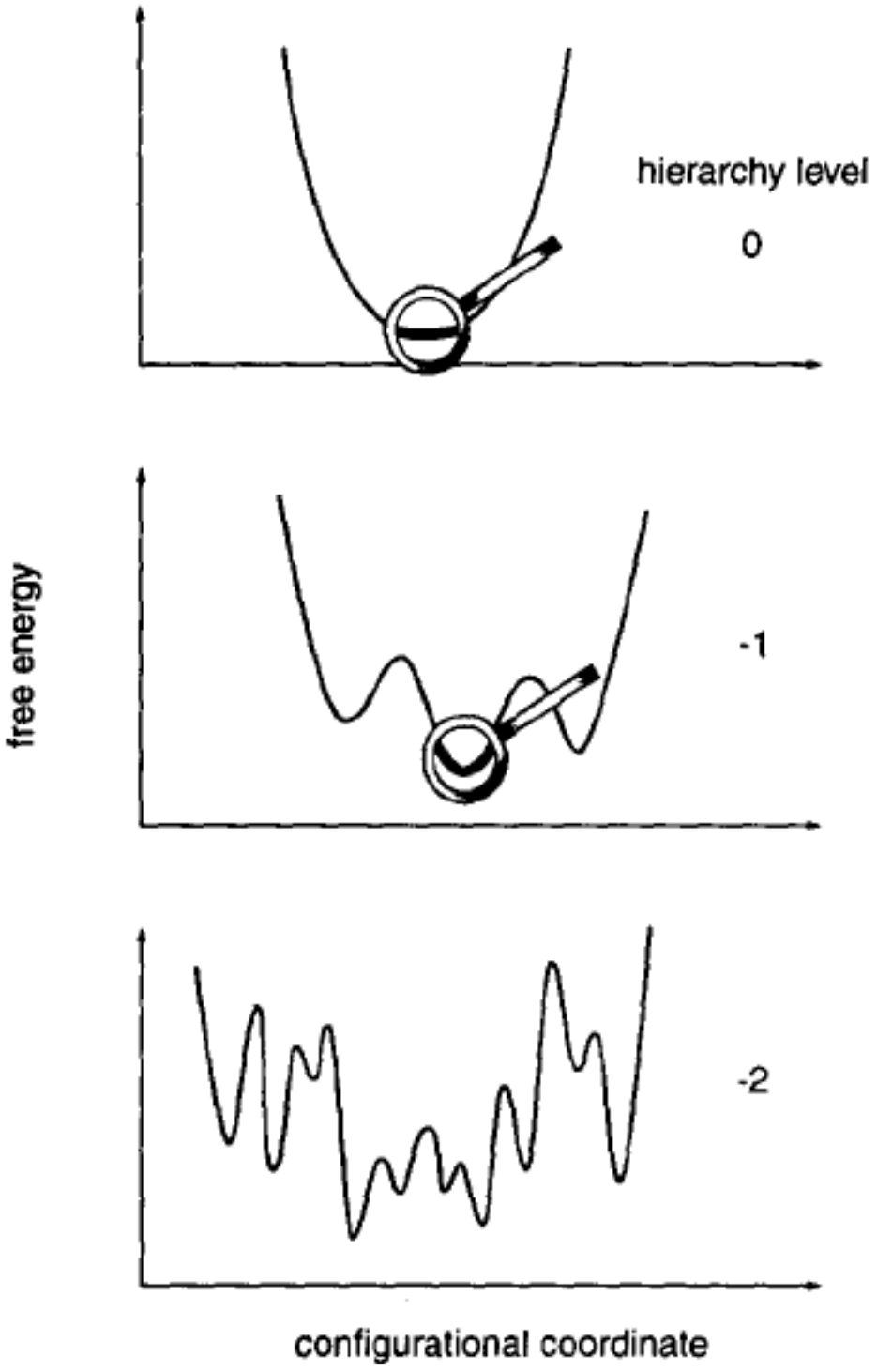

FIGURE 3.2: The Hierarchical Organization of the Energy Landscape with Different Tiers. Lower tiers are shown with negative numbers. [28]

3.2 Two Level System

As it was discussed in the previous section, the energy landscape of a protein is complex since it is multidimensional and fluctuations between the substates might occur through various paths. However, in many cases, relatively large and complex conformational changes can still be described using the simplest possible representation of the energy landscape, the so-called Two Level System (TLS) model.

TLS model describes the energy landscape of a protein in the simplest format where the protein has only two conformational substates with one generalized coordinate. One can mention the well-known Myoglobin and the ligand binding to heme iron as an example [26]. According to [26], it can be assumed that binding process takes place inside the heme pocket of Myoglobin and Myoglobin fluctuates between two different states during the process of breaking the iron-ligand bond with the light pulse and rebinding the ligand to the heme iron (Fe) again. The potential energy landscape of the Myoglobin is depicted with respect to one generalized coordinate in Figure 3.3. In Figure 3.3(a), It is assumed that ligand is bound to the heme iron initially (state A) and the light pulse breaks this bond and moves the ligand to a different position within the heme pocket (state B). The corresponding energy levels of the protein are shown in Figure3.3(b), where H_{BA} shows the barrier height and k_{BA} shows the transition rate from state B (unbound ligand) to state A (ligand bounded to Fe).

The double-well potential or the TLS model has been used in amorphous solids and glasses to describe their dynamic properties [29], and can also be used for proteins [30]. In this case, an ensemble of systems with only two conformational states (two wells) that are separated by a potential energy barrier can be used instead of the complex energy landscape, shown in Figure 3.1. The parameters of the TLS such as barrier heights, distance between two wells and asymmetries are shown in Figure 3.4.

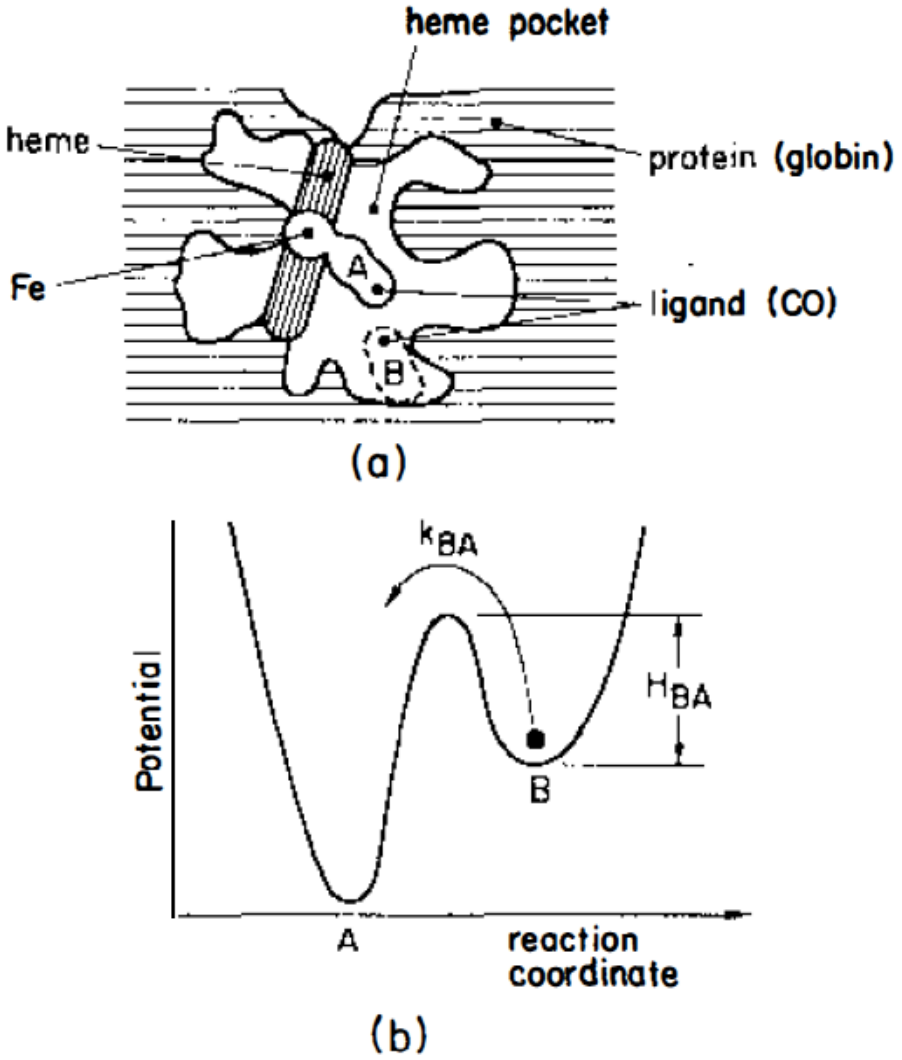

FIGURE 3.3: Two Level System for Myoglobin. (a) Two states of protein in the real space shown as A and B. (b) The corresponding potential energy in state A where the ligand is bound to heme iron, and in state B where the bound is broken and the ligand is in the heme pocket of the protein. [26]

In Figure 3.4, V is the height of potential barrier between two energy minima, d is the distance between two wells, Δ is the asymmetry parameter which shows the difference between the zero level of the phonon/vibrational mode in each well, and $\frac{\hbar\Omega}{2}$ is the lowest vibrational energy in each state.

Transition between the two conformational states or the two minima is assumed to be dominated by tunneling through the potential barrier at low temperatures, although the groups of atoms or

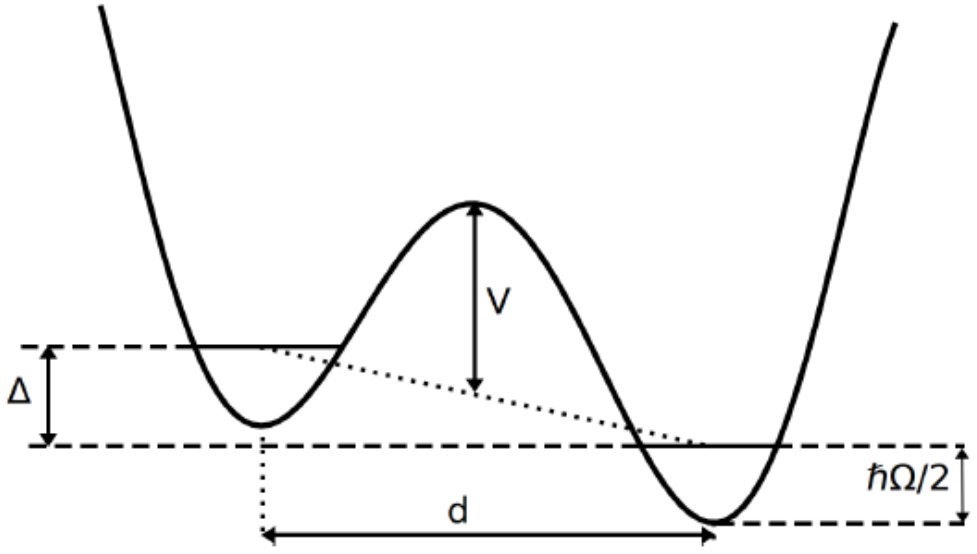

FIGURE 3.4: Two Level System Model [31]

entities involved in this process are not completely known for most systems, yet. The tunneling parameter (λ) can be expressed in terms of the potential energy barrier height (V) between two well by Equation 3.1 [32].

$$\lambda = \frac{d}{\hbar}\sqrt{2mV} \tag{3.1}$$

where m is the effective mass of the tunneling entity that rearranges during the fluctuations between two states, and d is the distance between two energy minima.

It should be noted that both ground and excited electronic states of the pigment molecule embedded in the protein are involved in the study of protein dynamics by means of optical techniques, such as Spectral Hole Burning. Therefore, another version of TLS model that includes both ground and excited states is used in this study (See Figure 4.7), which is explained in details in Chapter 4.

Chapter 4

Theory of Spectral Hole Burning (SHB)

In general, optical techniques, such as spectral hole burning, can be used in studying the dynamics of proteins and amorphous solids because of the fact that the fluctuations in the structure of condensed phases of matter affect the resonance frequencies of optical transitions of optical centers in the solid [1]. This phenomenon is called *Spectral Diffusion*. In other words, the optical resonance frequency of chromophores will change as a result of conformational changes and structural fluctuations of the host they are dissolved in [1].

The Spectral Hole Burning and Δ-Fluorescence Line Narrowing have been used in this study to probe the dynamics and the energy landscape of Cytochrome b_6f Photosynthetic Complex. This chapter includes the theory behind these techniques and the way they can be applied in studying protein dynamics. Section 4.1 describes the influence of different lattice structures on the optical resonance frequencies. The rest of the chapter is dedicated to the details of spectral hole burning technique.

4.1 Spectroscopy of the Impurity Centers in Solids

The spectral hole burning technique theory relies on the disorder and impurities in solid systems [28]. In other words, the imperfections and impurity centers in the structures of solids are reflected in the spectroscopic measurements.

Before looking at the spectroscopic measurements of multiple molecules introduced into the lattice structure of a solid, one can consider a single molecule in the vacuum when there is no interactions between different molecules. In this case, the absorption spectrum of the single molecule would be dominated by a narrow sharp peak at a low temperature. This type of absorption line is called the *natural line* which has a Lorentzian line shape and its width is given by γ_{nat} (the natural line width defined as full width at half maximum(FWHM)) as follows:

$$\gamma_{nat}(cm^{-1}) = \frac{1}{2c\pi\tau_1} \tag{4.1}$$

where τ_1 is the excited state lifetime and c is the speed of light.

Now, if the single molecule is moved into a solid structure, the shape of the absorption spectrum will change. The narrow sharp peak of the natural line in vacuum will be re-framed as *Zero-Phonon Line* (ZPL) and a phonon wing, *Phonon-Side Band* (PSB), will be produced as a result of phonon transitions in the solid. The shape of this absorption spectrum, including ZPL and PSB, follows the *Franck-Condon principle* for lattice vibrations [28] and is shown in Figure 4.1. The Franck-Condon principle states that since the electrons are much lighter than nuclei, the coordinate does not change during transition from one state to another. (This is based on the Born-Oppenheimer approximation, which assumes that the motion of nuclei and electrons can be separated.) Besides, the most likely transitions are those with the best overlap of the vibrational wavefunctions according to the Franck-Condon principle.

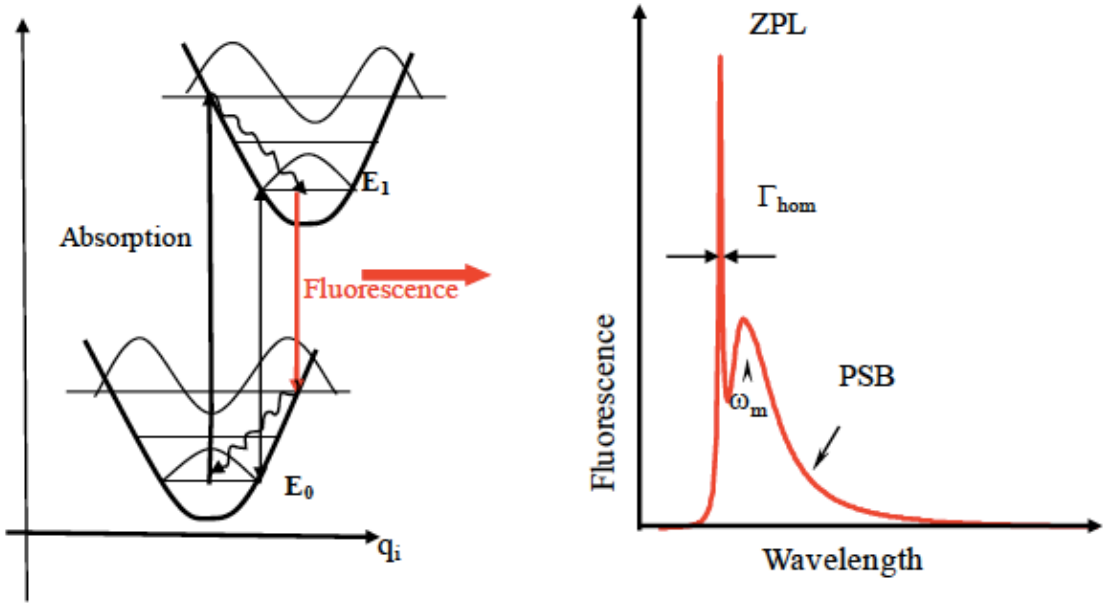

FIGURE 4.1: Franck-Condon principle and the shape of absorption spectrum of a single molecule in solid, including ZPL and PSB.

The relative intensity of the Zero-Phonon Line is defined by the *Debye-Waller* factor given by α in Equation 4.2.

$$\alpha = \frac{I_{ZPL}}{I_{ZPL} + I_{PSB}} \tag{4.2}$$

where I_{ZPL} shows the intensity of zero-phonon line and I_{PSB} shows the intensity of phonon-side band. The Debye-Waller factor depends on another parameter, *the electron-phonon coupling* (S). The electron-phonon coupling (also known as Huang-Rhys factor [33]) corresponds to the average number of phonons that are excited when an electronic excitation occurs. The dependence of Debye-Waller factor (α) on the electron-phonon coupling parameter is given by Equation 4.3.

$$\alpha = exp(-S \times \coth(\frac{\Omega_M}{2k_BT})) \tag{4.3}$$

where Ω_M is the PSB peak frequency (difference in the maximum energies of ZPL and PSB), T is the absolute temperature and k_B is the Boltzmann constant.

It should also be noted that at low temperatures, the relative intensity of ZPL is larger and its width is narrower than those for PSB. When the temperature is increased, the ZPL peak absorption gets smaller and the PSB becomes more dominant in the absorption spectrum [28]. Eventually, the ZPL and PSB will merge in the way that one cannot distinguish them any more. The shapes of ZPL and PSB at different temperatures are shown in Figure 4.2.

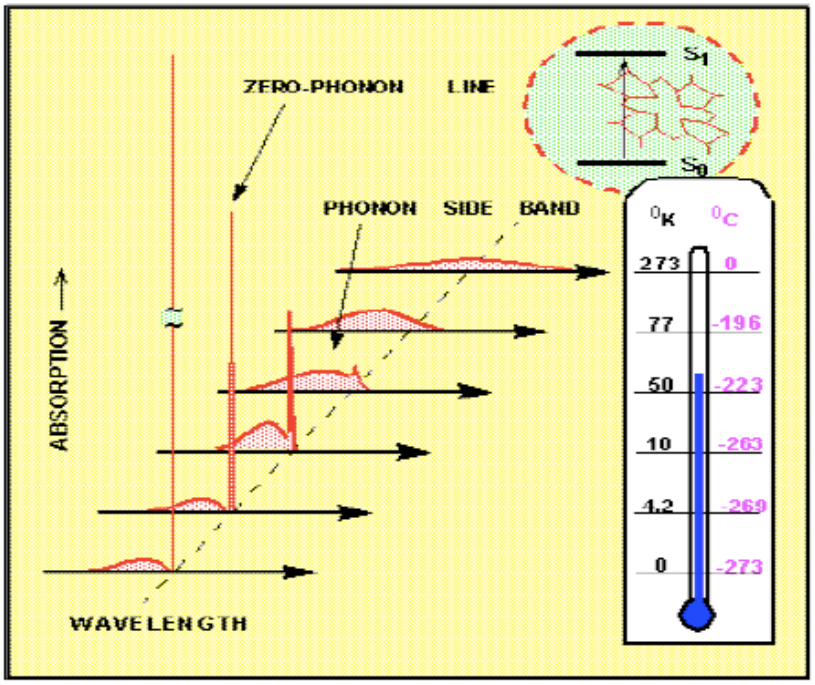

FIGURE 4.2: Dependance of Zero-Phonon Line and Phonon Side Band Intensities on Temperature. [34]

The width of the ZPL shown in Figure 4.1 is called the *Homogenous Linewidth* Γ_{hom}, which is given by Equation 4.4. The homogenous linewidth is the minimum absorption linewidth of a guest molecule in a *host* environment.

$$\Gamma_{hom} = \frac{1}{\pi \tau_2} \tag{4.4}$$

where τ_2 is the total dephasing time [28]. The total dephasing time, or the excited state coherence lifetime, is affected by two physical contributions. These contributions are from the excited state lifetime τ_1, and the pure dephasing time shown as τ_2^*. The excited state lifetime is the time of relaxation of the system from the excited state to the ground state. The pure dephasing time, or the pure phase-destroying time according to [28], comes from the interaction with the lattice vibrations and is the time for which the phase of the excited state wavefunction is preserved. In other words, as well as the excited state lifetime and the relaxation of systems from excited state to ground state, the thermal vibrations of the lattice structure will destroy the excited state coherence [28]. The contributions of these two effects on the total dephasing time and on the homogenous linewidth shown in Equation 4.5.

$$\Gamma_{hom} = \frac{1}{\pi\tau_2} = \frac{1}{2\pi\tau_1} + \frac{1}{\pi\tau_2^*(T)} \tag{4.5}$$

The pure dephasing time, τ_2^*, is infinitely long (i.e. the pure dephasing process is infinitely slow) at the absolute zero. Therefore, the fluorescence lifetime, τ_1, would be the only factor affecting the homogenous linewidth when the pure dephasing process is negligible [28].

Next, one can consider the lattice structure of a perfect crystal which has been doped with several guest molecules (Figure 4.3). In the perfect crystal, all guest molecules are in the same local environment and as a result, will absorb light at the exact same frequency. In other words, the absorption spectra of all the guest molecules that has been dissolved in a perfect crystal structure with a very low concentration (low concentration is to make sure that there is no interactions between guest molecules) would be exactly the same; however, the absorption linewidth would be broader than the one in the vacuum.

So far, the effects of a perfectly ordered structure on the absorption spectrum of the embedded guest molecules has been discussed. However, the structure of proteins is not similar to a perfect

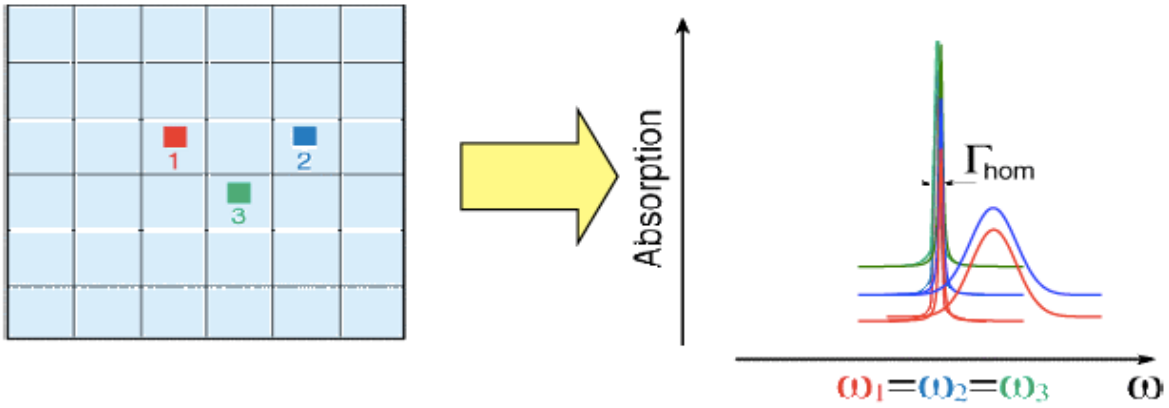

FIGURE 4.3: Right: The lattice structure of a perfect crystal with doped guest molecules. Left: The absorption lines guest molecules in the perfect crystal, where Γ_{hom} is the homogenous linewidth.

crystal, and is in some respect amorphous, resembling that of glasses. Figure 4.4 [28] shows the structure of an amorphous host with the impurity centers embedded into its structure.

In the case of amorphous host structure, each guest molecule would be interacting with a different environment and as a result, the absorption spectrum of the sample would be *inhomogeneously* broadened. In order to get around the inhomogeneous broadening in proteins and glasses, the spectral hole burning technique can be used [28]. This technique is explained in Section 4.2 in details.

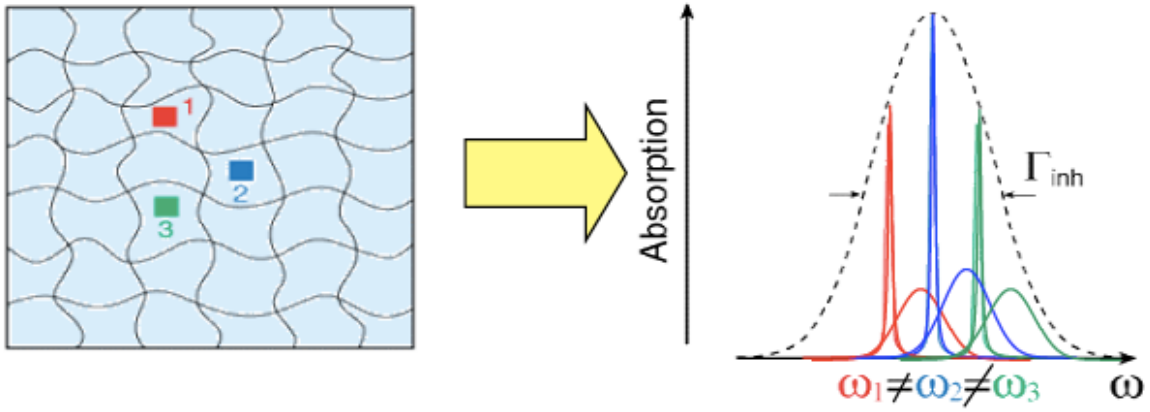

FIGURE 4.4: Right: The lattice structure of an amorphous solid doped with guest molecules. Left: The absorption spectrum of the shown lattice which is inhomogeneously broadened.

It should be noted that the absorption spectrum, in the case of amorphous host, is the result of convolution of the so-called *Site Distribution Function* (SDF), which is the distribution of probabilities of ZPL transitions of guest molecules, with the *Single Site Absorption* (SSA), which is the absorption of a single guest molecule including ZPL and PSB [35]. This concept is shown in Figure 4.5.

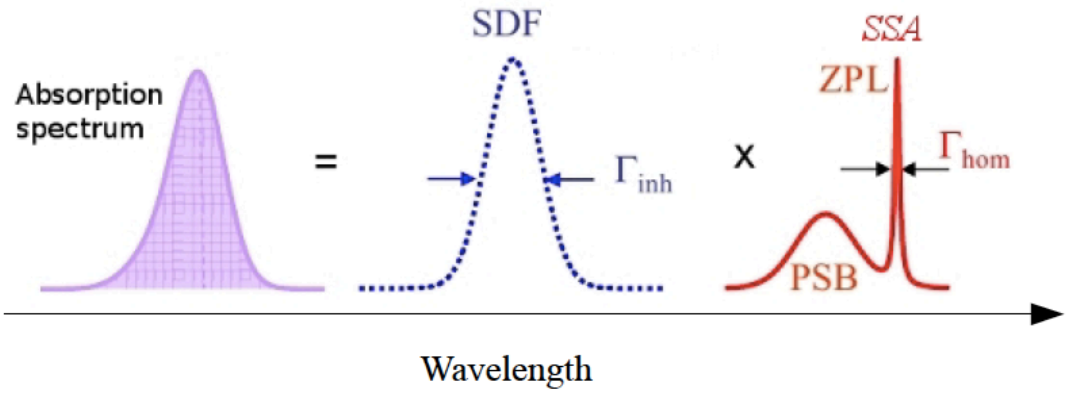

FIGURE 4.5: The absorption spectrum as a result of convolution of Single Site Absorption and Site Distribution Function. [36]

4.2 Spectral Hole Burning

As it was mentioned before, proteins are structurally disordered and as a result their absorption spectra are inhomogeneously broadened. One has to get around the inhomogeneous broadening in order to study the spectral diffusion and dynamics of proteins. Optical line narrowing techniques, such as Spectral Hole Burning (SHB), are suitable for this purpose [1].

Narrow band lasers are used in spectral hole burning in order to eliminate the problem with the broadened absorption spectra of pigment-protein complexes and other amorphous solids. These lasers are capable of exciting only a fraction of molecules of the sample which have ZPL in resonance with the laser frequency. As a result, the resonant molecules will stop absorbing photons at the burning frequency (laser frequency) and a hole will occur in the absorption

spectrum of the sample. A simple schematic of spectral hole burning and the resulting absorption spectrum is shown in Figure 4.6.

Hole burning might affect the sample in two different ways:

1. **Photochemical Hole Burning**:

   As a result of hole burning, the resonant molecules might go through chemical changes and no longer absorb light at the laser frequency since their molecular structure is different than the non-burnt molecules which are in resonance with the laser frequency. In this case, the chemical changes are mostly irreversible and this type of hole burning is called Photochemical Hole Burning (PHB).

2. **Non-Photochemical Hole Burning**:

   In this case, there is no chemical changes in the burnt molecules. Instead, conformational changes happen in the environment of chromophores as a result of excitation by laser. This kind of hole burning is called Non-Photochemical Hole Burning (NPHB). In case of NPHB, the physical and structural changes in the host environment are considered the reason for the hole production since the resonant frequencies of the burnt molecules changes with the structural fluctuations of their environment. Therefore, the burnt molecules absorption frequencies would be different than the laser frequency. NPHB is used in this study and its mechanism is explained later in this section in details.

One can find the **Hole Burning Spectrum** (HBS) by using Equation 4.6:

$$HBS = A(\Omega, t) - A(\Omega, 0) \tag{4.6}$$

where $A(\Omega,\ 0)$ is the pre-burn spectrum and $A(\Omega,\ t)$ is the post-burn spectrum measured after the burning time t.

It should be noted that SHB is an ensemble technique. In addition, hole burning is a probabilistic process and different molecules in resonance with the laser burn at different times. Thus, as we illuminate the sample with the laser, the hole grows gradually. This introduces **Fractional Hole Depth** (FHD), an important parameter in the spectral hole burning experiments, which is given by Equation 4.7.

$$FHD = 1 - \frac{A(\Omega, t)}{A(\Omega, 0)} \tag{4.7}$$

In the spectral hole burning experiment for small fractional hole depths, one can relate the burnt hole width to the homogenous width of ZPL through Equation 4.8 [28]. According to this equation, the hole width (Γ_H) is twice the homogenous line width (Γ_{hom}). This phenomenon occurs because the post-burn absorption spectrum, that contains the experimental hole, is a convolution of single molecule absorption (SSA) containing ZPL with the post-burn SDF that also contains a ZPL-shaped hole. It should also be noted that the burnt hole has a Lorentzian shape since the shape of the ZPL is also Lorentzian.

$$\Gamma_H = 2\Gamma_{hom} \tag{4.8}$$

Using Equation 4.5:

$$\Gamma_H = 2\Gamma_{hom} = \frac{2}{\pi\tau_2} = 2(\frac{1}{2\pi\tau_1} + \frac{1}{\pi\tau_2^*(T)}) \tag{4.9}$$

As it was mentioned earlier, the fluorescence lifetime, τ_1, would be the only factor affecting the homogenous linewidth at the absolute zero where the pure dephasing time, τ_2^*, is infinitely long [28]. Therefore, at the absolute zero, one can measure the fluorescence lifetime by measuring the hole width (Γ_H). However, at temperatures other than zero obtaining τ_1 from the hole width

is not possible. Therefore, the fluorescence lifetime has to be measured independently by means of other techniques in order to be able to measure the pure dephasing time by means of Equation 4.9, and to study those conformational changes in the structure of the surrounding environment that affect the pure dephasing time.

Now, going back to the theory of hole burning, one needs a detailed understanding of all the factors affecting the post-burn absorption spectrum $A(\Omega,\ t)$ of the ensemble in order to study the conformational changes by means of SHB technique. As it was mentioned in Section 4.1, the absorption spectrum is the convolution of site distribution function (SDF) with the single site absorption (SSA) (the absorption of a single molecule). The hole burning process modifies SDF and produces a hole in the absorption spectrum. Figure 4.6 shows the absorption spectrum before and after hole burning on the same graph. Hole is obvious in the post-burn spectrum. The figure also includes the Pseudo and Real PSBH and anti-hole[1], as well as the laser wavelength, λ_B, used for the hole burning. One can consider hole as an image of zero-phonon line (ZPL) of the molecule which is in resonance with laser burn frequency. The resonant molecule has a phonon side band (PSB) in addition to ZPL. Therefore, when hole is burnt by the laser, both ZPL and PSB of the resonant molecules vanish from the pre-burn absorption spectrum, and can be seen in the post-burn absorption spectrum as a *Zero-Phonon Hole* (ZPH) and the real *Phonon Side Band Hole* (PSBH). In addition to ZPH and "real" PSBH, another feature, "pseudo" PSBH, occurs in the post-burn spectrum as a result of excitation of some molecules which have ZPL that are not in resonance with the laser; however, their PSB are at the burning wavelength. Thus, these molecules are excited through their PSB and produce "pseudo PSBH" in the post-burn absorption spectrum.

[1] "Anti-Hole" is used in Fig. 4.6 instead of "Photoproduct" since "Photoproduct" is mostly used in PHB when chemical changes happen in the burnt molecules. Anti-hole is a better choice of terminology in case of NPHB.

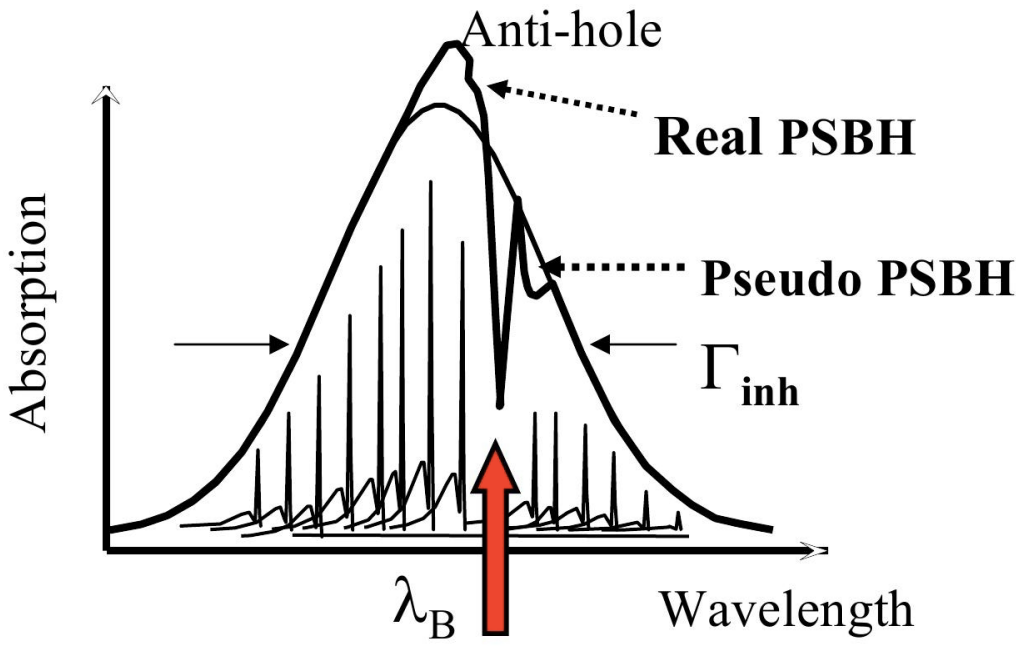

FIGURE 4.6: Post-Burn and Pre-Burn Absorption Spectra in Non-Photochemical Hole Burning (NPHB). ZPH, real and pseudo PSBH are also shown on the post-burn spectrum as well as the produced anti-hole. [36]

The post-burn spectrum *A(Ω, t)* is defined by the SHB Master Equation [35] (Equation 4.10) for a hole burnt at ω_B for time *t*.

$$A(\Omega,t) = 1.5 \int d\omega L(\Omega-\omega)G(\omega) \int d\lambda f(\lambda) \int d\alpha \sin(\alpha)\cos^2(\alpha) e^{-Pt\sigma\phi(\lambda)L(\omega_B-\omega)\cos^2(\alpha)} \quad (4.10)$$

where *G(ω)* is the site distribution function (SDF), describing the probability of finding single site absorptions (SSA) with ZPL at ω. *G(ω)* usually is Gaussian prior to burning. *L(Ω - ω)* is the single site absorption (SSA) with an area normalized to unity on ω scale. P is the total photon flux. Also, it is assumed that the laser linewidth used for hole burning is narrower than the homogenous width (or ZPL width) [35]. α is the angle between the polarization of the laser and the transition dipole vector of the chromophore with the integral absorption cross-section of σ. λ is the tunneling parameter which has the distribution *f(λ)*. *f(λ)* is usually considered Gaussian with the mean value of λ_0 and the standard deviation of σ_λ [35]. Finally, $\phi(\lambda)$ is the quantum yield of non-photochemical hole burning which is given by Equation 4.11 [35].

$$\phi(\lambda) = \frac{\Omega_0 exp(-2\lambda)}{\Omega_0 exp(-2\lambda) + \tau_1^{-1}} \tag{4.11}$$

Ω_0 in Eq. 4.11 is the attempt frequency, which defines how often the systems try to pass the potential energy barrier between two wells in TLS model by tunneling (See Section 3.2 for more details on TLS). It is believed that the attempt frequency, Ω_0 is on the order of 10^{12} Hz [37].

As it was mentioned, None-Photochemical Hole Burning (NPHB) is the mechanism used in this study, which can be explained by a TLS model that includes both ground and excited states of the chromophore. This type of a model with only one generalized coordinate is shown in Figure 4.7 with two minima in both ground and excited states, and lower hierarchy minima in each well. NPHB occurs in the higher tier shown in this figure. ΔE_1 is the laser photon energy which is in resonance with the transition frequency of chromophore molecules. In this case, the system will go to the excited state 1 as a result of photon energy absorption and may make a transition to the excited state 2 during the lifetime of excited state, assuming the potential barrier height in excited state is smaller than the one in the ground state. The system then returns to the ground state from the excited state 2 and gets trapped there. The parameters of the ground state determine the length of time that it takes for the system to go back to the ground state 1. As it can be seen in Figure 4.7, the resonance frequency of the system in the ground state 2 (ΔE_2) is slightly different than what it was before burning. Therefore, the burnt molecule would no longer absorb at the same frequency and the absorption spectrum would be shifted and the anti-hole will be formed. However, the energy difference between hole and anti-hole is relatively small in case of NPHB compared to PHB [38].

In NPHB, system may make the transitions between two wells by tunneling through the potential barrier or by barrier hopping over the potential barrier, as it is shown in Fig. 4.7. However, it is generally believed that at low temperatures the transition between two wells in the excited

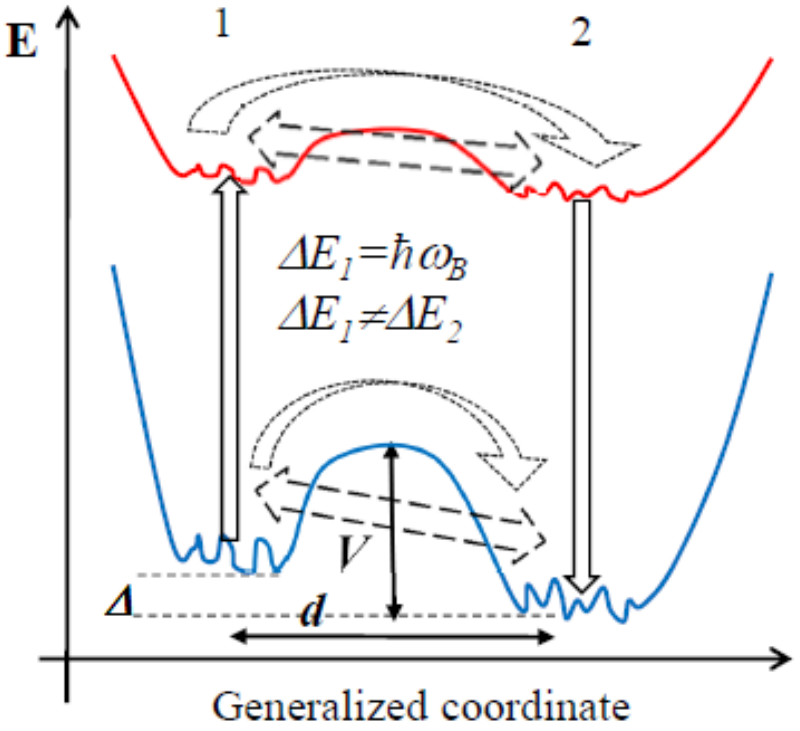

FIGURE 4.7: TLS model for NPHB with ground and excites states, where V is the height of potential energy barrier, d is the distance between two wells, Δ is the asymmetry parameter, ω_B is the burn frequency, and ΔE_1 and ΔE_2 are the resonant frequencies of system in state 1 and state 2, respectively. [37]

state occurs by means of tunneling [39], [40]. It should be noted that tunneling is a phonon-assisted process (i.e. the phonon has to carry the energy equal to the assymetry of the TLS to satisfy the conservation of energy). The phonon might gain or lose energy during the transition. The so-called *downhill tunneling* (transition from 1 to 2 in Figure 4.7 above) occurs when the phonon gains energy during a transition, and *uphill tunneling* occurs when the phonon loses energy during the transition. It should be noted that the rate of uphill tunneling is always lower than the rate of downhill tunneling since the phonon needs to have enough energy in the first place in order to lose energy during the uphill tunneling.

The downhill and uphill tunneling rates are given by Equations 4.12 and 4.13, respectively [41], [42], [43].

$$R_{downhill} = \frac{3f^2W^2E}{16\pi\rho c^5\hbar^5}(n(E,T)+1) \tag{4.12}$$

$$R_{uphill} = \frac{3f^2W^2E}{16\pi\rho c^5\hbar^5}(n(E,T)) \tag{4.13}$$

where f is the deformation potential in the two level system model, ρ is the local mass density of sample, c is the speed of sound in amorphous solid environment, $\hbar$ is the $\frac{h}{2\pi}$ where h is the Planck's constant. W is the tunneling frequency, E is the tunneling splitting and n(E, T) is the occupation number for phonons [38]. It should be noted that n(E, T) and n(E, T) + 1 are necessary (in their given forms) to satisfy the energy balance and conservation of energy during the tunneling process (since this process is phonon-assisted and the change in phonon energy is equal to the asymmetry parameter in TLS.).

W, E and n(E, T) are given by:

$$W = \omega_0 exp(-\lambda) \tag{4.14}$$

$$E = \sqrt{\Delta^2 + W^2} \tag{4.15}$$

$$n(E,T) = (exp(E/k_BT) - 1)^{-1} \tag{4.16}$$

In Eqs. 4.14 and 4.15, λ is the tunneling parameter given by Eq. 3.1 and Δ is the asymmetry parameter. W is usually much smaller than Δ; therefore, E would be approximately equal to the asymmetry: $E \cong \Delta$ [38].

Downhill and uphill tunneling rates can also be written in relationship with the attempt frequency Ω_0, as follows [44] :

$$R_{downhill} = \Omega_0(n(E,T)+1)exp(-2\lambda) \tag{4.17}$$

$$R_{uphill} = \Omega_0 n(E,T)exp(-2\lambda) \tag{4.18}$$

The spectral diffusion occurring in the lower tier shown in each well in Figure 4.7 makes contribution to the hole broadening. Therefore, the hole width measured by NPHB some time after burning follows Equation 4.19 rather than Equation 4.8 given in Section 4.2. Γ_{SD} is the contribution of spectral diffusion on the hole broadening which depends on the waiting time.

$$\Gamma_H = 2\Gamma_{hom} + \Gamma_{SD} \tag{4.19}$$

4.3 Hole Growth Kinetics

Hole Growth Kinetics (HGK) is one of the useful methods in Spectral Hole Burning to study the protein dynamics and parameters of the energy landscape of the protein. As it is also mentioned in the name of this technique, hole growth kinetics studies the way a hole *grows* as a result of illuminating the sample with a constant laser power density for a long amount of time (i.e. hours). In HGK measurements, a decrease in the fluorescence excitation signal (or the absorption signal) is observed while the irradiation dose (product of constant laser power density and time of hole burning) is increasing. After a certain amount of time (depending on sample), the fluorescence excitation signal almost stops decreasing. At this point, a saturated hole with maximum depth is produced in the absorption spectrum of the sample. In other words, one can study the change in fractional hole depth (FHD) upon increasing irradiation dose during the burning process (i.e. at the same time as the actual hole burning is happening) by collecting the fluorescence excitation signal by means of a photomultiplier. It should be noted that the

excited state energy landscape parameters are explored in HGK since the tunneling resulting in hole burning is happening in the excited state.

Once the burning is stopped, the post-burn absorption spectrum is scanned with a significantly lower intensity in order to study the produced hole and its recovery as a function of time (or increased temperature) , and as a result, to study the ground state parameters. Hole recovery is explained in Section 4.4 in details.

As it was mentioned before, HGK is useful in determining various parameters such as the electron-phonon coupling (S) which is related to the depth of saturated hole (ZPH) according to Equation 4.20.

$$ZPHD \approx e^{-S} \tag{4.20}$$

In addition to the electron-phonon coupling, standard deviation (σ_λ) and mean (λ_0) values of the tunneling parameter distribution in the excited state can be found by fitting the experimental HGK curves by SHB master equation (Equation 4.10). To do this, one must fix all the other parameters in Eq. 4.10 with values known during the HGK experiment (e.g. photon flux (P), burning frequency (ω_B), etc) and the values measured by other experiments (e.g. fluorescence lifetime (τ_1)), and find the best fit to the HGK curves by changing the values of σ_λ and λ_0. Therefore, the best fit to the experimental HGK curves leading to a saturated hole gives the correct values of σ_λ and λ_0, and as a result, the whole tunneling parameter distribution in the excited state. One should note that the full λ (or barrier) distribution can be defined with this method. The shape of HGK is determined by the interplay between fluorescence or absorption of the molecules that already burnt and those that did not burn yet. However, the lambda (or barrier) distribution encoded into the hole (and manifesting in recovery) is partial distribution, whose shape may differ from the shape of the full true distribution.

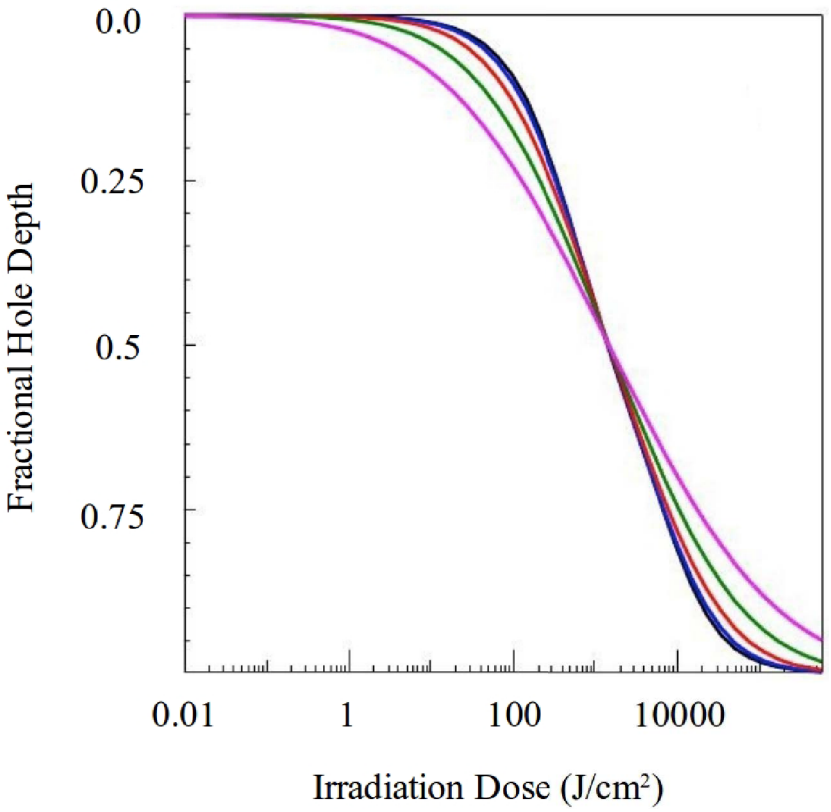

FIGURE 4.8: HGK curves obtained from SHB master equation. In this case, $\lambda_0 = 10$ with various σ_λ (from 0.0 (black) to 0.3, 0,6, 1.0 and 1.5 (magneta)) has been used to plot the curves. [45]

Figure 4.8 shows various theoretical HGK curves obtained by using different values of σ_λ and constant value of λ_0 in SHB master equation [45]. As it can be seen in this figure, σ_λ changes the curvature or slope of the HGK curve. By changing λ_0, and using constant σ_λ, a fixed shape of curve would be shifted left or right to different levels of irradiation dose (not shown).

4.4 Hole Recovery

In order to study the ground state parameters of the energy landscape of protein, one must study the recovery process of the hole. Hole recovery happens because burnt molecules tend to return to their pre-burn states by either tunneling or barrier hopping in the ground state. Hole recovery can be explored by two somewhat different complementary methods:

1. **Hole Recovery at Fixed Temperature**:

   In this case, the temperature remains fixed at the burning temperature and the spectral hole recovers spontaneously. Although the temperature is very low (close to liquid Helium temperature), the hole recovers as a result of tunneling process in the ground state since tunneling occurs even at the lowest temperatures. However, hole recovery at fixed temperature might be very slow and it might take a very long time (i.e. several days) for the spectral hole to recover completely at the fixed burning temperature.

2. **Thermocycling**:

   Thermocycling is the other type of hole recovery experiment. In this case, the temperature of the sample is raised to a certain temperature after the burning is completed (or after a few hours of hole recovery at fixed temperature). Then, the temperature is decreased to the burn temperature again and the hole spectrum is measured. The same process is continued several time with different increasing maximum temperatures. Thermocycling makes the spectral hole recover faster since the burnt molecules will have more energy as a result of heating and they might be able to pass the barriers through barrier hopping in addition to tunneling.

In order to calculate the hole area and analyze the hole recovery data, one should first calculate the number of remaining burnt centers after recovery for the time t and at the temperature T, which is given by Equation 4.22 [46]. This equation can be derived in the following way. First, we assume that the total number of centers in the burned state is given by N_0. In addition, the relaxation rate from burned to unburned state is given by $R(\lambda)$ at a specific temperature T. Thus, according to [46], the number of centers that *relax* from burned to unburned state with the relaxation rates between $R(\lambda)$ and $R(\lambda+d\lambda)$ is equal to $N_0 g(\lambda) d\lambda$ where $g(\lambda)$ is the distribution of tunneling parameter in the ground state. Thus, after the hole recovers for time

t at temperature T, the change in the number of centers in the burnt state associated with crossing the barriers with λ to $\lambda + d\lambda$ is given by:

$$dN(t,T) = N_0 g(\lambda) d\lambda exp(-R(\lambda)t) \tag{4.21}$$

Finally, the total number of centers which have not recovered after time t can be calculated by integrating over all possible relaxation rates, *R(λ)*, which also depends on the temperature T. Therefore,

$$N(t,T) = N_0 \int_0^\infty g(\lambda) d\lambda exp(-R(\lambda,T)t) \tag{4.22}$$

It is believed that up to $\backsim$ 10K, the recovery rate (as well as burning rate) does not show any strong dependency on temperature and the recovery occurs as a result of tunneling (mostly) [46], [38]. Besides, it has been shown that the dominant tunneling process at low temperatures is downhill tunneling (Equation 4.17) [38]. However, the barrier hopping rate has to be taken into consideration for recovery upon thermocycling. The rate with which populations evolve due to barrier hopping is given by Equation 4.23, where Ω_0 is the attempt frequency and V is the potential barrier height which is related to λ through Equation 3.1.

$$R_{hopping} = 2\Omega_0 exp(\frac{-V}{k_B T}) = 2\Omega_0 exp(\frac{-\hbar^2\lambda^2}{2md^2 k_B T}) \tag{4.23}$$

Therefore, the relaxation rate, R, in Equation 4.22 can be written as the sum of downhill tunneling rate and barrier hopping rate:

$$R(\lambda,T) = \Omega_0(n(E,T)+1)exp(-2\lambda) + 2\Omega_0 exp(\frac{-\hbar^2\lambda^2}{2md^2 k_B T}) \tag{4.24}$$

By substituting R(λ, T) in Equation 4.22, we find :

$$N(t,T) = N_0 \int_0^\infty g(\lambda) d\lambda exp(-\Omega_0 t[(n(E,T)+1)exp(-2\lambda) + 2exp(\frac{-\hbar^2\lambda^2}{2md^2k_BT})]) \tag{4.25}$$

which can be written in a simpler form as:

$$N(t,T) = N_0 \int_0^\infty g(\lambda) d\lambda q(\lambda,t,T) \tag{4.26}$$

where:

$$q(\lambda,t,T) = exp(-\Omega_0 t[(n(E,T)+1)exp(-2\lambda) + 2exp(\frac{-\hbar^2\lambda^2}{2md^2k_BT})]) \tag{4.27}$$

q(λ, t, T) shows the fraction of the centers that are not recovered after spending time t, at temperature T [38].

The distribution of tunneling parameter in the ground state can be found by fitting the experimental data to Equation 4.26, with q(λ, t, T) as in Equation 4.27. To do so, one has to first multiply q(λ, t, T) (which is a step-like function) with the post-burn λ-distribution (g(λ)) (which is in fact the partial λ-distribution of the ground state [38]). The λ distribution encoded in the hole remaining after some recovery can be found according to Equation 4.28.

$$g(\lambda)_{next} = g(\lambda)_{previous} \prod_{T,\tau(T)} q(\lambda,t,T) \tag{4.28}$$

As a result, the left side of the area under the post-burn fractional λ-distribution is chopped off, and the remaining area for larger-λ part of the distribution (right side) would be proportional to

the remaining spectral hole area (Figure 4.9). This area will decrease as a result of multiplying g(λ) by q(λ, t, T) for increased time or temperature (i.e. the hole is recovering).

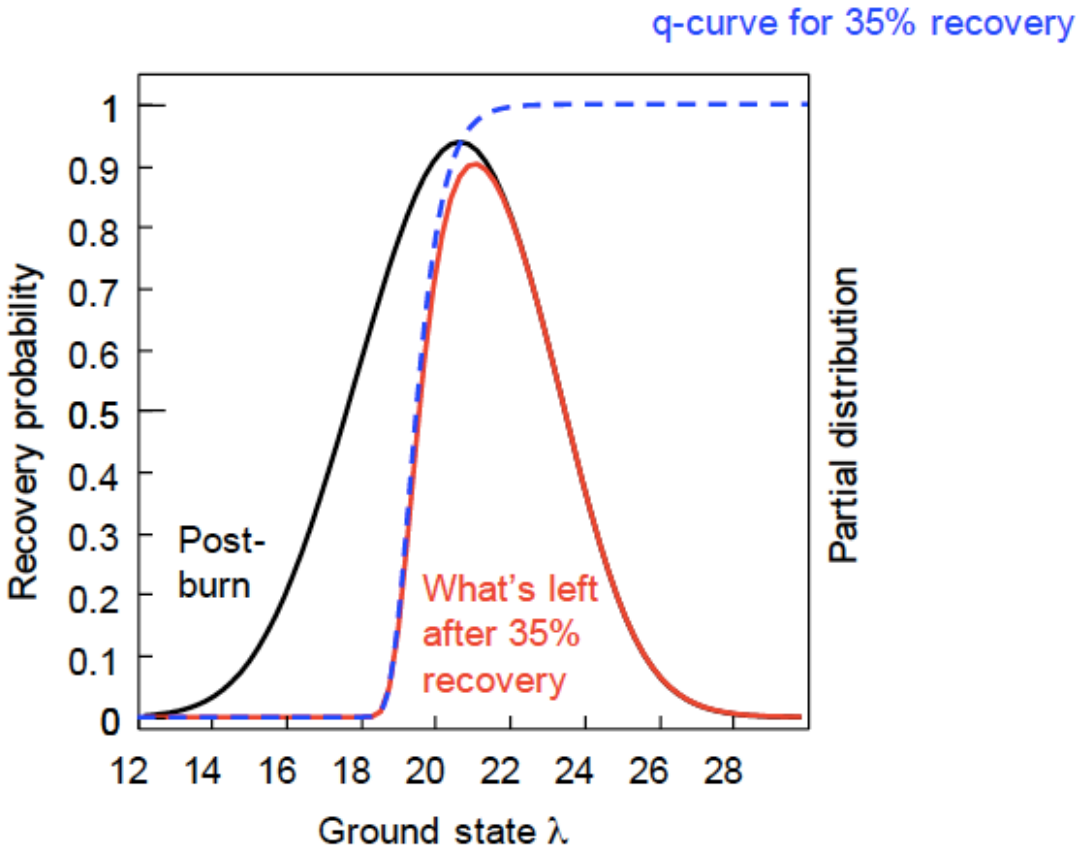

FIGURE 4.9: Post-burn partial λ distribution (black); q-curve resulting in 35% recovery of the hole (blue) and the partial distribution of lambda encoded into the remaining hole (red).

4.5 Fluorescence Line Narrowing

Fluorescence Line Narrowing (FLN) and Δ-FLN are two techniques that provide independent information on the shape of the single-site spectrum (L(Ω) in Equation 4.10), that is an important part of the model used in the study of energy landscapes of proteins (See Equation 4.10, HB master equation.).

Fluorescence Line Narrowing is a line narrowing technique that is used to overcome the problem of inhomogeneously broadened absorption spectrum of a disordered solid. In FLN, a resonant portion of the inhomogeneously broadened absorption spectrum is excited with a narrow band laser at low temperatures [47]. Then, the fluorescence emission, which only belongs to the excited portion of molecules, is collected. The collected emission in FLN is different from the regular fluorescence emission collected with non-selective excitation. In other words, the fluorescence spectrum measured with FLN technique is *narrowed* compared to the regular fluorescence spectrum measured with conventional methods [48]. FLN spectrum contains both real and pseudo PSB. However, unlike in SHB, real and pseudo PSB are both located to the red of the ZPL.

Δ-FLN spectrum is the difference between pre- and post-burn fluorescence line narrowing spectra [49], [50], which is useful in defining electron-phonon coupling parameters [47]. This technique has two significant advantages: (a) the ZPL can be measured directly with Δ-FLN technique since most of the scattered laser light, affecting the ZPL shape in FLN spectra, is eliminated when the difference between the pre- and post-burn FLN spectra is calculated as the Δ-FLN spectrum [47]; (b) the shape of the final Δ-FLN spectrum is equal to the shape of the single site absorption spectrum since the double spectral selection effect of the SHB and FLN eliminates the pseudo-PSB contribution [47].

During most parts of this study, the non-photochemical hole burning (NPHB) technique has been used in order to explore the energy landscape of Cytochrome b_6f complex. In addition, some fluorescence line narrowing (FLN) and Δ-FLN were employed to study the energy transfer processes in the Cyt b_6f sample.

Chapter 5

Probing the Energy Landscape of Cytochrome b_6f Complex by Spectral Hole Burning

This chapter is dedicated to the experimental results and the energy landscape measurements for the Cytochrome b_6f Pigment - Protein Complex. This chapter is mostly based on the following published paper:

M. Najafi, N. Herascu, G. Shafiei, R. Picorel, and V. Zazubovich, "Conformational Changes in Pigment-Protein Complexes at Low Temperatures-Spectral Memory and a Possibility of Cooperative Effects," *The Journal of Physical Chemistry B*, vol. 119, no. 23, pp. 6930 - 6940, 2015.

However, our recent experiments resulted in altering some of the conclusions of the paper (at least quantitatively). The updated version, with additional subsections, reflects our current understanding of Cytochrome b_6f Energy Landscapes and Dynamics.

Some parts of the data included in the above paper were processed by me. In addition, the data from the experiments on Cytochrome b_6f dissolved in deuterated environment and Chlorophyll dissolved in buffer-glycerol matrix (both protonated and deuterated) with no protein were acquired and analyzed by me and Dr. Valter Zazubovits.

5.1 Introduction

Understanding protein energy landscapes in photosynthetic pigment-protein complexes is important both from the general life sciences perspective (information on hierarchal protein energy landscapes [51], [52], [53] is necessary to better understand protein conformational changes and folding) and in photosynthesis research per se (protein dynamics is affecting optical properties, energy and charge transfer processes in proteins involved in photosynthesis). In optical experiments the dynamics of amorphous solids, including proteins, manifests as light- and thermally-induced shifts of spectral lines of the pigments embedded in the solid. These shifts are directly observable in the single molecule / single photosynthetic complex spectroscopy (SPCS) experiments [53], [54]. In the ensemble spectra these shifts manifest as spectral hole burning (SHB) and as hole recovery and broadening [55]. Collectively these phenomena are known as spectral diffusion. SHB involves selecting a sub-ensemble of pigment molecules with zero-phonon lines (ZPL) in resonance with the laser and causing either the photo-chemical transformation of the molecules themselves, or the rearrangement of their environment. In amorphous solids, including proteins at low temperatures, the light-induced rearrangement of the environment is the dominant process. On the ensemble level this mechanism is known as non-photochemical hole burning, NPHB [56] (See Section 4.2 in Chapter 4 for more details) . In the case of SPCS these are just the light-induced shifts of the spectral lines. As the pigment molecule is not modified, the reverse conformational change gives rise to the recovery of a spectral hole or to spectral line returning to its original wavelength. Following NPHB, hole recovery and hole broadening

offer one a window onto the distributions of barriers on the protein energy landscape. The key aspects of the origins of light- and thermally-induced shifts of the spectral lines, the basis of the observations in both SPCS and NPHB experiments, are demonstrated in Chapter 4 (Specifically in Figure 4.7 - TLS model).

Photosynthetic pigment-protein complexes are particularly suitable as model systems for research on protein energy landscapes and dynamics utilizing optical methods. Chromophores are present in these complexes naturally, without extraneous manipulations, and in a wide variety of local environments. Recently, our group has published several papers where NPHB was employed to study the energy landscapes in light-harvesting antenna complexes [57], [58], [38]. In particular, for the CP43 antenna complex we demonstrated that the distributions of barriers on the protein energy landscape are Gaussian and not proportional to $\backsim 1/\sqrt{V}$ [38] (V is the barrier height). No evidence of $\backsim 1/\sqrt{V}$ distributions was observed in CP43. This was somewhat surprising since $\backsim 1/\sqrt{V}$ distributions were predicted and observed in glasses [32], [59], [60]; and a superposition of $\backsim 1/\sqrt{V}$ and Gaussian terms was observed for phycobilisomes [60]. We also developed the novel unified approach to joint analysis and modeling of both hole burning and hole recovery data, for fixed temperature and upon temperature variations. Importantly, the logic used in [38] to arrive at the conclusion about the Gaussian shape of the barrier distributions in CP43 was independent of any features specific to proteins and distinguishing them from other amorphous solids, e.g. organic glasses. This logic relied on the fact that in the presence of "spectral memory" the barrier distributions encoded into the non-saturated spectral holes and manifesting during the hole recovery (the "partial barrier distributions") differ from the full true barrier distributions (i.e., the distributions of all possible barriers on the relevant tier of the energy landscape, whether they are crossed in optical experiments or not). "Spectral memory" implies that spectral holes are recovered by the systems that had experienced NPHB returning to their pre-burn frequencies, and not by the systems that were out of resonance with the laser

in the beginning of the experiment and then evolved into resonance. The partial barrier distributions are vastly different for different shapes of the true full distributions, and one can easily distinguish their manifestations. In the light of these CP43 results [38] it was suggested that the earlier results on hole recovery in glasses [32], [59], [60] could be misinterpreted, due to ignoring spectral memory as well as the spontaneous recovery at burn temperature, and ascribing all recovery to barrier hopping. If anything, organic glasses are more likely to have the pigment molecule in interaction with just one two-level system (TLS; the special low-temperature properties of amorphous solids are ascribed to the presence of TLS [29], [61]) and to feature more perfect spectral memory than proteins with their multi-well energy landscapes. If true, this misinterpretation hypothesis would have far-reaching implications for the theories of amorphous solids at low temperatures [29], [61] yielding the $\backsim 1/\sqrt{V}$ barrier distributions. However, such a bold proposal obviously needed verification for other proteins and amorphous solids.

Additionally, even though we performed the experiments described in [38] on the red edge of the lowest-energy band of the CP43 complex in order to avoid any excitation energy transfer (EET)-related effects, CP43 is still a system of multiple relatively strongly coupled pigments [62], [63]. Thus, although EET from the lowest-energy pigment or delocalized state was forbidden, we could not be completely confident that our results are free of the excitonic effects. For instance, if the lowest-energy excited state is partially delocalized over several interacting pigments, any of these pigments may experience a spectral shift and local environment change triggered by optical excitation of this delocalized state. As different pigments of the CP43 complex are placed in somewhat different local environments, one cannot be fully sure that observed protein energy landscape parameters describe one particular pigment pocket of the protein and not a weighted sum of distributions for different pockets.

Cytochrome (Cyt) b_6f [12], [13], [14], [15], a complex containing just one chlorophyll *a* (Chl *a*) molecule per protein monomer (See Section 2.3.3 and Figure 2.7 in Chapter 2 for more details), represents a better model for protein energy landscapes research. It does not possess delocalized

Chl *a* states and potentially offers access to as uncontaminated optical manifestations of protein dynamics as possible. Cytochrome b_6f, existing in vivo in dimeric form, mediates the transfer of electrons between the two photosynthetic reaction center complexes, Photosystem II and Photosystem I, while also transferring protons across the thylakoid membrane from stroma to lumen. Most of the cofactors in Cyt b_6f are involved in these charge transfer processes, and absorb at different wavelengths with respect to the Chl *a*. The exact purpose of that Chl *a* in Cyt b_6f is unclear [13], [14], [15]. Cytochrome b_6f was explored by both frequency- and time-domain spectroscopies [13], [14], [15]. It was shown that at least at room temperature the Chl *a* in Cyt b_6f exhibits unusually short fluorescence lifetime ($\backsim$250 ps) and reduced fluorescence yield, which were attributed to effective quenching of the Chl excitations by the aromatic groups of the protein. This quenching is considered the most likely reason why presence of Chl *a*, although apparently useless from photosynthesis perspective, does not introduce any evolutionary disadvantage, and why Chl *a* remains preserved. Chlorophylls in Cyt b_6f appear well screened by protein from the outside environment. The Mg-to-Mg distance between the two Chl molecules of the dimer is 6.1 nm, rendering the interaction between those Chls very weak (dipole-dipole coupling $J_{12} \leq 0.4\ cm^{-1}$, depending on the dielectric constant) (See Figure 2.7). Below we are going to present the evidence of the slow excitation energy transfer between these two Chls. The main focus of this study, however, is on the protein energy landscapes. The unified approach of [38] is employed here to determine the shape and quantitative parameters of the barrier distributions, as well as the likely nature of the entities involved in conformational changes.

In addition, similar measurements were done on Cytochrome b_6f dissolved in deuterated environment in order to determine whether any parts of the observed dynamics in regular Cytochrome b_6f sample (dissolved in protonated environment), belong to the surrounding buffer-glycerol matrix and not to the protein itself. (In this case, the Cytochrome b_6f Complex was dissolved

in fully deuterated buffer/glycerol mixture with otherwise the same composition as in the original (protonated) sample.) Furthermore, in order to confirm that Chls are well screened from the outside environment, optical spectroscopy experiments were performed on Chl dissolved in buffer-glycerol matrix (both protonated and deuterated) with no protein. The results of these recent experiments are presented in Section 5.3.5 and Section 5.3.6 of this chapter.

5.2 Setup and Sample

Chloroplastic Cyt b_6f was isolated by Dr. Rafael Picorel from market spinach according to [64]. Two closely moving yellow bands were clearly observed around the middle of the sucrose gradient tubes but both bands showed similar absorption spectra with the same heme/Chl a ratio. The stoichiometry resulted in approximately one Chl a per Cyt b_6f monomer using an extinction coefficient of 20 $mM^{-1}{\cdot}\mathrm{cm}^{-1}$ for Cyt b (heme at 549 nm) as described in [64] and 75 $mM^{-1}{\cdot}\mathrm{cm}^{-1}$ for Chl a (at 668 nm) as described in [65] after sample reduction with sodium dithionite. For some experiments, the detergent n-octyl-β-D-glucopyranoside (OG) was replaced with n-dodecyl-β-D-maltoside (DM) in the final preparation by several dilution / concentration steps with 30 mM Tris/succinate, pH 6.5, and 0.03% (w/v) DM solution by centrifugation in 30 kDa MWCO Amicon tubes. Figure 5.1 depicts Cytochrome b_6f Complex solubilized with the help of the detergent micelle and placed inside water/glycerol mixture.

Absorption and broad spectral range hole spectra were measured with a Cary 5000 spectrophotometer with resolution of 0.1 nm. Broadband and selectively excited emission spectra and Δ-FLN (the difference of fluorescence line narrowed spectra before and after spectral hole burning) spectra were measured using Acton 2356 spectrograph with Princeton Instruments Pixis 1340 $\times$ 100 back-illuminated CCD. High-resolution spectra were measured with Sirah Matisse-DS frequency-stabilized tunable dye laser (bandwidth $<$ 1 MHz). A 6 W 532 nm Spectra Physics Millennia was used as a pump laser. The sample was placed inside a liquid-helium bath/flow

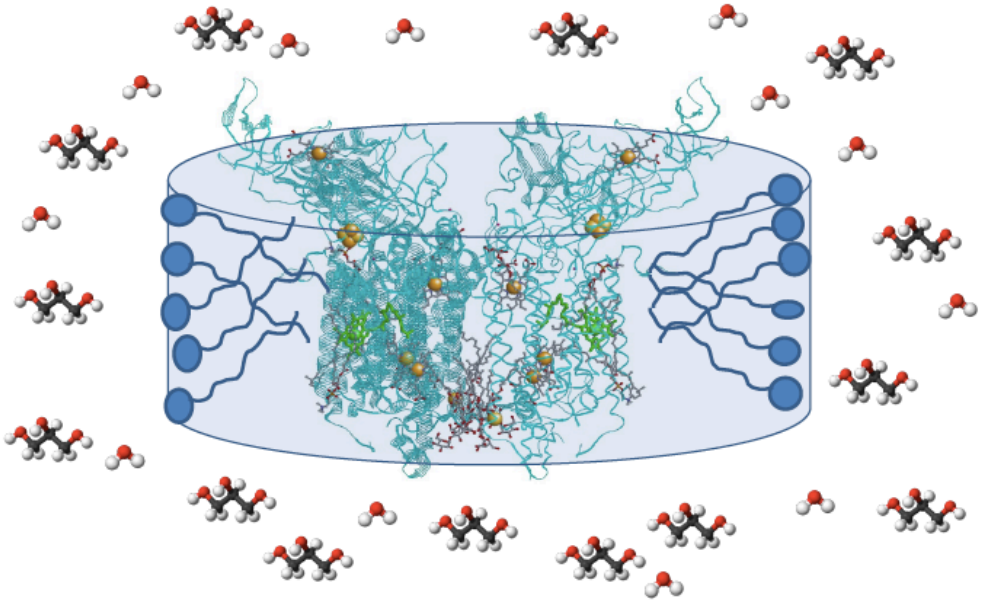

FIGURE 5.1: Cytochrome b_6f Complex solubilized with the help of the detergent micelle and placed inside water/glycerol mixture.

cryostat (Ukrainian Academy of Sciences) [66]. High-resolution experiments were performed in fluorescence excitation mode, with vertically polarized excitation light and fluorescence collected at 90 degrees with respect to the excitation and detected with a Hamamatsu photomultiplier / photon counting module. The intensity of excitation light was stabilized by BEOC laser power controller and regulated with neutral density filters. The scattered excitation light was suppressed by a 700 nm long-pass filter. The irradiance was typically $\backsim$ 17 $\mu W/cm^2$ for burning (unless otherwise specified); 500 times smaller irradiance was used for reading hole spectra. Thermocycling involves producing a spectral hole at low temperature (e.g., 5 K), temporarily increasing the temperature to a higher value, measuring the hole spectrum again at burn temperature, and then repeating the cycle with ever increasing maximal temperature. More details can be found in [58], [38].

The same method for sample preparation and the same experimental setup were used for the experiments on Cyt b_6f in deuterated environment. To make a deuterated environment, both

the water of the buffer and the glycerol were substituted by fully deuterated compounds (i.e. d_8 glycerol was used) purchased from C/D/N Isotopes Inc. Samples were stored at -80 °C and were unfrozen only immediately prior to the experiment. Thus, possible exchange of deuterons between solvent and protein was minimized.

5.3 Experimental Results

5.3.1 Absorption and Emission Spectra of Cyt b_6f

The absorption, emission and hole burning action spectra spectra of Cyt b_6f at 5 K are shown in Figure 5.2. An example of the low-resolution hole spectrum is also presented in grey in Figure 5.2 in order to show the shapes of zero-phonon hole, anti-hole and pseudo-phonon sidehole in non-photochemical hole burning. The shape of zero-phonon hole in the low-resolution spectrum suggests that the electron-phonon coupling is moderate in Cyt b_6f sample. The emission spectrum was measured using excitation with white light through a band-pass interference filter centered at 600 nm and with the bandwidth of 10 nm to ensure selective excitation of Chl a. The hole burning (HB) action spectrum, was measured in fluorescence excitation mode, shows the dependance of the hole depth on wavelength when the illumination dose is fixed for measurement. HB action spectrum can represent the site distribution function (SDF) of all the pigments in the simplest possible case when there is no heterogeneity and no excitation energy transfer (EET). However, it should be noted that this simple scenario is not valid for Cyt b_6f since in that case the absorption and emission spectra would be shifted to the blue and to the red of the action spectrum by the same amount, respectively, and would be of similar width. In case of Cyt b_6f, the sub-SDF of the most easily burnable pigments, which is represented by the action spectrum, is peaked at 674.6 nm with the width of 16.6 nm. Therefore, the HB

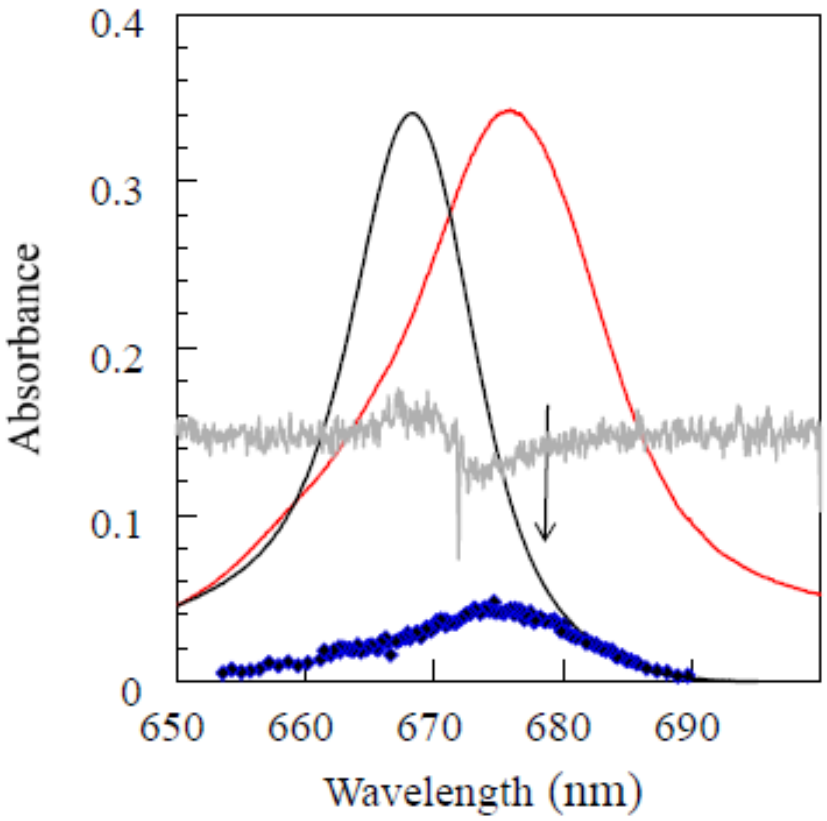

FIGURE 5.2: Absorption (black), emission excited at 600 nm (red) and SHB action (blue diamonds) spectra for Cyt b6f at 5 K. Also presented is an example of a low-resolution hole in the absorption spectrum (grey). Arrow indicates the burn wavelength for HGK and recovery experiments described in the text.

action spectrum matches the emission spectrum peaked at 675.9 nm. However, the absorption spectrum is peaked at 668.3 nm (Figure 5.2).

In addition, the emission and absorption spectra of Cyt b6f are both peaked $\backsim$ 2.2 nm to the blue with respect to the ones reported in [13]. However, the widths of the absorption (12.5 nm) and the emission spectra (19 nm) in our case are fairly similar to the ones reported in [13] (11.6 nm and 16 nm respectively).

It should be noted that the emission spectrum was significantly broader than the absorption spectrum as well according to [13]. The systematic difference in the positions of spectral peaks can be attributed to the fact that samples used in this study and in [13] belong to different

organisms (Spinach here and Synechocystis PCC6803 in [13]), to differences in isolation procedures (different detergents), as well as to Cyt b_6f in [13] being monomeric. (We confirmed that both absorption and emission spectra of samples with dodecyl maltoside instead of the octyl glucopyranoside (See Section 5.2) are red-shifted by about 1 nm, which means the difference between the results here and in [13] is reduced.)

5.3.2 Δ-FLN Spectra and Energy Transfer

The emission spectrum is in agreement with the HB action spectrum, given the parameters of the single-site spectrum and electron-phonon coupling derived from the data in Figure 5.3.

Figure 5.3 depicts the Δ-FLN spectra for several excitation wavelengths; those obtained with excitation at the red edge of the absorption band directly represent the single-site spectrum, and in particular the phonon sideband, according to [49]. The Δ-FLN spectrum is the difference between fluorescence line narrowing spectra before and after NPHB [49], [50]. Since the ZPL contributions to the original FLN spectra were saturated, we used independently measured maximal depth of the zero-phonon hole to estimate $S_{phonon} \approx 0.7$, as in [13]. The phonon sideband (PSB) is peaked at 24 cm^{-1}, also in agreement with [13]. The detailed discussion on simulating Δ-FLN spectra in the presence of EET is presented in [67]. Briefly, for long enough excitation wavelength (or in the absence of EET), the PSB of the Δ-FLN spectrum is nearly identical to the PSB of the single-site spectrum [49], [67]. The PSB in Figure 5.3 are sharp near the peak but have long tailing at higher frequencies and are not amenable to fitting with either a single lognormal curve [68] or a single half-Gaussian / half-Lorentzian curve as one-phonon profile for realistic values of S_{phonon}. As the focus of this work is not on the origins of this particular PSB shape, we used two components to produce a good enough single-site spectrum to be employed in subsequent modeling, one lognormal (S = 0.6), and one 24 cm^{-1} Lorentzian mode with S = 0.12. The lognormal part of the one-phonon profile is given by

$$l(\omega) = \frac{S}{\omega\sigma\sqrt{2\pi}} exp(-\frac{(ln(\omega/\omega_c))^2}{2\sigma^2}) \tag{5.1}$$

with ω_c being the cutoff frequency and σ being the standard deviation [68]. The parameters of the one-phonon profile are summarized in Table 5.1.

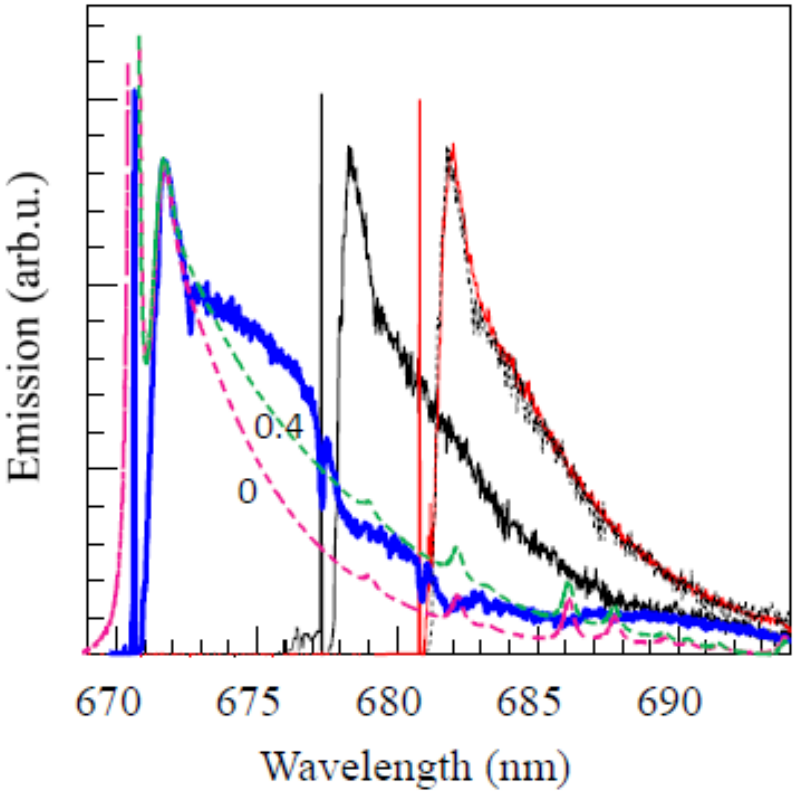

FIGURE 5.3: Noisy curves: Δ-FLN spectra obtained at 5 K with excitation at 670.7 (blue), 677.0 (black) and 680.8 (red) nm. The blue curve was measured after performing Δ-FLN experiments at 677.0 and 680.8 nm. The original FLN spectra were saturated at the excitation wavelength; their difference there was therefore zero and the spikes were artificially added to the Δ-FLN spectra to indicate the excitation wavelength. A copy of the black curve was shifted by 3.8 nm to the red to demonstrate that at longer wavelengths the shape of the Δ-FLN spectra is wavelength-independent. These spectra were fitted using the parameters reported in Table 5.1. Magenta and green dashed curves, respectively, are calculated Δ-FLN spectra for excitation wavelength of 670.7 nm and inter-pigment couplings J_{12} of 0 and 0.4 cm^{-1}. [67]

The single-site spectrum includes ZPL, PSB as well as contributions due to localized Chl vibrations. Multi-phonon processes are included according to [69] with modifications proposed

SDF peak / FWHM	**Lognormal PSB [68]; See Eq. 5.1: S, σ, ω_c, peak**	**24 cm^{-1} Lorentzian mode: S, width**
14840 / 350 cm^{-1}	0.60, 0.8, 65 cm^{-1}, 37 cm^{-1}	0.12, 20 cm^{-1}

TABLE 5.1: SDF and electron-phonon coupling parameters for the Cyt b_6f dimer (long lifetime fraction).

in [70] - in order to produce the R-phonon profile (R = 2, 3 ...), the one-phonon profile including lognormal $l(\omega)$ (Eq. 5.1), the 24 cm^{-1} Lorentzian mode, and the localized chlorophyll vibrations [50] was numerically convoluted with itself $R-1$ times, without approximations. R-phonon profiles for R = 1, 2 ... were added together with the weighting factors $S^R/R!$. The zero-phonon profile is a Lorentzian with the area normalized to $exp(-\Sigma S)$, where the sum is over all phonons and localized vibrations.

Large gap between the peaks of the absorption and emission spectra can be explained neither by large electron-phonon coupling (it is moderate, see above) nor by invoking excitation energy transfer between two identical Chls of the Cyt b_6f dimer, by analogy with the trimeric Fenna-Matthews-Olson (FMO) complex [71]. If the two Chls of the cytochrome dimer possessed identical true SDF, these would be peaked at about 669.5 nm. Following the logic of [67] and [71], one can calculate that the sub-SDF of the lower-energy pigments in the pair, corresponding to the action spectrum, would be peaked at about 671 nm, and have the width of about 10 nm. In other words, in a scenario involving only EET between two pigments with identical SDF, the emission spectrum and action spectrum are supposed to be narrower than the absorption spectrum, not broader, as it was indeed observed for FMO complex [71], for example. If EET is slow and some noticeable emission from the donor molecules is possible, the action and emission spectra would broaden (but not beyond the width of the absorption spectrum) and shift to the blue, not to the red. Besides, it appears that absorption spectrum cannot be fitted employing one Gaussian SDF, as it has significant long-wavelength tailing. The fluorescence lifetime for the fraction of the pigments dominating the emission spectra, including FLN, is significantly longer than 250 ps reported in [13], [14]. Figure 5.4 presents the dependence of the homogeneous line

width on temperature for $\lambda_B \approx 677$ nm. For every temperature five holes of different depths were burned, and the extrapolation to zero hole depth was performed. It is clear that the holes burned below 4 K are narrower than the 250 ps lifetime [13], [14] would permit (dashed horizontal line). The narrowest holes at 1.9 K correspond to the excited state lifetime of about $\backsim$ 700 ps. There is no evidence or physical reason why this temperature dependence of the line width should level off right at 1.9 K, which is just the minimal temperature accessible in our setup; more likely the width follows the $\backsim T^{1.3}$ dependence typical for amorphous solids and pigment-protein complexes below 5 K [72], [73], [74], [75]. Therefore, the fluorescence lifetime of Chls dominating emission is likely longer than 700 ps, quite possibly a couple of nanoseconds, typical for Chls in protein environment without additional quenching. Value of 2.5 ns was used for subsequent modeling. The blue curve in Figure 5.4 is only a guide for the eye. Due to somewhat limited temperature range we did not attempt to fit the data with a superposition of $\backsim T^{1.3}$ and $\backsim \exp(-\hbar\,\omega_{vib}/k_B\mathrm{T})$ terms, the latter being due to some low-frequency vibration possibly causing additional dephasing [72], [73], [74], [75].

In order to explain our observations we have to suggest that our cytochrome sample is somewhat heterogeneous. It is possible that in some fraction of our sample the fast quenching of the Chl excitations by the surrounding protein [13], [14] does not occur. Thus, there may be four categories of Chls rather than two (higher-energy donor and lower-energy acceptor): quenchable donors, quenchable acceptors, unquenchable donors and unquenchable acceptors; with the action spectrum representing mostly the latter. Quenchable pigments may still be in the majority, and contribute the most to the absorption spectrum; their SDF appears to be narrower than that of the pigments that cannot be quenched by the protein. However, quenchable pigments do not contribute much to the emission. Ignoring possible contributions of quenched pigments to the emission completely, one can demonstrate that the Δ-FLN spectra depicted in Figure 5.3 are in good agreement with $S_{phonon} \approx 0.7$ and inter-pigment coupling of $J_{12} \approx 0.4\ cm^{-1}$ (dashed green curve). Magenta dashed curve depicts the spectrum predicted in the absence

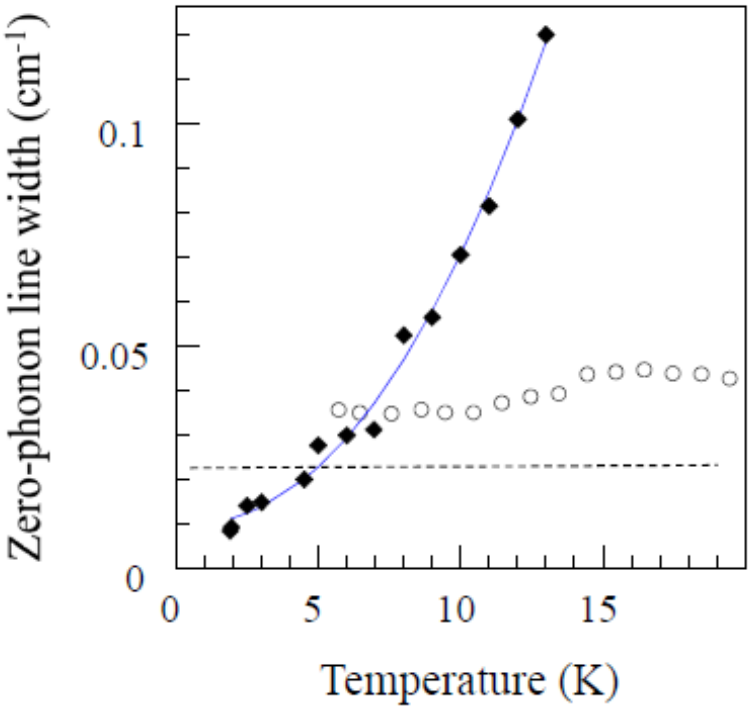

FIGURE 5.4: Black Diamonds: temperature dependence of the homogenous line width at around 677 nm. Five holes were burned at each temperature with varying illumination doses; results were extrapolated to zero hole depth. The horizontal dashed line corresponds to the 250 ps fluorescence lifetime reported in [13], [14]. Blue curve is a guide for the eye only. Also presented is the dependence of the homogeneous line width on thermocycling temperature for a 30% hole burnt at 5.5 K (open circles).

of EET. It should be noted that the presence of EET is further confirmed by the presence of previously burned spectral holes in the shorter-burn wavelength Δ-FLN spectrum (blue curve in Figure 5.3, excitation wavelength 670.7 nm). This experimental Δ-FLN spectrum contains zero-phonon holes, pseudo phonon sidebands and NPHB anti-hole features. Obviously, observing such previously burned holes in the Δ-FLN spectra would be impossible in the absence of EET [67]. One can also treat these results as a proof that the approach of [49] indeed predicts the Δ-FLN spectra correctly, i.e. that due to double spectral selection the Δ-FLN spectra do not contain significant pseudo-PSB contributions

5.3.3 Hole Burning and Hole Growth Kinetics

The hole growth kinetics (HGK) curves which were measured at burn wavelength λ_b around 677 nm and at several temperatures T are shown in Figure 5.5. As it was explained in details in Section 4.3 of Chapter 4, HGK curves show how the fluorescence signal decreases with time (or with the irradiation dose which is defined by product of constant laser power density and time) while the hole burning is happening at the fixed laser frequency ω_B. HGK curves depicted in Figure 5.5 actually represent $A(\omega_B, Pt)$ (normalized to $A(\omega_B, 0)$) which is defined by the hole burning master equation (Equation 4.10) for post-burn absorption spectrum.

In order to determine the parameters of the excited state λ distribution, one has to compare the experimental HGK curves with those simulated using Equation 4.10 (Figure 5.5). To simulate HGK with Equation 4.10, the attempt frequency in Equation 4.11 (Ω_0) has been taken as 7.6×10^{12} for the sake of easy comparison with the results obtained for glasses [76], [35], [77] and other pigment-protein complexes [57], [58], [38]. In addition, the fluorescence lifetime in the absence of EET (τ_{fl}) is assumed to be 2.5 ns here. The denominator of Eq. 4.11, in principle, can contain also the characteristic EET time. However, on the red edge of the band the absorption is dominated by the acceptor molecules, which are incapable of further downhill EET (See Figure 5.3 (where two longer-wavelength Δ-FLN spectra are identical) in Section 5.3.2 for further explanation).

As can be seen in Figure 5.5, the hole burning process is gradually slowing down with temperature. This slowdown is expected due to the increase of the homogeneous line width with temperature (depicted in Figure 5.4), accompanied by some increase of S_{phonon}(T) [69]. Both effects lead to the decrease of the peak absorption cross-section of the ZPL. However, unlike in CP43, at the higher temperatures the burning is somewhat faster than would follow from the above effects alone; see dashed red line in Figure 5.5(A). These discrepancies can be explained if one includes into consideration the temperature dependence of the rate of phonon-assisted

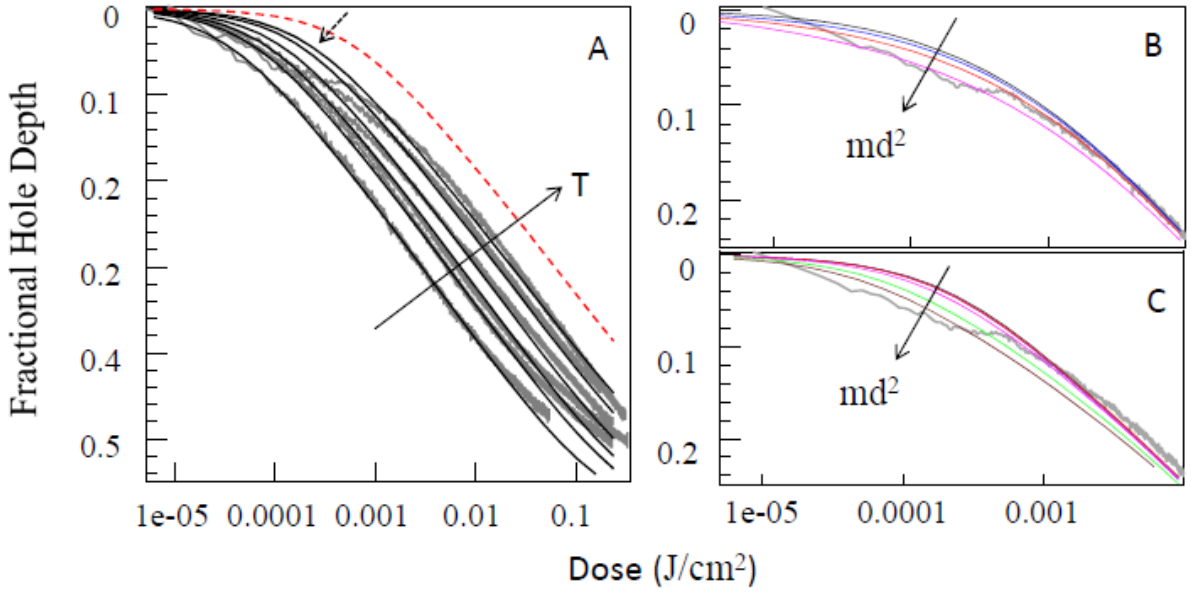

FIGURE 5.5: **Frame A:** HGK measured at 2, 5.5, 7.6, 9.6, 11.7 and 13.9 K (grey noisy curves) and their fits employing uniform λ-distribution with λ_{min} =8.2 and λ_{max} =12.2 and excited state TLS asymmetry of 4.5 cm^{-1} (smooth black curves). Dashed arrow indicates the region of discrepancy between experimental and modeling results, presumably due to the onset of hole burning via barrier-hopping. Dashed red line is the HGK curve calculated for T=13.9 K and no temperature dependence of the tunneling rate (i.e., for large TLS asymmetry). Burn wavelength was 677 nm. **Frame B:** Effects of barrier hopping on HGK for Gaussian λ-distribution demonstrated for the 13.9 K HGK; md^2=0.1, 1.0, 1.1 and 1.2 $\times$ 10^{-46} $kg{\cdot}m^2$, increasing in the direction of the arrow. **Frame C:** Effects of barrier hopping on HGK for uniform λ-distribution demonstrated for the 13.9 K HGK; md^2=0.1, 1.0, 1.1, 1.2, 1.3 and 1.35 $\times$ 10^{-46} $kg{\cdot}m^2$.

tunneling involving the shift to a deeper well of the energy landscape and an increase of the scattered phonon energy (downhill tunneling) Ω_0 exp(-2λ)(n(Δ)+1) that is slightly increasing with temperature. n(Δ) = 1/(exp(Δ/k_BT)-1) is the population number for phonons employed in phonon-assisted tunneling. Better global fit to all HGK curves can be achieved for TLS asymmetry $\Delta \approx 4.5\ cm^{-1}$. For CP43 [38] the average excited state TLS asymmetry apparently was larger, and thus the temperature dependence of the tunneling rate was less prominent.

The parameters of the λ-distribution obtained from the fit to the HGK curves are similar to those reported for CP43 [38] and other protein-chlorophyll complexes [57], [58] under similar conditions and assumptions. Namely, if f(λ) is Gaussian and temperature dependence of the tunneling rate is properly taken into account, $\lambda_0 = 10.25 \pm 0.10$ and $\sigma_\lambda = 1.3 \pm 0.1$ is obtained from the fits

to the HGK for fluorescence lifetime of 2.5 nanoseconds. This could be compared to λ_0 = 10-11 and σ_λ = 1.3-2.0 observed for other protein-chlorophyll complexes [57], [58], [38] and to $\lambda_0 \approx 8$ and $\sigma_\lambda \approx 1$ observed for aluminum phtalocyanine tetrasulphonate or free base phthalocyanine in a number of simple organic glasses and hyperquenched glassy water [76], [35], [77].

5.3.4 Hole Recovery

In order to determine the qualitative shapes of the λ- or barrier height distributions involved in NPHB and fixed-temperature hole recovery, we followed the logic of [38] and performed joint analysis of 5.5 K HGK data in Figure 5.5 and the 5.5 K recovery data presented in Figure 5.6(A). It should be noted that the holes that were initially shallower are recovering relatively faster. The difference in recovery of 20%- and 42%-deep holes is close to the maximal possible value predicted for the case of the perfect spectral memory (See Discussion in Section 5.4). In other words, recovery at 5.5 K is strongly dominated by the burned pigment-protein systems returning to the pre-burn configuration characterized by the original transition frequency of the pigment. The recovery curves were fairly repeatable. We also note that the recovery rate was independent on temperature between 5 and 10 K and slowed down somewhat at 13 K (not shown). As any process potentially responsible for the recovery has to accelerate with temperature, this indicates the increase of the NPHB rate with temperature (NPHB occurring while measuring with the small read intensity is slowing down the *apparent* recovery).

Presence of spectral memory justifies the use of partial λ-distributions (for hole recovery modeling) actually encoded into the holes, which are drastically different for Gaussian and uniform (corresponding to $\backsim 1/\sqrt{V}$ -shaped barrier distribution) full true λ-distributions [38]. The HGK data in Figure 5.5(A) was fitted also under the assumption of the uniform true full distribution of λ between λ_{min} =8.15 and λ_{max} =12.2. Then partial distributions of λ actually contributing to the non-saturated holes for both types of full true λ-distributions were calculated as in [38],

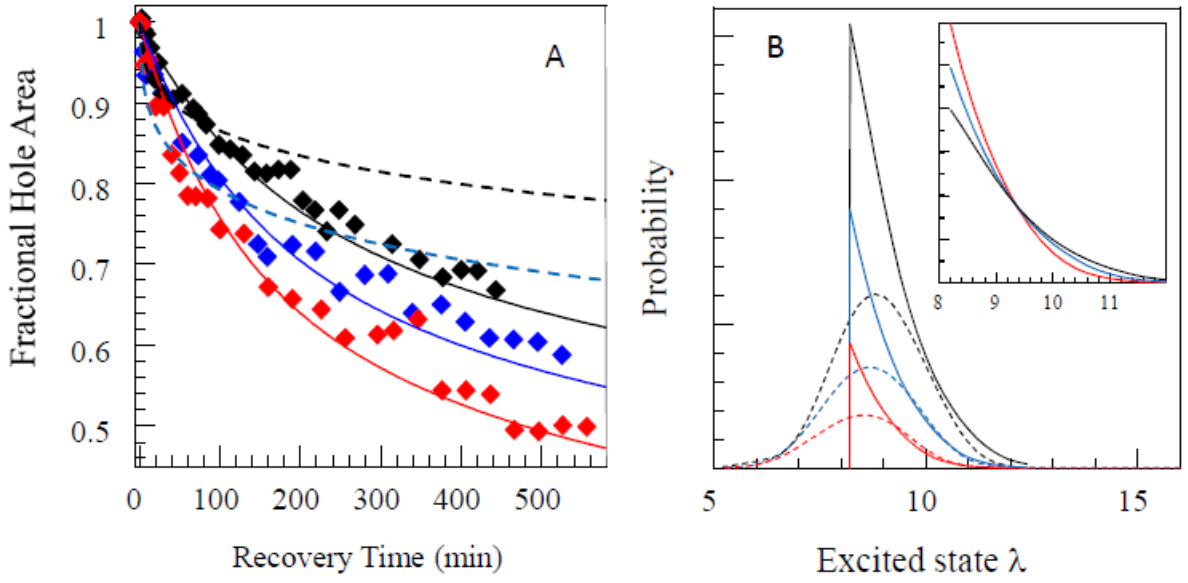

FIGURE 5.6: **Frame A:** Diamonds - measured recovery of 42% (black), 31% (blue) and 20% (red) holes at 5.5 K. Solid curves of matching colors - fits to the recovery curves obtained starting from uniform λ-distribution. Dashed black and blue curves - poor fits obtained starting from a Gaussian λ-distribution. See text for more details. **Frame B:** Partial λ-distributions for 20% (red), 30% (blue) and 40% (black) holes and the same parameters as used for fitting HGK curves. Dashed curves - partial distributions obtained for Gaussian full true λ-distribution. Solid curves were obtained for uniform true full λ-distribution. The insert in Frame B depicts the same partial excited state λ-distributions as in the main Frame B, but renormalized to the same area under the curve.

and simulated recovery curves were compared with the experiment. Figure 5.6(B) depicts the partial λ-distributions encoded into the spectral holes of various depths under the assumptions of uniform (solid lines) and Gaussian (dashed lines) true full λ-distributions with parameters given above. The insert depicts partial distributions in the uniform (box-like) true full distribution case, normalized to the same area under the curve. As the relative contribution of smaller-λ systems is larger for shallower holes, these holes are expected to recover faster. All recovery curves calculated for the uniform λ-distribution (black, red and blue solid smooth curves in Figure 5.6) were produced utilizing the same scaling factor k = λ_{ground} / $\lambda_{excited}$ = 2.35 ± 0.01. Thus, since $V \backsim \lambda^2$, barriers in the ground state are $2.35^2 = 5.5$ times higher than in the excited state, and the magnitudes of the ground and excited state barriers within one pigment-protein system are likely indeed well-correlated. Dashed curves were obtained starting from a Gaussian

true full λ-distribution. As can be seen from the comparison between experimental and calculated recovery curves, the full true ground-state λ-distribution is more likely uniform and not Gaussian (although the fit is somewhat imperfect for the uniform distribution as well). In the case of a Gaussian distribution faster initial recovery and slower recovery after a couple of hours are predicted (dashed curves).

Returning to Figure 5.5, one can also notice that even when the weak temperature dependence of the tunneling rate is taken into account, the hole burning above 10 K is somewhat too fast in the beginning, compared to the calculated HGK; see dashed arrow in Frame A. This effect is consistently present in several HGK curves in Figure 5.5, and for both assumptions about the λ-distribution shape. This may indicate an onset of an additional HB mechanism. Given the arguments presented above and justifying the use of the downhill tunneling approximation, it is unlikely that this additional process is uphill tunneling. Besides, any tunneling rate would increase with temperature uniformly for all λ, without any preference for the smaller ones that characterize individual systems that are the first to burn. The tunneling rate is a product of λ-dependent and temperature-dependent terms containing n(Δ), with asymmetry Δ being independent on λ. On the other hand, barrier hopping would indeed turn on selectively for smaller-λ (smaller barrier) systems first [38]. Evidence of both barrier-hopping and tunneling was found in single LH2 complexes between 5 and 18 K [78]. One can use the HGK curves to estimate the md^2 parameter of the entity involved in the conformational changes. Barrier hopping and tunneling contributions to hole burning are comparable when exp(-2λ) $\approx$ 2 exp(-V/k_BT) or $\lambda \approx \lambda^2\hbar^2/2md^2k_B$T. Contribution from barrier-hopping to the HB yield was incorporated into the hole burning modeling software and improved (but not perfect) agreement between HGK simulations and experiment was achieved. We need to mention, though, that this barrier hopping correction worked better when a Gaussian λ-distribution was employed (Fig. 5.5(B) versus Fig. 5.5(C)), in disagreement with the analysis of the recovery data in Figure 5.6. Best agreement can be achieved for md^2=1.15 $\times$ 10^{-46} $kg{\cdot}m^2$. This value is only 15% larger than

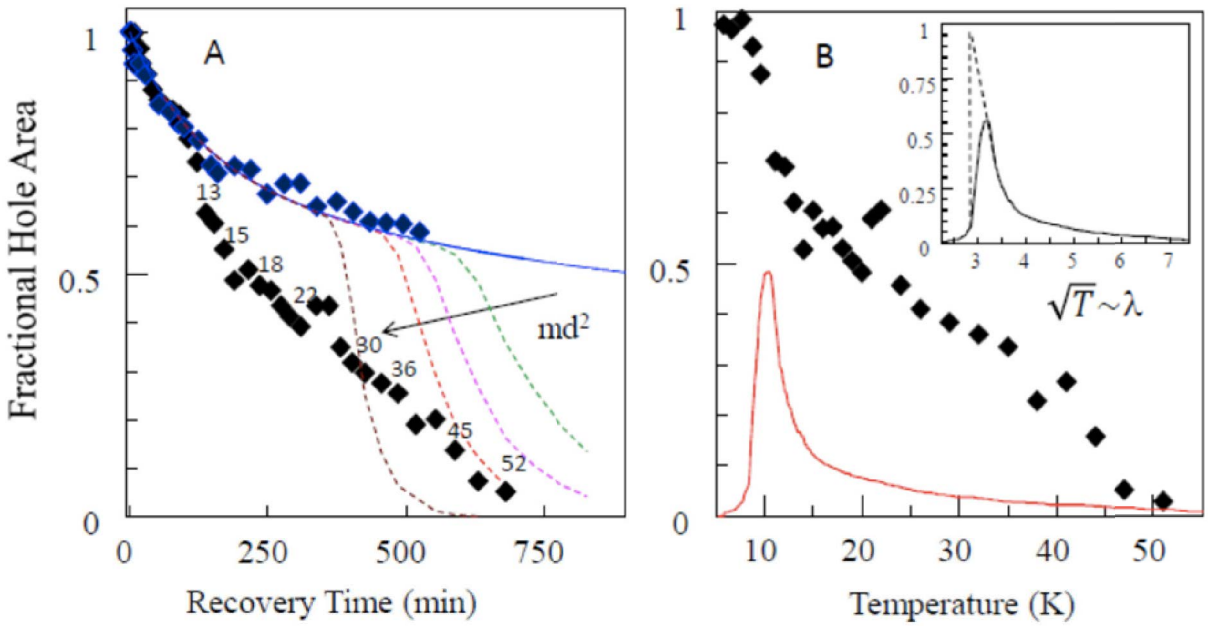

FIGURE 5.7: **Frame A:** The recovery of a 30%-deep hole upon thermocycling (black diamonds), compared to recovery at 5.5 K (blue diamonds) and its fit (blue solid line), as well as recovery curves calculated based on real temperature change profile for several different values of md^2 (dashed lines); md^2 is increasing from 1.0 to 1.15 to 1.3 to 1.9 $\times$ 10 ^{46} $kg{\cdot}\mathrm{m}^2$ in the direction of the arrow. Numbers above some of the datapoints indicate respective temperatures in Kelvin. **Frame B:** Black diamonds: recovery due to thermocycling corrected for recovery that would occur at 5.5 K anyway. Red curve: the distribution of barriers V corresponding to the recovery data. Insert: distribution as a function of $\sqrt{T} \backsim \sqrt{V} \backsim \lambda$.

the upper limit of md^2=1.0 $\times$ 10^{-46} $kg{\cdot}\mathrm{m}^2$ reported for CP43 [38]. While in the case of a Gaussian λ-distribution predominantly the beginning of the HGK was accelerated, for uniform λ-distribution the acceleration was more present for all stages of HGK. This makes perfect sense if one looks at Figure 5.6(B): Gaussian λ-distributions have the tails protruding towards smaller λ than the λ_{min} of the uniform λ-distribution, and small percentage of systems characterized by these small λ burn more exclusively in the beginning of the burning process. In contrast, for uniform λ-distribution the smallest-λ systems are characterized by larger $\lambda \approx 8.2$, and are less prone to barrier-hopping than the systems with $\lambda < 8$ from the Gaussian scenario.

Figure 5.7(A) depicts the recovery of a 30%-deep spectral hole upon thermocycling (black diamonds). It also contains the fixed-temperature 5.5 K recovery data and its fit (blue diamonds and solid line) and the results of modeling of thermocycling-induced recovery using the same

ground state λ-distribution parameters as obtained above for the fixed-temperature hole recovery, for several different md^2 values from 1.0×10^{-46} to 1.9×10^{-46} $kg{\cdot}\mathrm{m}^2$ (dashed curves). The horizontal axis of the Figure 5.7(A) presents time rather than temperature; the temperature is introduced indirectly via employing the actual temperature vs time profile used in the thermocycling experiment. Some temperatures are indicated next to their respective datapoints. Initial recovery (the first two hours, at temperatures below $\backsim$ 10 K; the first hour was spent at 5.5 K without thermocycling) follows the same path as in Figure 5.6(A). As can be seen from the comparison of experimental data and modeling results (dashed curves) experimental data is compatible with $md^2 \leq 1.4 \times 10^{-46}$ $kg{\cdot}\mathrm{m}^2$, but, as for CP43 [38], there appears to be an additional spectral memory-less recovery channel [38] (see additional discussion below). Larger md^2 values would not be allowed; crossing of the experimental and simulated curves (shown for md^2 =1.9×10^{-46} $kg{\cdot}\mathrm{m}^2$, black dashed line) would mean that the additional recovery is partially reversed with the increase of temperature, which is unphysical. Values of md^2 smaller than 1.0×10^{-46} $kg{\cdot}\mathrm{m}^2$ are, however, definitely possible.

Figure 5.7(B) shows recovery due to thermocycling alone, after taking corrections for recovery occurring anyway at 5.5 K. The barrier distribution involved can be obtained noticing that the fraction of systems remaining unrecovered after cycling to T_{max} is given by:

$$f = 1 - \int_0^{V(T_{max})} g(V)dV \tag{5.2}$$

with:

$$V(T_{max}) = k_B T_{max} ln(t_{max}\Omega_0) \tag{5.3}$$

where $g(V)$ is distribution of barrier heights, $t_{max} \approx 60$ sec is time spent at the peak cycle temperature T_{max} and Ω_0 is again the attempt frequency [79]. It is clear that $g(V)$ obtained from experimental data and sketched in Figure 5.7(B) is not Gaussian and resembles the results

of [32], [59], [60], where $g(V) \backsim 1/\sqrt{V}$ barrier distribution was deduced. A small plateau in the experimental data (diamonds) at the lowest temperatures can be explained by the smallest-barrier systems recovering due to tunneling during the first hour at burn temperature, before thermocycling started. The insert depicts the approximate shape of the λ-distribution involved in thermocycling-induced recovery. Dashed lines sketch the part of the λ-distribution ($\backsim$ 20% of the spectral hole area) that recovered during the first hour, before thermocycling was started. The shape of this λ-distribution resembles the shapes of the partial λ-distributions encoded into the holes in the case of perfect spectral memory and uniform true full λ-distribution (solid curves in Figure 5.5B). It is significantly different from either nearly Gaussian shapes (dashed lines in Figure 5.5B) or from box-like shape expected in the case of the uniform λ-distribution but no spectral memory (i.e. when partial barrier or λ-distributions encoded into the hole are identical to the full true ones).

Finally, we note that the hole broadens rather slowly upon thermocycling, and the width after cycling to temperatures exceeding 10 K is clearly smaller than the widths of the holes burned at respective temperatures (open circles in Figure 5.4). This indicates fairly slow spectral diffusion with small ($<< 1\ cm^{-1}$) spectral shifts [53], [80], [81] below 20 K corresponding to lower tier of the protein energy landscape in Figure 4.7. Overall, the dependence of the hole width on the maximal temperature of the cycle resembles that reported for phycobilisomes [81], except the linear (within experimental errors) increase of the hole width persists at least to 45 K when the hole is nearly recovered and the $\backsim T^{3/2}$ term [81] is not observed. Thus, reliable determination of the md^2 parameter for the entities whose conformational changes are responsible for the hole broadening in Cyt b_6f is unfortunately impossible. We can only conclude that it is smaller than $4.3 \times 10^{-46}\ kg{\cdot}\mathrm{m}^2$ or 26 $m_{proton}{\cdot}\text{Å}^2$ observed for phycobilisomes [81].

5.3.5 Cyt b_6f in Deuterated Environment

As it was mentioned earlier, all barrier distributions reported in the case of CP43 [38] appeared to be Gaussian and there was no evidence of $1/\sqrt{V}$ distributions that was predicted by the theories of amorphous solids, and was observed in glasses [32], [59], [60]. However, in the results that were so far presented in this study, only "glass-like" $1/\sqrt{V}$ barrier distributions were observed for Cyt b_6f, with very small, if any, Gaussian contributions. This rises a question of intactness of our Cyt b_6f samples. Although the results of Δ-FLN spectra presented in Section 5.3.2 suggest that our sample is relatively intact, we decided to address this issue in more details. In this case, the first question one might ask is what if the pigments in Cyt b_6f used in this study were exposed to the amorphous buffer/glycerol environment and true protein dynamics was not actually probed?

It is well known that spectral dynamics in many systems is sensitive to deuteration. In cases when the pigment was in direct contact with the deuterated environment, the slowdown of burning by a factor of hundreds and even thousands was observed [82], in agreement with the increase of the tunneling parameter λ from about 8 to about 11.2 (i.e. by a factor of $\sqrt{2}$ since mass of deuterium is twice the mass of proton. See Eq. 3.1), and as a result, a decrease in the tunneling rate which is proportional to exp(-2$\Delta\lambda$) (See Eq. 4.17). Fifteen-fold decrease of the NPHB yield was observed in R_1-line of $[Cr(oxalate)_3]^{3-}$ in deuterated ethylene glycol/water [83]. Thus, here we will explore if deuterated environment affects the spectral dynamics of Cyt b_6f.

First, the sample quality was checked by measuring its absorption and emission spectra, shown in Figure 5.8. The spectra of Cyt b_6f in deuterated environment closely resemble those for regular/protonated sample.

Then, the HGK were measured at the burning wavelength of $\backsim$ 677 nm at 5.5 K. Figure 5.9 shows the HGK curves obtained at 5.5 K for Cyt b_6f in regular/protonated (grey, light blue, pink curves) and deuterated (red, blue, black curves) environment. It should be noted that

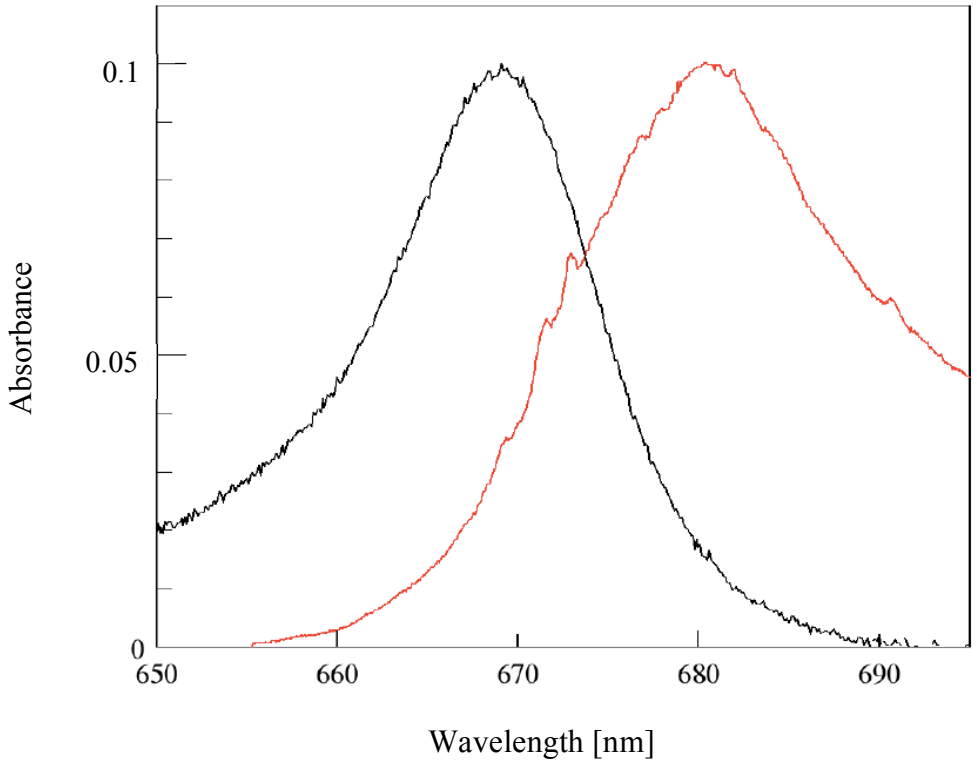

FIGURE 5.8: Absorption (black) and emission excited at 647 nm (red) spectra for Cyt b6f in deuterated environment at 5 K.

among the curves measured for deuterated sample, only the red curve is measured at a low light intensity and the blue and black curves were measured at higher light intensities. (The HGK curves of protonated sample were also measured at different intensities. However, it seems that the burning rate in protonated sample does not depend on the burning intensity while it slows down in deuterated sample when higher intensities are used. See Discussion in Section 5.4.1).

As can be seen in Figure 5.9, same burning rate is observed in both protonated and deuterated environment when a low light intensity is used to measure HGK in deuterted sample.

The next step is to analyze the hole recovery at the fixed temperature of 5.5 K. The hole recovery data for Cyt b_6f in deuterated environment is presented in Figure 5.10(B) and is compared to the recovery data for Cyt b_6f in regular/protonated environment (Figure 5.10(A)). According to the figures, the recovery has slightly slowed down in the deuterated sample (almost 30%). It should

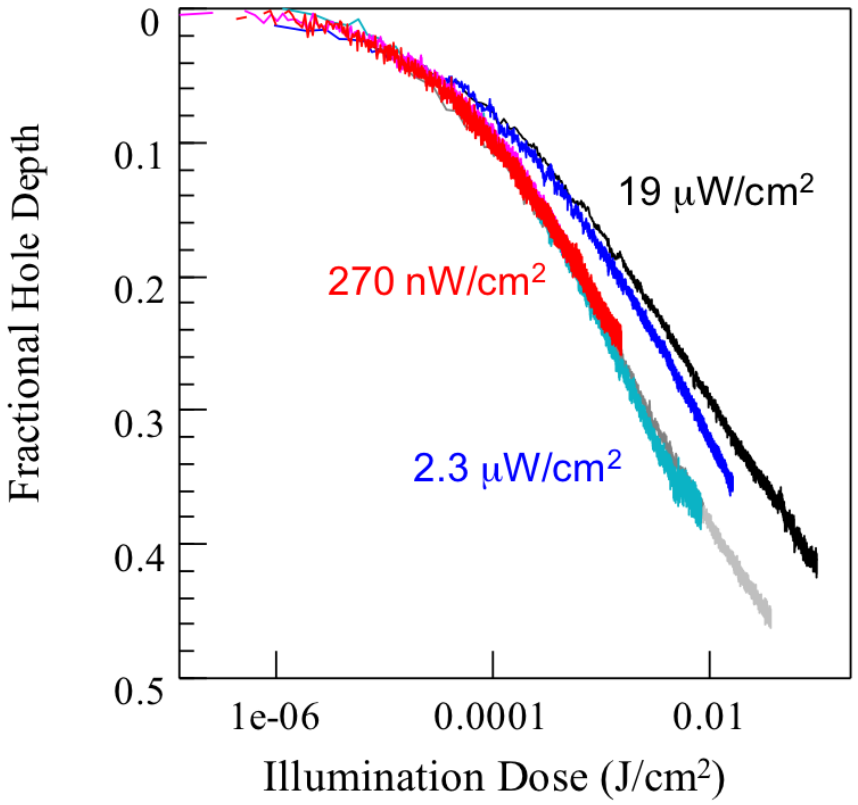

FIGURE 5.9: HGK measured at 5.5 K for Cyt b_6f dissolved in deuterated buffer-glycerol matrix (black, blue, red curves) compared to HGK curves (grey, light blue, pink curves) obtained at the same temperature for Cyt b_6f in protonated environment. For protonated environment the burning rate does not depend on illumination intensity, at least within the intensity range employed in our experiments. Same burning rate is observed for low enough burning intensity also in deuterated environment (red curve). However, burning rate slows down for higher intensities in deuterated environment (blue and black curves) (See Section 5.4.1).

be noted that the fixed temperature recovery (at 5.5 K) is due to tunneling in the ground state. In addition, the barriers in the ground state are higher than the ones in the excited state and as a result, λ is larger in the ground state. Therefore, if the ground-state dynamics observed in deuterated sample were affected by the deuteration, even for $\lambda_{ground} \approx 15$, more than 10^5 times slowdown would be expected in the recovery of the deuterated sample (λ_{ground} would increase to 21 (by a factor of $\sqrt{2}$) if the dynamics were dominated by protons of the outside buffer/glycerol environment, and as a result, tunneling rate would decrease according to Equation 4.17.). On the other hand, if the dynamics were dominated by OH group, 6% change of mass would occur

as a result of deuteration. In this case, λ would increase by only 3% (from 15 to 15.44) and the recovery would be 2.4 times slower. (See Discussion in 5.4.2 for more details about deuteration effects on the dynamics of Cyt b_6f.)

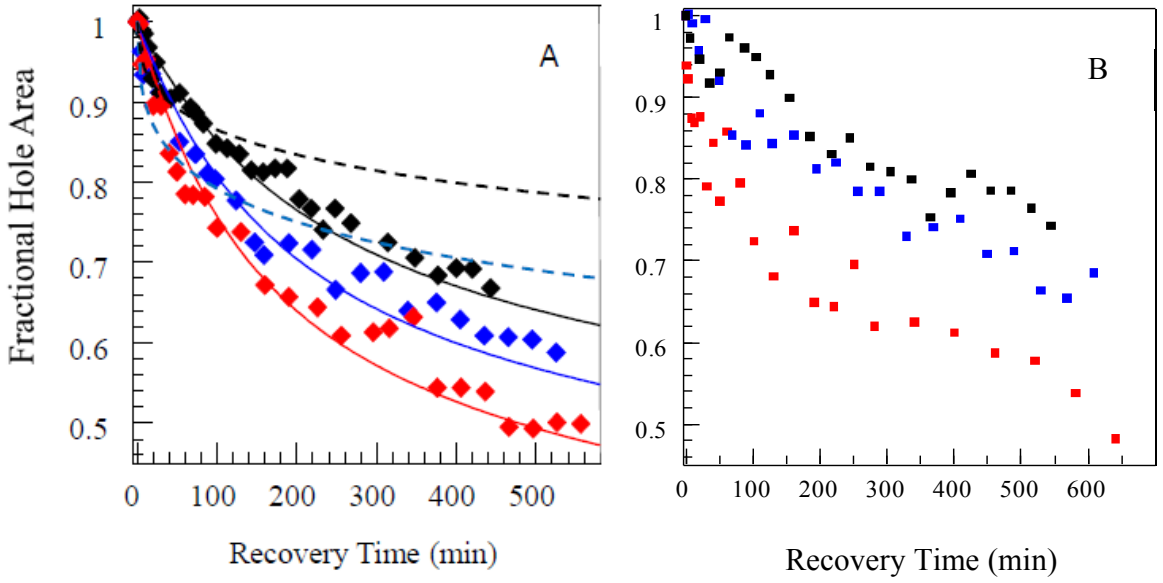

FIGURE 5.10: **Frame A:** Diamonds - measured recovery of 42% (black), 31% (blue) and 20% (red) holes at 5.5 K for Cyt b_6f in protonated environment. Solid curves of matching colors - fits to the recovery curves obtained starting from uniform λ-distribution. Dashed black and blue curves - poor fits obtained starting from a Gaussian λ-distribution. **Frame B:** Squares - measured recovery of 40% (black), 30% (blue) and 20% (red) holes at 5.5 K for Cyt b_6f in deuterated environment.

The observed slowdown of recovery might be because of the fact that a higher laser intensity was used for scanning the hole spectrum in deuterated Cyt b_6f experiments. Using a higher intensity light for reading in this set of experiments was required since the received signal from the sample was small (low concentration of sample). Therefore, some burning might have happened as a result of several scans and this slowed down the *apparent* recovery rate, specifically in the beginning of recovery at fixed temperature where the spectrum is measured more often (See the beginning of recovery measurements in Figure 5.10(B)). This effect is less important, although still present, when the time interval between two scans is 15-20 minutes (i.e. when the spectrum is scanned after temperature is elevated and then is lowered back to the

burning temperature in thermocycling experiments, and when the spectrum is measured less often in the fixed temperature recovery.). Burning while scanning occurs since too much light intensity prevents the smallest-barrier systems from recovering (i.e. not or burns them again), and slows the recovery down slightly.

The results of recovery upon thermocycling for deuterated sample are shown in Figure 5.11(B) and are compared to the thermocycling results for the protonated sample (Figure 5.11(A)). In addition, several high-resolution spectral holes (as an example of raw data) are presented in Figure 5.12.

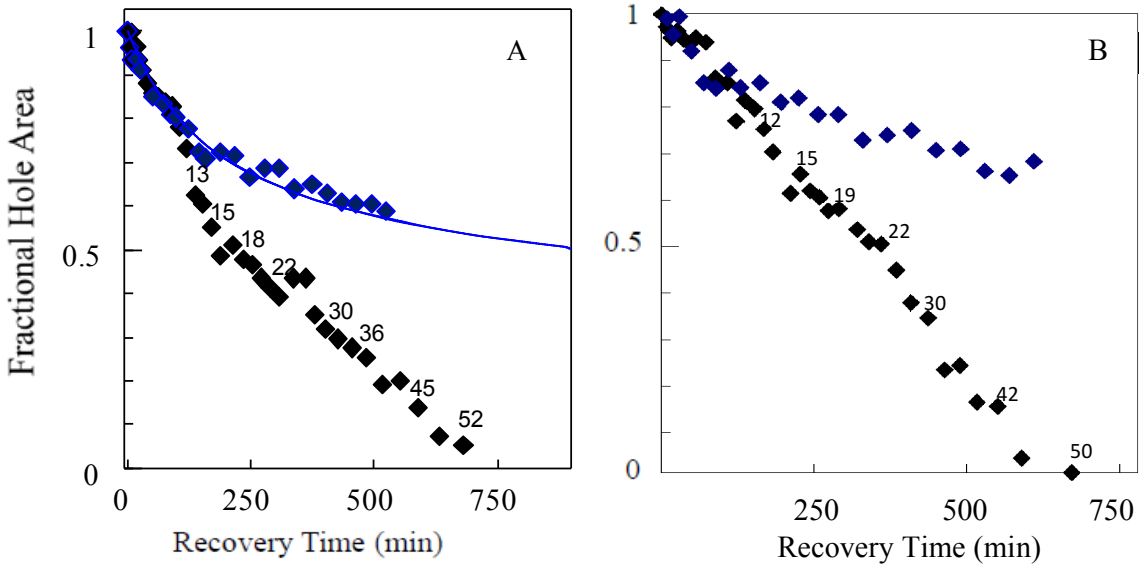

FIGURE 5.11: **Frame A:** The recovery of a 30%-deep hole for Cyt b_6f in protonated environment upon thermocycling (black diamonds), compared to recovery at 5.5 K (blue diamonds) and its fit (blue solid line). Numbers above some of the datapoints indicate respective temperatures in Kelvin. **Frame B:** The recovery of a 30%-deep hole upon thermocycling (black diamonds), compared to recovery at 5.5 K (blue diamonds) for Cyt b_6f in deuterated environment. Numbers above some of the datapoints indicate respective temperatures in Kelvin.

The data on recovery upon thermocycling are similar in both deuterated and protonated samples. It should be noted that barrier-hopping, that does not depend on the mass of tunneling entity, is the responsible mechanism in recovery upon thermocycling for higher temperatures. Nevertheless, similarity indicates that same type of the distribution, with same entity crossing

similar barriers, is explored in experiments on cytochrome b_6f in both protonated and deuterated environments.

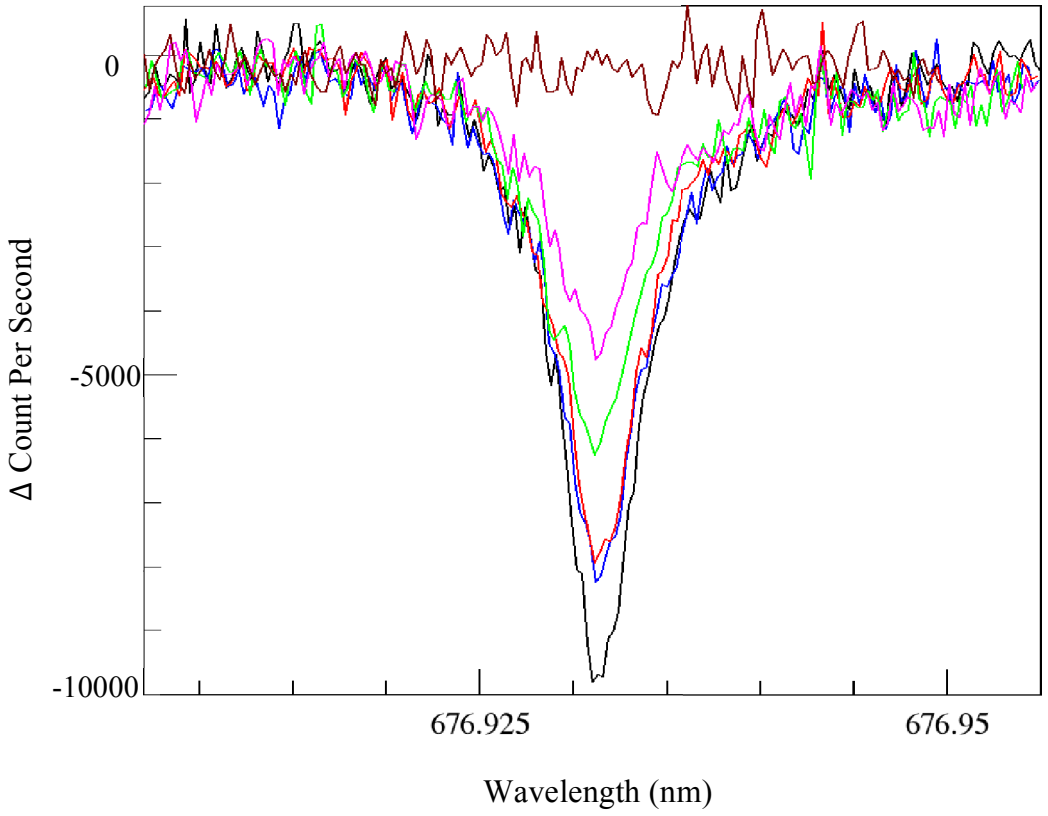

FIGURE 5.12: High resolution spectral holes showing the recovery of a 30% deep-hole that were measured during the thermocycling experiment for Cyt b_6f in deuterated environment. The hole was burnt at 5.5 K with the burning wavelength of $\backsim$ 676.932 nm. Black: first hole spectrum after hole burning; Blue: hole spectrum after the hole was recovering for about 1 hour at fixed burning temperature 5.5 K; The rest of the hole spectra were measured when the temperature was lowered back at 5.5 K after the temperature was elevated to the maximum temperature of 7.5 K (red), 12 K (green) and 14 K (magneta). Brown spectrum is the final scan when the hole was almost recovered.

Thus, pigments in Cyt b_6f appear to be very well screened from the amorphous outside matrix by the surrounding protein, and the dynamics that is probed in NPHB and recovery experiments for both deuterated and protonated samples belong to the protein.

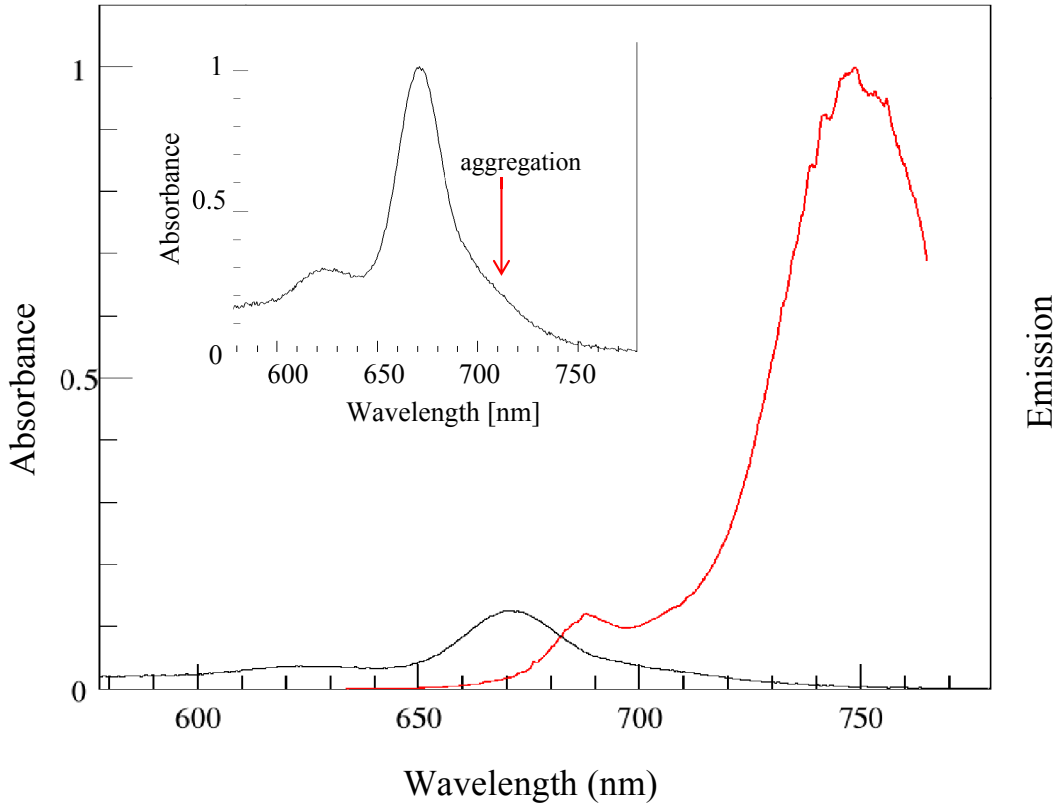

FIGURE 5.13: Absorption (black) and emission (red) spectra for Chlorophyll a in deuterated buffer-glycerol matrix at 5 K. The maximum peak of emission spectrum at 750nm belongs to the aggregates which are highly fluorescent and monomer fluorescence at about 680nm seems to be very strongly quenched. Inset depicts the absorption spectrum of Chlorophyll in deuterated solvent separately. The peak (in the inset) is normalized to one in order to show the aggregation clearly (red arrow).

5.3.6 Chlorophyll in Water/Glycerol Environment

We have also attempted to perform similar experiments and measurements on Chlorophyll *a* dissolved in water-glycerol mixture in order to determine the dynamics of this system without protein and to confirm that Chls in Cyt b_6f Complex are well screened from the outside solvent environment. The results show that Chlorophyll in water-based mixtures is subject to aggregation. The inset in Figure 5.13 shows the aggregation effect in the absorption spectrum of Chl dissolved in deuterated glassy matrix. The absorption (black) and the emission (red) spectra of Chl in deuterated buffer-glycerol mixture are also presented in Figure 5.13. As it can be seen,

aggregates are highly fluorescent (the maximum peak in the fluorescent spectrum at 750nm belongs to the aggregates) and monomer fluorescence seems to be very strongly quenched. As a result, we decided to detect fluorescence from 690-710 nm region only in fluorescence excitation experiments. The SHB experiment was performed on Chl in glassy matrix at 5 K. However, a massive slow down in hole burning was observed compared to the hole burning in Cyt b_6f samples ($\backsim$ 1000 times slower burning for Chl in sloution). The slowdown of hole burning is consistent with a combination of a) fluorescent lifetime reduced by quenching, and b) line width increased by quenching, with corresponding decrease of the peak absorption cross-section (assuming integral absorption cross-section stays the same).

5.4 Discussion

5.4.1 Evidence of EET and Intactness of the Cyt b_6f Samples

Good agreement between inter-pigment coupling values obtained from the structural data and from simulations of the Δ-FLN spectra, as well as other evidence of EET (holes in the Δ-FLN spectra in Figure 5.3), suggest that Chl molecules not exhibiting fast quenching and dominating fluorescence and fluorescence excitation spectra are not randomly non-specifically bound to the protein or released into the buffer-glycerol solution. They are likely still located within their designated protein pockets, but the fast quenching mechanism is turned off. Interestingly, the same arguments must be to a significant degree true also for the monomeric Cyt b_6f sample reported in [13], otherwise the relationship between absorption and emission spectra for that sample would be significantly different. In particular, the emission spectrum would have approximately the same width as the absorption spectrum, and would not be significantly broader. It is possible that quenching of Chl excitations is associated with conformational changes whose barriers are too high to cross at cryogenic temperatures. (The 250 ps lifetime [13], [14] was reported at

room temperature.) The hole burning and recovery rates are also typical for pigment-protein complexes and not for pigments in organic glasses.

In addition, as it was shown in Section 5.3.5 (Figure 5.9), the burning rate of Cyt b_6f dissolved in deuterated environment is similar to the burning rate of protonated sample for low burning light intensity. Also, the fixed-temperature recovery in both protonated and deuterated samples were not significantly different. The fact that the fixed-temperature recovery slows down slightly in deuterated sample unlikely indicates the influence of outside buffer/glycerol environment. The host deuteration effects on the hole recovery would have been significant, which is definitely not the case in our observations (See 5.3.5).

However, the HB rate in the deuterated sample appears to be somewhat intensity-dependent, with hole burning slowing down with increasing intensity. This effect was shown in Figure 5.9. In principle, apparent HB rate may be affected by changes in the balance between hole recovery occurring during burning (intensity-independent process) and burning process per se. However, in this scenario one would expect faster burning (as a function of J/cm^2, not W/cm^2) for higher intensity. Same photon flux is delivered in a shorter time, tilting the balance in favor of more net burning.

It has been noticed for both CP43 [38] and Cyt b_6f in protonated environment that hole burning slows down with the increase of temperature, in agreement with the homogeneous line width increasing with temperature and the peak absorption cross-section decreasing accordingly. Same behavior was observed also for Cyt b_6f in deuterated environment. Thus, observed slowdown of burning with increasing intensity may be explained by local heating of the immediate protein environment of the chlorophyll molecules by several kelvins (with respect to the "global" temperature (5.5 K) of the sample measured by the macroscopic sensor). Why is this effect sensitive to the environment outside the protein? For this effect to occur, the heat conductivity of the protein has to be higher than that of the outside environment in either case, and the bulk

thermal conductivity and/or the interface conductance has to be lower for deuterated outside environment.

We have explored various scenarios in order to address the heat conductivity issue observed in deuterated sample, such as calculating the approximate heat conductivity of deuterated Cyt b_6f, possibility of heating the whole illuminated volume of the sample, etc. However, the obtained results were not realistic and feasible. As an example, unrealistically low values of thermal conductivity for water-glycerol mixtures are required in order to explain the local heating of the Cyt b_6f protein by several Kelvin at low illumination intensities and protein concentrations employed here. However, there is one scenario that seems to be more plausible than the other ones. The latter involves the possibility of high thermal resistance of the interface between (non-modified, protonated) protein and deuterated outside environment, for instance due to acoustic mismatch. In case of acoustic mismatch, there would be a thermal resistance at the interface, and as a result, a temperature jump will occur through the interface [84]. It should be noted that in any case, if the Chls of Cyt b_6f were sensitive to the outside solvent environment, more drastic slow down in hole burning rates would have occurred compared to the slow down that is actually observed in our measurements, even for different intensities. Therefore, lack of such a significant decrease in the hole burning rate confirms that pigments in Cyt b_6f are not sensitive to the surrounding solvent. (It should be noted that this argument is true with protons as tunneling entities. See Section 5.4.2.)

Furthermore, the NPHB experiments performed on Chlorophyll *a* dissolved in buffer-glycerol matrix confirm that the Chlorophylls of Cyt b_6f Complex were not exposed to the outside environment (solvent) (See Section 5.3.6). The fluorescence of monomeric chlorophylls (at about 680 nm) in direct contact with water appears very strongly quenched, line width of spectral hole is increased and the hole burning slows down drastically. The fluorescence of aggregated chlorophylls, on the other hand, is peaked at 750 nm.

Summarizing, we are confident that lower-energy higher fluorescence yield Chls of the Cyt b_6f dimer are suitable probes for protein dynamics (rather than surrounding solvent dynamics) exploration.

5.4.2 Protein Energy Landscapes - Details of the NPHB and Recovery Mechanism

The weak temperature dependence of the HB yield (or no such dependence in the case of CP43 [38]) is not compatible with the weighted sum of downhill and uphill tunneling processes corresponding to the thermal equilibrium or even to the situation with equal probabilities of uphill and downhill tunneling (flash-frozen higher-temperature equilibrium). In both these cases the expected temperature dependence would be stronger than observed. Figure 5.14 shows expected temperature dependence of the tunneling rate in all these scenarios. Downhill tunneling (black curve, a) has the smallest ratio of tunneling rates at T $>$ 0 and T = 0.

The predominance of the downhill tunneling as the hole burning mechanism reflects an unnatural anti-equilibrium situation where the majority of the deepest wells of the TLS are not occupied. Thus, explaining the results presented here and for CP43 [38] requires invoking, for proteins, of an analog of the Shu-Small NPHB mechanism [85]. In this mechanism, the excited state of the TLS involving the pigment (analog of the "extrinsic TLS" in glasses) gets poised for downhill tunneling due to the diffusion of free volume associated with excitation-induced transitions in the "intrinsic" TLS. Our ability to burn zero-phonon holes to maximal depth allowed by electron-phonon coupling S_{phonon} ($\backsim$ 50% for $S_{phonon} = 0.7$) even below 2 K further confirms the presence of the Shu-Small mechanism [85] of NPHB in Cyt b_6f (and CP43, where up to 70% zero-phonon holes were possible with $S_{phonon} = 0.35$).

The results of the joint analysis of the HGK and fixed-temperature recovery data suggest the presence of nearly perfect spectral memory. In the absence of spectral memory the holes of

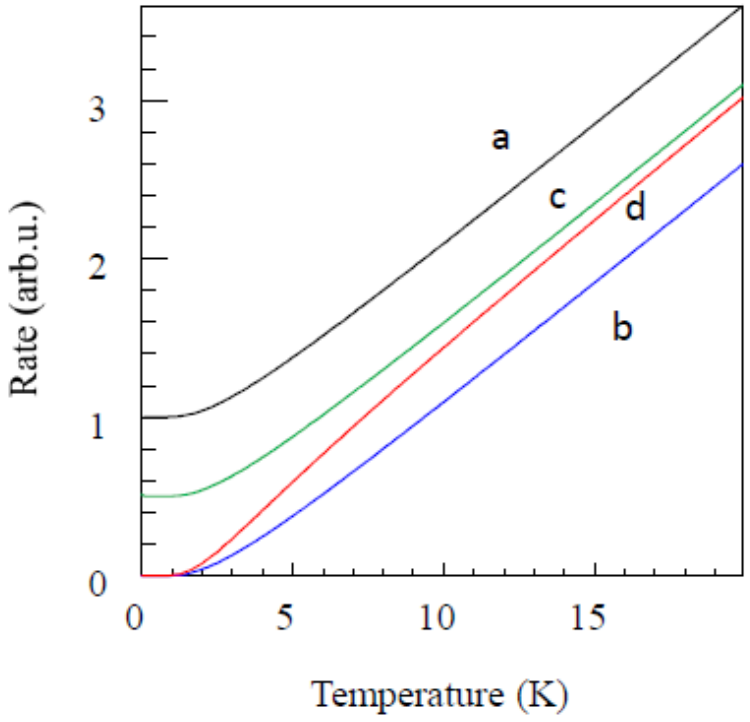

FIGURE 5.14: The temperature dependence of NPHB rate for downhill tunneling (black, a), uphill tunneling (blue, b), average of uphill and downhill tunneling - flash-frozen higher-temperature equilibrium (green, c), and the weighted average of uphill and downhill tunneling at thermal equilibrium at the respective temperature (red, d).

different depths would recover with the same relative speed, contrary to what is shown in Figure 5.6(A). It should be noted that the "lack of spectral memory" should not be understood as each system possessing an infinite number of available conformational sub-states. It merely means that the hole may be filled by absorption of the molecules which were not in resonance with the laser prior to burning. Let us discuss a somewhat oversimplified no-memory model where hole depth is proportional to the hole area and where there are N molecules absorbing at any wavelength around the burn wavelength before burning, and assume that all protein / pigment systems are M-sub-state systems, so every system can be in one of M different conformational sub-states. ($M = 2$ corresponds to a classical TLS, two level system.) Thus, there are total molecules in the ensemble, which have one conformational sub-state (occupied or unoccupied) resonant with the laser. Suppose the rate of spontaneous switching between

any two sub-states is k and that current number of molecules still at resonance after burning is $P(t)$. Then the number of molecules out of resonance which potentially can switch to resonance would be $MN - P(t)$. Division by $M - 1$ in subsequent equation reflects the fact that only one out of $M - 1$ wells available for transitions from an out-of resonance sub-state is the resonant one.

$$\frac{dP(t)}{dt} = k\frac{(MN - P(t))}{M-1} - kP(t) = k(N - P(t))[\frac{M}{M-1}] \tag{5.4}$$

$$U(t) = N - P(t) \tag{5.5}$$

$$U(t) = U(0)exp(-k[\frac{M}{M-1}]t) \tag{5.6}$$

Here $U(t)$ is the number of molecules that are removed from the resonance at time t, $U(0)/N$ is the fractional hole depth immediately after burning. While plotting normalized recovery data as in Figure 5.6(A), we essentially are plotting $U(t)/U(0)$. In the absence of spectral memory this quantity does not depend on the initial fractional hole depth regardless of the number of available sub-states M, at least for simple topologies of the protein energy landscape, and including $M = 2$.

Next we will address the issue of the additional thermocycling-induced recovery mechanism that cannot be accounted for using the same barrier distribution as manifests during the fixed-temperature recovery (see Figure 5.7). Modeling of NPHB and recovery processes employing multi-well energy landscapes of different shapes and in the samples in or out of thermodynamic equilibrium [86] does not yield anything resembling the observed gradual recovery upon thermocycling. Since this additional recovery mechanism cannot be explained within the model involving even the realistic imperfect spectral memory, the respective distribution of the barriers has to be the true full barrier distribution for another tier of the protein energy landscape, as was suggested for CP43 [38]. Yet the λ-distribution sketched in the insert of Figure 5.7(B)

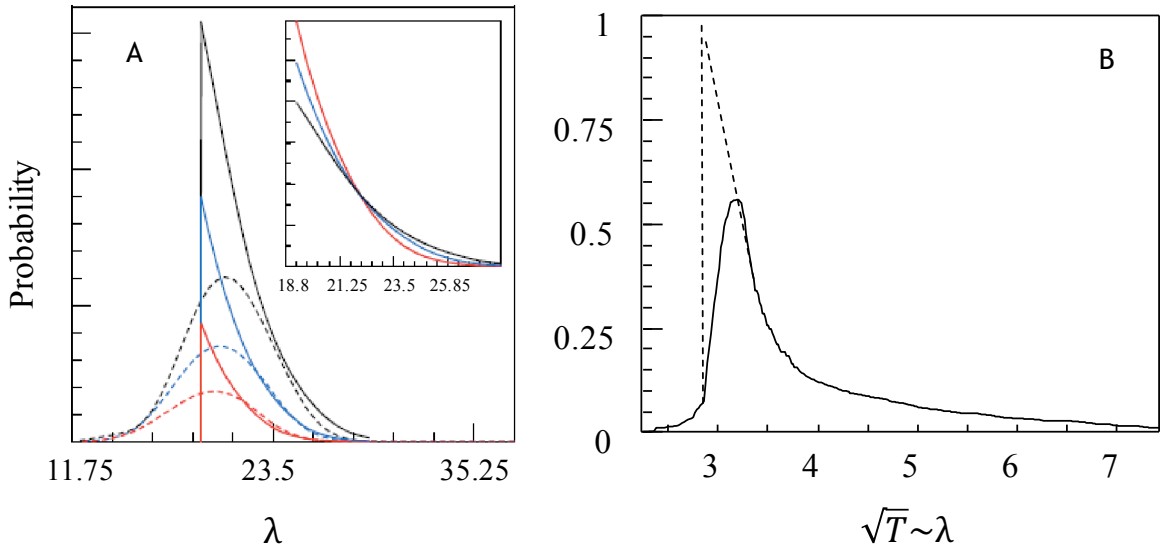

FIGURE 5.15: **Frame A:** Solid Curves: Partial ground state λ-distributions for 20% (red), 30% (blue) and 40% (black) holes. Dashed curves: partial ground state distributions obtained for Gaussian full true λ-distribution. Solid curves were obtained for uniform true full λ-distribution. The insert in Frame A depicts the same partial ground state λ-distributions as in the main Frame A, but renormalized to the same area under the curve. **Frame B:** Solid Curve: Partial ground state λ-distributions for 30%-deep hole obtained from recovery upon thermocycling data. Dashed lines: The part of the λ-distribution ($\backsim$ 20% of the spectral hole area) that recovered during the first hour, before thermocycling was started.

looks a lot like the partial distributions encoded into the non-saturated holes in the case spectral memory is present (solid curves in Figure 5.6(B)), except for the incorrect ratio of $\lambda_{ground,min}$ to $\lambda_{ground,max}$ (See Figure 5.15). In retrospect, this might have been true for CP43 [38] as well, except in the case when both true full and partial λ-distributions were close to Gaussian it was more difficult to notice.

At this point one may ask if it is possible to find a set of parameters that would explain all HGK, fixed temperature recovery and thermocycling results without invoking any additional tiers of the energy landscape and/or recovery channels. The following argument was proposed in our published paper on Cyt b_6f in protonated environment [37]: From the data in the inset of Figure 5.7(B) (or Figure 5.15(B)) it follows that $\lambda_{ground,max} \approx 2.6\lambda_{ground,min}$. On the other hand, in order to explain both HGK and fixed-temperature recovery, one still has to assume that $\lambda_{ground,max} = (\lambda_{exc,max} - \lambda_{exc,min}).k + \lambda_{ground,min} \approx 9.4 + \lambda_{ground,min}$, where the scaling

factor $k = \lambda_{ground}/\lambda_{exc} = 2.35 \pm 0.01$ (see above). From here $\lambda_{ground,min} \approx 5.9$, $\lambda_{ground,max} \approx 15.3$, $\lambda_{exc,min} \approx 2.5$ and $\lambda_{exc,max} \approx 6.5$. The average λ_{exc} is about 4.5. These unusually low values of λ can still be in agreement with the fits to the HGK and fixed temperature recovery data if the attempt frequency is reduced accordingly by a factor of about $(e^2)^{10.2-4.5} \approx 9 \times 10^4$, to as low as 85 MHz. Then one can utilize the data in Figure 5.7(B) to determine of md^2 using the method outlined in [79] i.e., assuming that both fixed-temperature and thermocycling-induced recovery reflect one and the same barrier distribution. With reduced attempt frequency, $ln(t_{max}\Omega_0) \approx 22$, $V_{max,ground} \approx 790\ cm^{-1}$ and $md^2 \approx 0.8 \times 10^{-46}\ kg{\cdot}m^2$. This value is again very close to those presented above and for CP43 [38]. For $md^2 \approx 1 \times 10^{-46}\ kg{\cdot}m^2$ (or 6 $m_{proton}{\cdot}Å^2$) if tunneling involved a proton, the distance d would be 2.44 $Å$, which is a typical hydrogen bond length. However, in the case of tunneling within a sufficiently long hydrogen bond yielding double-well potentials, values of d several times smaller than the hydrogen bond length were suggested [87], [88]. For a methyl or a hydroxyl group $md^2 \approx 1 \times 10^{-46}\ kg{\cdot}m^2$ would lead to $d = 0.63$ or $0.59\ Å$, respectively. These numbers are comparable to deviations of the soft regions of protein from equilibrium positions according to X-ray scattering [89], [90]. If the above arguments in favor of the reduced attempt frequency are correct, they would further support larger m and smaller d options for the tunneling entity. However, it is unclear how one could justify an attempt frequency four orders of magnitude lower than the typical vibration frequencies. It was estimated, based on the typical values of protein compressibility [91], that the chromophore-to-TLS distance $R \backsim 1$ nm, $\Delta R\ /\ R \backsim 10^{-3}$ and the net charge of the shifting entity equal to the charge of a proton correspond to spectral shifts of several wavenumbers [80]. Thus, $d \approx \Delta R$ can be as low as 0.01 $Å$ for NPHB to still be observable in the case of proton tunneling. However, respective increase of m by a factor of $\backsim 10^4$ would result in an attempt frequency decrease by $\backsim 10^2$ only, and would be incompatible with tunneling entities being protons.

In the most general terms, reduction of the attempt frequency could result from the cooperative effects, involving the whole network of weak interactions holding the protein together. One possible way to look at the cooperative effects reducing the attempt frequency employs the quantum-mechanical analog of beats. Imagine multiple oscillators with similar microscopic structure and similar but non-identical frequencies. If initiating a conformational change requires all these oscillators to be in phase simultaneously, this condition will be satisfied much less frequently than the period of each individual oscillator and the effective attempt frequency will be reduced. The cooperative rearrangements could include movements of either protons (explaining the sensitivity of Photosystem I (PSI) dynamics to deuteration [92]) or other, more massive, entities, or both. Of course, in this scenario m and d become disconnected from the actual mass and displacement of some one particular entity. Cooperative effects are also in line with the presence of Shu-Small NPHB mechanism [85] in proteins as suggested above, with some additional conformational changes poising the "extrinsic TLS" for downhill tunneling. The coupling between multiple structural features of the protein at cryogenic temperatures was inferred from the hole broadening experiments in protoporphyrin-IX-substituted myoglobin [93]. Another likely example of cooperative effects in spectral dynamics of pigment-protein complexes is the switching between different EET pathways in PSI [94].

However, the attempts to re-fit the data with the parameters changed according to the cooperative effect hypothesis were unsuccessful. Instead of trying to find the correct combination of parameters by trial and error, one can produce some sort of a parameter space, introduce all possible constraints derivable from the experimental data, and narrow the range of possible fit parameters. In order to do so, one can start from the thermocycling data in Figure 5.16.

According to Figure 5.16, barrier-hopping probably sets in at 10 K (red oval) and is definitely present at 13 K. Since $\sqrt{T} \backsim \sqrt{V} \backsim \lambda$, barrier hopping in the ground state starting from $\backsim$ 10 K means that $\lambda_{ground,min} = c \times 3.16$. In addition, recovery is complete by $\backsim$ 52 K (orange oval) meaning $\lambda_{ground,max} = c \times 7.2$, where c is the same constant for both $\lambda_{ground,min}$ and

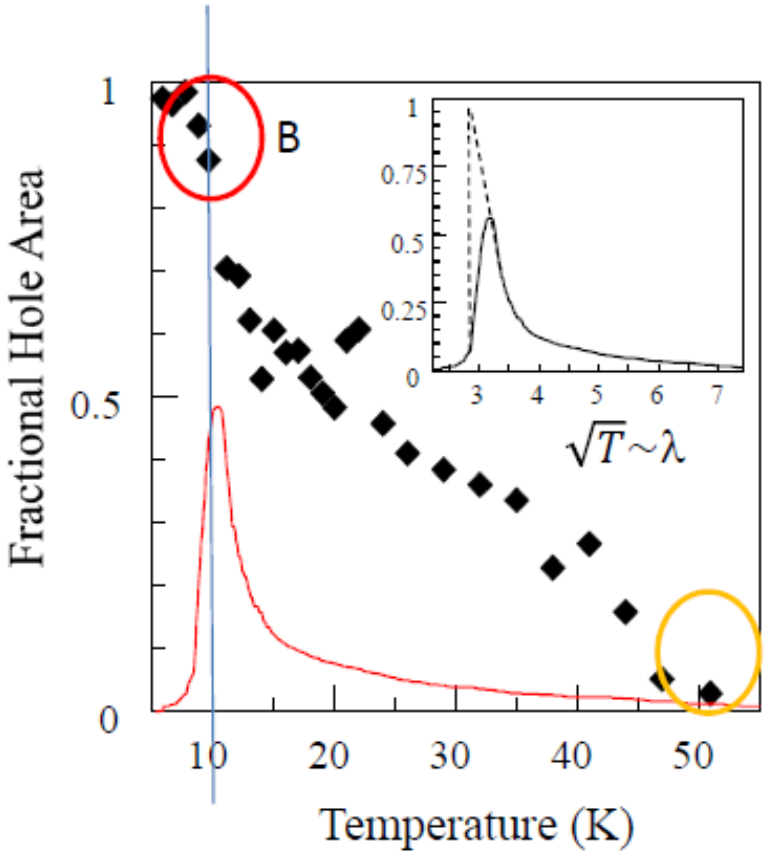

FIGURE 5.16: Black diamonds: Recovery of a 30%-deep hole due to thermocycling corrected for recovery that would occur at 5.5 K anyway (Cyt b_6f sample in protonated environment). Red curve: the distribution of barriers V corresponding to the recovery data. Inset: distribution as a function of $\sqrt{T} \backsim \sqrt{V} \backsim \lambda$. Red oval: barrier-hopping probably starts at 10 K. Orange oval: Recovery is completed by $\backsim$ 52 K.

$\lambda_{ground,max}$. Therefore, $\lambda_{ground,max}/\lambda_{ground,min} = 7.2/3.16 = 2.28$, which is insensitive to the attempt frequency. We set the tunneling and barrier-hopping rates at 10 K to be equal, in the following way:

$$exp(-2\lambda) = exp(ln2)exp(\frac{-\lambda^2\hbar^2}{2md^2k_BT}) \tag{5.7}$$

$$\Rightarrow 2\lambda = \frac{\lambda^2\hbar^2}{2md^2k_BT} - ln2 \tag{5.8}$$

$$\Rightarrow md^2 = \frac{\lambda^2\hbar^2}{2k_BT(2\lambda + ln2)} \tag{5.9}$$

It should be noted that the extra factor of 2 = exp(ln2) for hopping rate was not present in the original published paper [37] (but is present in the updated version above). According to [95], the rate with which populations go to equilibrium in a two-state system is the sum of the rates of back- and forth- barrier hopping. On the other hand, from the last equation one can see that for most of the realistic λ range this $ln2$ introduces very minor correction. Besides, this correction will be fully or partially compensated by the small increase of tunneling rate for large ground state asymmetry. Figure 5.17 shows the parameter space of md^2 and λ. The diagonal lines in this figure are almost straight, indicating near linear relationship between md^2 and λ.

In addition, according to Equation 4.11 for the NPHB yield, one can simultaneously change the attempt frequency Ω_0 and the parameters of the λ-distribution in such way that the NPHB yield will not be affected. Specifically, the width of the excited state λ-distribution stays the same. Thus, regardless of the attempt frequency, the experimental data can be fitted keeping $\lambda_{exc,max}$ - $\lambda_{exc,min}$ = 4.05. Therefore, $k(\lambda_{exc,min}$ + 4.05) / $k\lambda_{exc,min}$ = 2.28 , where k is the scaling factor between λ-distributions in ground and excited states (Earlier, k = 2.35 was used in this study and in the paper.). Therefore, $\lambda_{exc,min}$ = 3.16 which indicates that λ is reduced by 5. Reduction of all λ by 5 corresponds to change in attempt frequency by exp(10) = 22000, i.e. from 7.6 × 10^{12} Hz to 345 MHz.

Figure 5.17 represents the relevant parameter space. The first black diagonal line corresponds to $\lambda_{ground,min}$ according to Equation 5.9 with T=10 K (and attempt frequencies for tunneling and hopping being equal). The second black line corresponds to $\lambda_{ground,max}$ = 2.28 $\lambda_{ground,min}$. Two blue diagonal lines with larger slope separated by $\Delta\lambda$ = 4 represent $\lambda_{exc,max}$ and $\lambda_{exc,min}$ in the case when barrier hopping in the excited state starts at 4 K already (too early compared to HGK results). The orange oval represents the uncorrected parameters from the original paper [37].

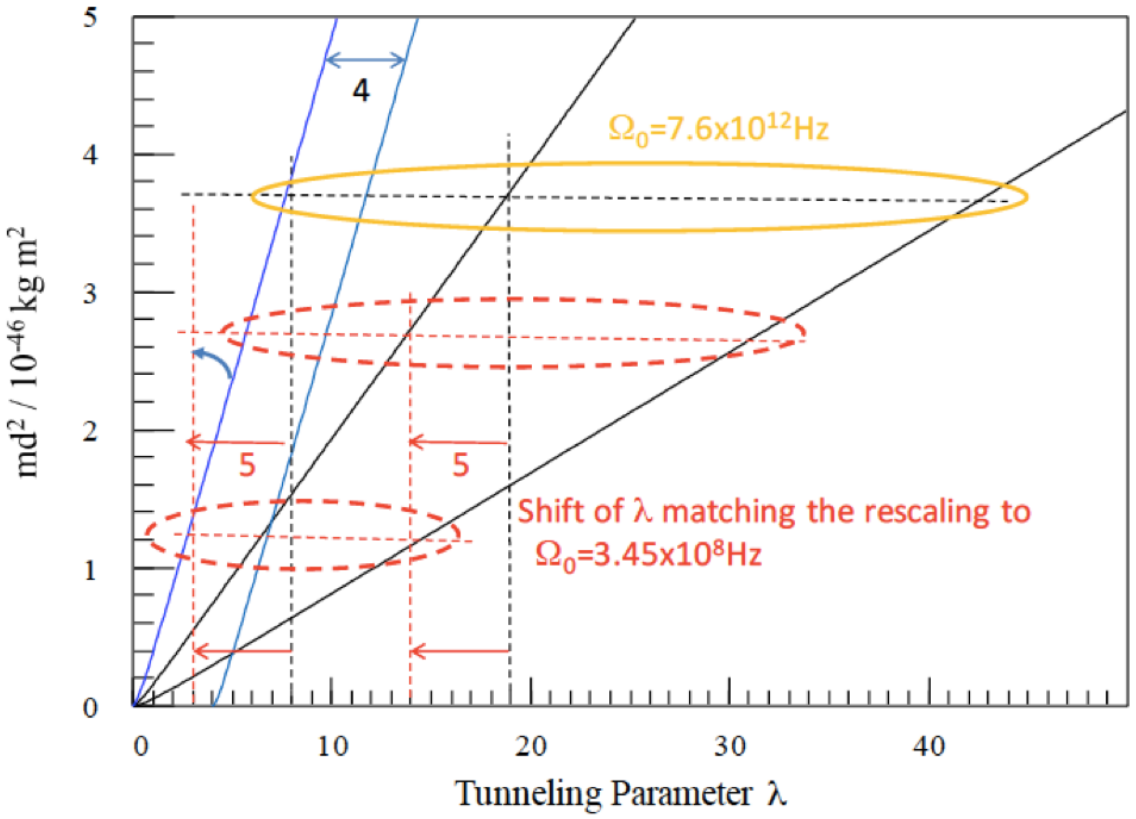

FIGURE 5.17: Parameter Space with Possible Ranges of md^2 and λ

These parameters correspond to $md^2 \backsim 3.7 \times 10^{-46}\ kg{\cdot}\mathrm{m}^2$. Obviously, these parameters do not work, as for such a large md^2 one would observe too fast recovery upon thermocycling. The lower red oval contains the parameters resulting from rescaling the excited state λ-distributions as described in the paper, i.e. assuming that scaling factor k between λ-distributions in ground and excited states is a constant. From the figure above one can see that the meaning of this scaling factor k is, roughly, the ratio of temperatures when barrier-hopping starts to dominate in ground and excited state, respectively (in Figure 5.17, k =10 K/4 K = 2.5). Discrepancies between the numbers here and in the paper so far are only due to more precise determination of $\lambda_{ground,min}$: Figure 5.18 depicts fictitious but reasonably realistic partial λ-distribution (the distribution actually encoded into the hole) for the ground state as well as matching q-curves (given by Equation 4.27) for 60 sec, 300 sec, 1 hour and 2 hours at 5 K (i.e. dominated by

tunneling). The relationship between the partial distribution and the q-curves is dictated by the following considerations:

1. Fixed temperature recovery in the first 60 seconds is negligible (black q-curve; hole depths from HGK and from the first hole are similar within couple percent.).

2. Some recovery occurs in the first 300 seconds (blue q-curve; second hole is smaller with respect to the first).

3. After two hours and $\backsim$ 20-25% recovery (green curve), there are still some unrecovered systems with $\lambda_{ground,min}$; so the initial λ is the same for fixed-temperature recovery and for thermocycling, at least in the case of full true λ-distributions being uniform.

In order to successfully fit the fixed-temperature hole recovery after changing the attempt frequency to 345 MHz, it is required to shift $\lambda_{ground,min}$ by 5 units.(i.e. by the same amount we shifted the whole excited state λ-distribution.) It can be immediately seen that the resulting range of parameters (the upper red oval in Figure 5.17) is not the same as represented by the lower red oval. The only way to make those ovals to match is to suggest that barrier hopping turns on as early as at 2 K in the excited state. Since the hopping rate will increase with temperature exponentially, this would be incompatible with modest increase of the NPHB yield observed between 2 and 13 K. In fact, from HGK data one can conclude that barrier hopping in the excited state becomes somewhat visible at around 8-9 K.

Thus, we have to re-evaluate the assumptions of the model presented in the original paper [37]. One or more of the following may be true, from more likely to less likely:

1. $\lambda_{ground}/\lambda_{exc}$ is not constant; $k = \lambda_{ground}/\lambda_{exc}$ is a function of λ (or barrier height), increasing with the increase of λ. It should be noted that the $k = const$ assumption was justified only by qualitative argument (excited state landscape should resemble the

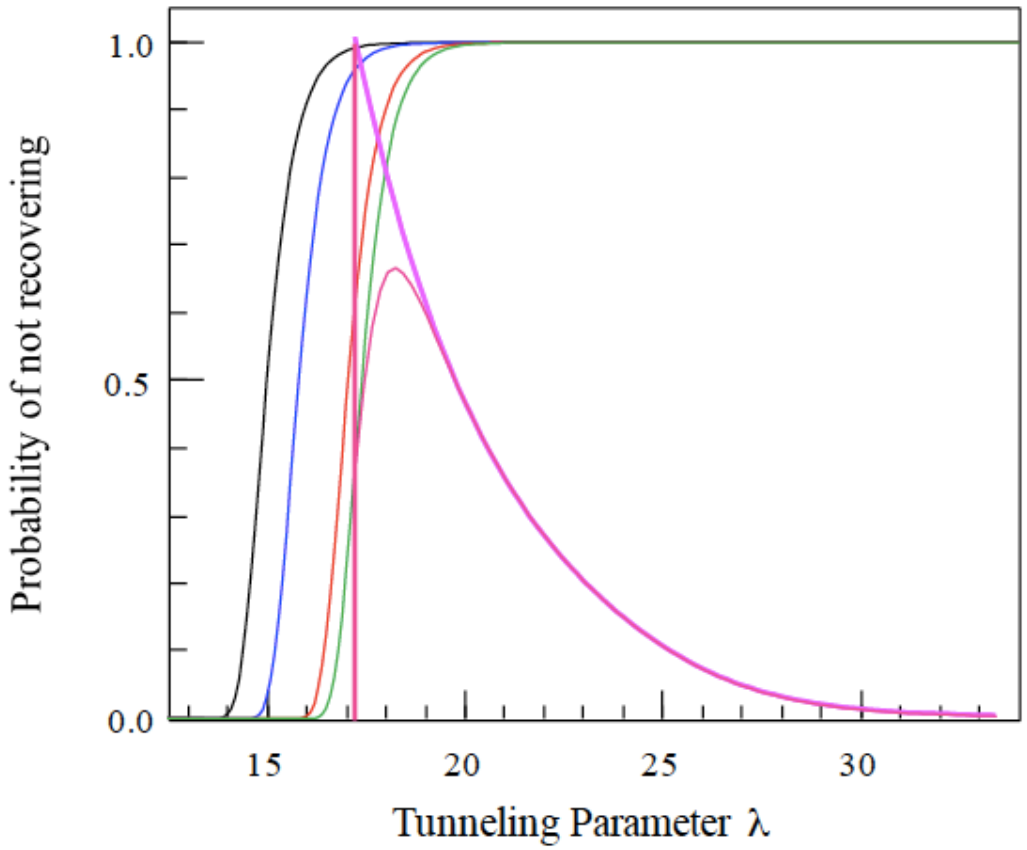

FIGURE 5.18: Partial λ-distributions for the ground state right after hole burning (thick magneta line) and after 2 hours of recovery (thin magneta line), as well as matching q-curves (given by Equation 4.27) for 60 sec (black), 300 sec (blue), 1 hour (red) and 2 hours (green) at 5 K and for the attempt frequency of $1 \times 10^{11}\ Hz$.

ground state landscape) that was working well for the beginning part of fixed-temperature recovery (i.e. the only available part). There is no reason why similarity should mean simple perfect proportionality. In fact, lowest barriers in the excited state still correspond to the lowest barriers in the ground state, and so on. The higher λ / higher barrier tail of the distribution is just stretched, in agreement with the insert of Figure 5.16.

2. Significantly different attempt frequencies for tunneling and barrier hopping. It is not clear why these frequencies should be different at all, given that both processes are occurring on the same landscape / TLS. Besides, up to an order of magnitude difference in attempt frequencies will have very small effect on Figure 5.17; including different attempt

frequencies results in additional term $\ln(\Omega_{0,hopping}/\Omega_{0,tunneling})$ added to ln2 in Equation 5.9.

3. Some memory-less fraction of recovery is actually present. However, this disagrees with nearly perfect fit for the beginning of the fixed temperature recovery by 100% spectral memory model.

Once we abolish the requirement that $k = \lambda_{ground}/\lambda_{exc} = const$, extreme reduction of the attempt frequency becomes unnecessary (the 4-5 orders of magnitude reduction discussed above is not completely unrealistic, but still bold.). Thus, the real range of parameters is likely somewhere between the orange and upper red ovals in Figure 5.17. This, in turn, suggests 2.7-3.6 $\times$ 10^{-46} $kg{\cdot}\mathrm{m}^2$ for proper md^2 range, i.e. significantly larger than in the original paper [37].

The md^2 = 2.7-3.6 $\times$ 10^{-46} $kg{\cdot}\mathrm{m}^2$ effectively rules out the tunneling of a single proton in the double-well potential associated with a hydrogen bond. Cooperative effects involving several protons or the large hydrogen bonds network of the protein are still possible, since in the case of the cooperative effects m becomes uncoupled from the mass of some one particular atom or chemical group. For a single methyl or a hydroxyl group $md^2 \backsim 3.0 \times 10^{-46}$ $kg{\cdot}\mathrm{m}^2$ would lead to d = 1.09 or 1.02 $\mathring{A}$, respectively.

Furthermore, the results obtained for Cytochrome b_6f in deuterated environment rule out only the possibility that observed dynamics is specifically due to proton tunneling in the outside environment. Since $\lambda \backsim \sqrt{m}$, increasing m by a factor of 2 results in the increase of λ by a factor of $\sqrt{2}$. Depending on the range of λ, the HB yield is expected to be reduced 50-1000 times. The methyl groups change their mass upon deuteration from 15 to 18 g/mol and changes in their tunneling dynamics may be noticeable, but they are not present in the outside environment composed of water and glycerol. However, The mass of the -OH group changes only by 6%. The change of dynamics involving whole -OH groups may easily go unnoticed, especially in the smaller λ range. Thus, the lack of deuterium effects in Cytochrome b_6f samples does not

prove that we are not dealing with the dynamics of the -OH groups of the environment. Given that in the water/glycerol mixture the burning rate did not significantly depend on deuteration, the possibility that the hole burning dynamics of water/glycerol mixture is dominated by the -OH groups rearrangement is quite real. Thus, presence of strong quenching in solution and its absence in protein is stronger argument against chlorophyll in protein being exposed to water/glycerol (and therefore exhibiting glassy dynamics) than the lack of deuteration effects.

5.4.3 Distribution Shape

Is there a way to reconcile the observations for Cyt b_6f and CP43 [38] in terms of the qualitative shapes of the barrier distributions? A superposition of Gaussian and $\backsim 1/\sqrt{V}$ terms was observed in a thermocycling experiment on phycobilisomes [60]. The results presented here also may be explained by assuming complex shape of the true full λ-distribution which is roughly 85% uniform (box-like) and 15% Gaussian. (This would account for faster initial stages of burning and recovery.) Note that it is not clear why distinct λ_{min} and λ_{max} (V_{min} and V_{max}) should exist in an amorphous system. One could think of the true λ-distribution functions with a flattened center and relatively narrow tails approaching zero asymptotically. If such a complex distribution is narrow enough, the hole behavior may be dominated by the Gaussian-like tails, while if such a distribution is broad, flat central part would play an increasing role. It remains to be seen if there is a correlation between the degree of disorder (larger inhomogeneous width and / or larger overall width of the λ-distribution) and the tendency of the holes to obey uniform λ-distribution rather than a Gaussian one. Alternatively, one can speculate that Gaussian barrier distributions of CP43 [38] are a direct result of a significant excitonic character of the lowest-energy state [62], [63] (A-state [72]). In this scenario each Chl contributing to the A-state experiences box-like or nearly box-like distribution of λ, similar to that in Cyt b_6f but the weighted sum of several such distributions may look Gaussian enough. (Imagine a typical histogram approximated by the normal distribution from an introductory

probability course.) Confirming any of these scenarios will have implications for determining the limits of applicability of the theories of amorphous solids at low temperatures to proteins.

5.5 Concluding Remarks

Results presented in this study indicate that barrier distributions in Cyt b_6f are proportional to $1/\sqrt{V}$. Cytochrome results are thus the exact opposite of what was reported in the case of CP43 [38], and similar to the distributions observed in thermocycling experiments in glasses [32], [59], [60]. As discussed above, it is very unlikely that Chls explored in this study were released by the partially denatured protein and surrounded by the glassy solvent. This would contradict the presence of the EET between the two Chls of the dimer with the rate following from the structure data of intact Cyt b_6f [12], as demonstrated in Figure 5.3. Furthermore, the presence of quenching when the Chls are exposed to the surrounding solvent confirms that Chls of Cyt b_6f are well screened from the solvent.

Quantitatively, the parameters of the excited and ground-state distributions are also typical for pigment-protein complexes and not for pigments in organic glasses [76], [35], [77]. Thus, the suggestion voiced in the Introduction of [37], that all amorphous solids or at least all proteins may possess only Gaussian barrier distributions [38], was not confirmed. Spectral dynamics of Cytochrome b_6f manifesting in NPHB experiments appears to be independent of the deuteration of the buffer/glycerol glassy matrix containing the protein (apart from the differences in heat dissipation). Several different estimates for the md^2 parameter characterizing tunneling entities were presented. md^2 more likely has values in the range of 2.7-3.6 $\times$ 10^{-46} $kg{\cdot}\mathrm{m}^2$. A tempting explanation alternative to attributing the NPHB and recovery to the tunneling of some one particular entity involves cooperative effects resulting in a significant decrease of the attempt frequency. In other words, the only way to have a large md^2 with protons as the tunneling entities is to have cooperative effects. Or, alternatively, the tunneling entities are some side

groups (most likely the whole -OH groups) instead of protons. The differences in heat dissipation are most consistent with the presence of high interface thermal resistivity between (protonated) protein and deuterated outside environment, likely due to phonon frequency mismatch.

Chapter 6

Conclusions and Outlook

Spectral hole burning (SHB) as an optical line narrowing technique was employed to study the dynamics and energy landscape of Cytochrome b_6f, which is a protein complex involved in photosynthesis. According to the results presented in Chapter 5, barrier distributions in Cyt b_6f are proportional to $1/\sqrt{V}$, and not to Gaussian that was previously observed in CP43 in [38]. The $1/\sqrt{V}$ shape of barrier distributions in Cyt b_6f is similar to the distributions observed in glasses [32], [59], [60]. In addition, the value of md^2 parameter characterizing tunneling entities seems to be more likely in the range of 2.7-3.6 $\times$ 10^{-46} $kg{\cdot}\mathrm{m}^2$. The observed results in Cyt b_6f were confirmed by performing similar experiments on Cyt b_6f dissolved in deuterated buffer-glycerol matrix and on Chlorophyll in solution (without protein) (See Discussion and Concluding Remarks in Chapter 5.3.).

As for future work, searching for detailed understanding, on an atomic level, of factors possibly leading to the attempt frequencies as low as 100 MHz is an interesting research topic. In addition, one can perform similar experiments on other pigment-protein complexes to explore the possibility of having a correlation between the degree of disorder (larger inhomogeneous width and / or larger overall width of the λ-distribution) and the tendency of the holes to obey

uniform λ-distribution (observed in Cyt b_6f) rather than a Gaussian one (observed in Cp43 [38]). For this purpose, LH2 [53], [57], [74] (an antenna pigment-protein complex from purple bacteria) or CP29 [58], [50] (one of the antenna pigment-protein complexes of Photosystem II) can be good options. Furthermore, one could continue performing similar experiments on chlorophyll dissolved in buffer-glycerol matrix (without protein) and explore its behaviour when it is in direct contact with solvent in more details.

Bibliography

[1] D. Thorn Leeson, D. A. Wiersma, K. Fritsch, and J. Friedrich, "The Energy Landscape of Myoglobin: An Optical Study," *The Journal of Physical Chemistry B*, vol. 101, no. 33, pp. 6331–6340, 1997.

[2] P. Fromme and I. Grotjohann, "Overview of Photosynthesis," in *Photosynthetic Protein Complexes*, pp. 1–22, Wiley-VCH Verlag GmbH & Co. KGaA, 2008.

[3] "File:Z-scheme.png - Wikipedia, the free encyclopedia." [Online] . Available: https://commons.wikimedia.org/wiki/File:Z-scheme.png [Accessed: 14-Dec-2015].

[4] "File:Simple photosynthesis overview.svg - Wikimedia Commons." [Online] . Available: https://commons.wikimedia.org/wiki/File:Simple_photosynthesis_overview.svg . [Accessed: 14-Dec-2015].

[5] R. Porra, W. Thompson, and P. Kriedemann, "Determination of accurate extinction coefficients and simultaneous equations for assaying chlorophylls a and b extracted with four different solvents: verification of the concentration of chlorophyll standards by atomic absorption spectroscopy," *Biochimica et Biophysica Acta (BBA) - Bioenergetics*, vol. 975, pp. 384–394, aug 1989.

[6] J. W. MacAdam, *Structure and function of plants*. John Wiley & Sons, 2011.

[7] "PhotochemCAD Chemicals." [Online] . Available: http://omlc.org/spectra/PhotochemCAD/index.html. [Accessed: 13-Jan-2016].

[8] W. Junge and N. Nelson, "ATP Synthase," *Annual Review of Biochemistry*, vol. 84, no. 1, pp. 631–57, 2015.

[9] A. Guskov, J. Kern, A. Gabdulkhakov, M. Broser, A. Zouni, and W. Saenger, "Cyanobacterial photosystem II at 2.9-A resolution and the role of quinones, lipids, channels and chloride," *Nat Struct Mol Biol*, vol. 16, no. 3, pp. 334–342, 2009.

[10] L. Yarris, "Research News: Berkeley Researchers Identify Photosynthetic Dimmer Switch." [Online] . Available: http://www.lbl.gov/Science- Articles/Archive/PBD-CP29.html. [Accessed: 25-Jan-2016].

[11] B. Jagannathan and J. H. Golbeck, "Photosynthesis: Microbial," *Encyclopedia of Microbiology (Third Edition)*, pp. 325–341, 2009.

[12] E. Yamashita, H. Zhang, and W. A. Cramer, "Structure of the Cytochrome b_6f Complex: Quinone Analogue Inhibitors as Ligands of Heme c_n," *Journal of Molecular Biology*, vol. 370, no. 1, pp. 39–52, 2007.

[13] E. J. Peterman, S. O. Wenk, T. Pullerits, L. O. Pâlsson, R. van Grondelle, J. P. Dekker, M. Rögner, and H. van Amerongen, "Fluorescence and absorption spectroscopy of the weakly fluorescent chlorophyll a in cytochrome b_6f of Synechocystis PCC6803.," *Biophysical journal*, vol. 75, no. 1, pp. 389–398, 1998.

[14] N. Dashdorj, H. Zhang, H. Kim, J. Yan, W. a. Cramer, and S. Savikhin, "The single chlorophyll a molecule in the cytochrome b_6f complex: unusual optical properties protect the complex against singlet oxygen.," *Biophysical journal*, vol. 88, no. 6, pp. 4178–4187, 2005.

[15] J. Yan, N. Dashdorj, D. Baniulis, E. Yamashita, S. Savikhin, and W. A. Cramer, "On the structural role of the aromatic residue environment of the chlorophyll a in the cytochrome b_6f complex," *Biochemistry*, vol. 47, no. 12, pp. 3654–3661, 2008.

[16] J. M. Berg, J. L. Tymoczko, and L. Stryer, *Biochemistry*. W. H. Freeman, 2007.

[17] G. Tomita and E. Rabinowitch, "Excitation energy transfer between pigments in photosynthetic cells.," *Biophysical journal*, vol. 2, no. 6, pp. 483–499, 1962.

[18] R. Croce and H. van Amerongen, "Natural strategies for photosynthetic light harvesting," *Nature Chemical Biology*, vol. 10, no. 7, pp. 492–501, 2014.

[19] J. R. Lakowicz, *Principles of fluorescence spectroscopy*. Springer Science & Business Media, 2013.

[20] D. C. Harris, *Quantitative Chemical Analysis*. W. H. Freeman, 2010.

[21] R. M. Clegg, "Chapter 1 förster resonance energy transfer—fret what is it, why do it, and how it's done," in *Fret and Flim Techniques*, vol. 33 of *Laboratory Techniques in Biochemistry and Molecular Biology*, pp. 1 – 57, Elsevier, 2009.

[22] R. E. Blankenship, D. M. Tiede, J. Barber, G. W. Brudvig, G. Fleming, M. Ghirardi, M. R. Gunner, W. Junge, D. M. Kramer, A. Melis, T. a. Moore, C. C. Moser, D. G. Nocera, A. J. Nozik, D. R. Ort, W. W. Parson, R. C. Prince, and R. T. Sayre, "Comparing photosynthetic and photovoltaic efficiencies and recognizing the potential for improvement.," *Science (New York, N.Y.)*, vol. 332, no. 6031, pp. 805–9, 2011.

[23] I. McConnell, G. Li, and G. W. Brudvig, "Energy conversion in natural and artificial photosynthesis.," *Chemistry & biology*, vol. 17, no. 5, pp. 434–47, 2010.

[24] J. M. Berg, J. L. Tymoczko, and L. Stryer, "Biochemistry," 2002.

[25] S. B. Prusiner, "Prion diseases and the BSE crisis.," *Science (New York, N.Y.)*, vol. 278, pp. 245–51, oct 1997.

[26] H. Frauenfelder, F. Parak, and R. D. Young, "Conformational substates in proteins.," *Annual review of biophysics and biophysical chemistry*, vol. 17, pp. 451–479, 1988.

[27] R. H. Austin, K. W. Beeson, L. Eisenstein, H. Frauenfelder, and I. C. Gunsalus, "Dynamics of ligand binding to myoglobin.," *Biochemistry*, vol. 14, no. 24, pp. 5355–5373, 1975.

[28] J. Friedrich, *Biochemical Spectroscopy*, vol. 246 of *Methods in Enzymology*. Elsevier, 1995.

[29] P. w. Anderson, B. I. Halperin, and c. M. Varma, "Anomalous low-temperature thermal properties of glasses and spin glasses," *Philosophical Magazine*, vol. 25, no. 1, pp. 1–9, 1972.

[30] U. Störkel, T. Creemers, F. Hartog, and S. Völker, "Glass versus protein dynamics at low temperature studied by time-resolved spectral hole burning," *Journal of Luminescence*, vol. 76-77, no. 97, pp. 327–330, 1998.

[31] "Hole Burning Spectroscopy -Glass properties." [Online] . Available: http://www.isan.troitsk.ru/dms/les_lab/activity/holeburn/sd/intro.htm. [Accessed: 09-Feb-2016].

[32] W. Köhler and J. Friedrich, "Distribution of barrier heights in amorphous organic materials," *Phys. Rev. Lett.*, vol. 59, pp. 2199–2202, Nov 1987.

[33] W. W. Parson, *Modern Optical Spectroscopy*, ch. Electronic Absorption, pp. 109–188. Berlin, Heidelberg: Springer Berlin Heidelberg, 2007.

[34] A. Rebane, "Principles of Persistent Spectral Hole Burning. Montana State University." [Online] . Available: http://www.physics.montana.edu/arebane/research/tutorials/hole_burning/. [Accessed: 16-March-2016].

[35] T. Reinot and G. J. Small, "Modeling of dispersive nonphotochemical hole growth kinetics data: Al-phthalocyanine tetrasulphonate in hyperquenched glassy water," *Journal of Chemical Physics*, vol. 113, no. 22, pp. 10207–10214, 2000.

[36] S. M. N. Shooshtari, *Modeling and Characterization of Protein Energy Landscape at Low Temperature using Spectral Hole Burning Spectroscopy.* PhD thesis, Concordia University, August 2013.

[37] M. Najafi, N. Herascu, G. Shafiei, R. Picorel, and V. Zazubovich, "Conformational Changes in Pigment–Protein Complexes at Low Temperatures—Spectral Memory and a Possibility of Cooperative Effects," *The Journal of Physical Chemistry B*, vol. 119, no. 23, pp. 6930–6940, 2015.

[38] M. Najafi, N. Herascu, M. Seibert, R. Picorel, R. Jankowiak, and V. Zazubovich, "Spectral hole burning, recovery, and thermocycling in chlorophyll-protein complexes: distributions of barriers on the protein energy landscape," *Journal of Physical Chemistry B*, vol. 116, no. 38, pp. 11780–11790, 2012.

[39] R. Jankowiak and G. J. Small, "Hole-burning spectroscopy and relaxation dynamics of amorphous solids at low temperatures.," *Science (New York, N.Y.)*, vol. 237, pp. 618–25, aug 1987.

[40] J. Hayes, G. Small, and P. H. Burning, "Photochemical hole burning and strong electron-phonon coupling: primary donor states of reaction centers of photosynthetic bacteria," *J Phys Chem*, vol. 42, no. 12, pp. 4928–4931, 1986.

[41] J. M. Hayes, R. Jankowiak, and G. J. Small, *Persistent Spectral Hole-Burning: Science and Applications*, ch. Two-Level-, pp. 153–202. Berlin, Heidelberg: Springer Berlin Heidelberg, 1988.

[42] J. Jäckle, L. Piché, W. Arnold, and S. Hunklinger, "Elastic effects of structural relaxation in glasses at low temperatures," *Journal of Non-Crystalline Solids*, vol. 20, no. 3, pp. 365–391, 1976.

[43] W. A. Phillips, *Amorphous solids: low-temperature properties*. Springer-Verlag, 1981.

[44] N. C. Dang, T. Reinot, M. Reppert, and R. Jankowiak, "Temperature dependence of hole growth kinetics in aluminum-phthalocyanine- tetrasulfonate in hyperquenched glassy water," *Journal of Physical Chemistry B*, vol. 111, no. 7, pp. 1582–1589, 2007.

[45] N. Herascu, S. Ahmouda, R. Picorel, M. Seibert, R. Jankowiak, and V. Zazubovich, "Effects of the Distributions of Energy or Charge Transfer Rates on Spectral Hole Burning in Pigment–Protein Complexes at Low Temperatures," *The Journal of Physical Chemistry B*, vol. 115, no. 50, pp. 15098–15109, 2011.

[46] S. Love and A. Sievers, "Persistent infrared spectral hole burning of the sulfur—hydrogen vibrational mode in hydrogenated As_2S_3 glass," *Chemical Physics Letters*, vol. 153, pp. 379–384, dec 1988.

[47] J. Pieper and A. Freiberg, *The Biophysics of Photosynthesis, Edited by John Golbeck and Art van der Est*, ch. Electron–Phonon and Exciton–Phonon Coupling in Light Harvesting, Insights from Line-Narrowing Spectroscopies, pp. 45–77. New York, NY: Springer New York, 2014.

[48] W. Yen and R. Brundage, "Fluorescence line narrowing in inorganic glasses: linewidth measurements," *Journal of luminescence*, vol. 36, no. 4, pp. 209–220, 1987.

[49] M. Reppert, V. Naibo, and R. Jankowiak, "Accurate modeling of fluorescence line narrowing difference spectra: Direct measurement of the single-site fluorescence spectrum," *Journal of Chemical Physics*, vol. 133, no. 1, 2010.

[50] M. Rätsep, J. Pieper, K. D. Irrgang, and A. Freiberg, "Excitation wavelength-dependent electron-phonon and electron-vibrational coupling in the CP29 antenna complex of green plants," *Journal of Physical Chemistry B*, vol. 112, no. 1, pp. 110–118, 2008.

[51] H. Frauenfelder, S. Sligar, and P. Wolynes, "The energy landscapes and motions of proteins," 1991.

[52] P. W. Fenimore, H. Frauenfelder, B. H. McMahon, and R. D. Young, "Proteins are paradigms of stochastic complexity," *Physica A: Statistical Mechanics and its Applications*, vol. 351, no. 1, pp. 1–13, 2005.

[53] C. Hofmann, T. J. Aartsma, H. Michel, and J. Köhler, "Direct observation of tiers in the energy landscape of a chromoprotein: a single-molecule study.," *Proceedings of the National Academy of Sciences of the United States of America*, vol. 100, no. 26, pp. 15534–15538, 2003.

[54] Y. Berlin, A. Burin, J. Friedrich, and J. Köhler, "Low temperature spectroscopy of proteins. Part II: Experiments with single protein complexes," *Physics of Life Reviews*, vol. 4, no. 1, pp. 64–89, 2007.

[55] Y. Berlin, A. Burin, J. Friedrich, and J. Köhler, "Spectroscopy of proteins at low temperature. Part I: Experiments with molecular ensembles," *Physics of Life Reviews*, vol. 3, no. 4, pp. 262–292, 2006.

[56] R. Jankowiak, J. M. Hayes, and G. J. Small, "Spectral hole-burning spectroscopy in amorphous molecular solids and proteins," *Chemical Reviews*, vol. 93, no. 4, pp. 1471–1502, 1993.

[57] D. Grozdanov, N. Herascu, T. Reinot, R. Jankowiak, and V. Zazubovich, "Low-temperature protein dynamics of the B800 molecules in the LH2 light-harvesting complex: Spectral hole

burning study and comparison with single photosynthetic complex spectroscopy," *Journal of Physical Chemistry B*, vol. 114, no. 10, pp. 3426–3438, 2010.

[58] N. Herascu, M. Najafi, A. Amunts, J. Pieper, K. D. Irrgang, R. Picorel, M. Seibert, and V. Zazubovich, "Parameters of the protein energy landscapes of several light-harvesting complexes probed via spectral hole growth kinetics measurements," *Journal of Physical Chemistry B*, vol. 115, no. 12, pp. 2737–2747, 2011.

[59] W. Köhler, J. Meiler, and J. Friedrich, "Tunneling dynamics of doped organic low-temperature glasses as probed by a photophysical hole-burning system," *Physical Review B*, vol. 35, no. 8, pp. 4031–4037, 1987.

[60] W. Köhler, J. Friedrich, and H. Scheer, "Conformational barriers in low-temperature proteins and glasses," *Physical Review A*, vol. 37, no. 2, pp. 660–662, 1988.

[61] W. A. Phillips, "Tunneling states in amorphous solids," *Journal of Low Temperature Physics*, vol. 7, no. 3-4, pp. 351–360, 1972.

[62] N. C. Dang, V. Zazubovich, M. Reppert, B. Neupane, R. Picorel, M. Seibert, and R. Jankowiak, "The CP43 proximal antenna complex of higher plant photosystem II revisited: Modeling and hole burning study. I," *Journal of Physical Chemistry B*, vol. 112, no. 32, pp. 9921–9933, 2008.

[63] M. Reppert, V. Zazubovich, N. C. Dang, M. Seibert, and R. Jankowiak, "Low-energy chlorophyll states in the CP43 antenna protein complex: Simulation of various optical spectra. II," *Journal of Physical Chemistry B*, vol. 112, no. 32, pp. 9934–9947, 2008.

[64] E. Romanowska, "Isolation of cytochrome b_6f complex from grana and stroma membranes from spinach chloroplasts.," *Methods in molecular biology (Clifton, N.J.)*, vol. 684, pp. 53–64, jan 2011.

[65] Y. Pierre, C. Breyton, D. Kramer, and J. L. Popot, "Purification and characterization of the cytochrome b_6f complex from Chlamydomonas reinhardtii," *J. Biol. Chem.*, vol. 270, no. 49, pp. 29342–29349, 1995.

[66] I. P. Zharkov, A. N. Ivashchenko, S. V. Pogrebnjak, and V. V. Safronov, "Optimization of Temperature Control in Liquid Flow Cryostats.," *Ukr. J. Phys.*, vol. 55, no. 3, pp. 350–355, 2010.

[67] V. Zazubovich, "Fluorescence line narrowing and Δ-FLN spectra in the presence of excitation energy transfer between weakly coupled chromophores," *Journal of Physical Chemistry B*, vol. 118, no. 47, pp. 13535–13543, 2014.

[68] A. Kell, X. Feng, M. Reppert, and R. Jankowiak, "On the shape of the phonon spectral density in photosynthetic complexes," *Journal of Physical Chemistry B*, vol. 117, no. 24, pp. 7317–7323, 2013.

[69] J. M. Hayes, P. A. Lyle, and G. J. Small, "A Theory for the Temperature Dependence of Hole-Burned Spectra," *The Journal of Physical Chemistry*, vol. 98, pp. 7337–7341, jul 1994.

[70] M. Reppert, A. Kell, T. Pruitt, and R. Jankowiak, "Comments on the optical lineshape function: Application to transient hole-burned spectra of bacterial reaction centers," *Journal of Chemical Physics*, vol. 142, no. 9, 2015.

[71] N. Herascu, A. Kell, K. Acharya, R. Jankowiak, R. E. Blankenship, and V. Zazubovich, "Modeling of various optical spectra in the presence of slow excitation energy transfer in dimers and trimers with weak interpigment coupling: FMO as an example," *Journal of Physical Chemistry B*, vol. 118, no. 8, pp. 2032–2040, 2014.

[72] R. Jankowiak, V. Zazubovich, M. Rätsep, S. Matsuzaki, M. Alfonso, R. Picorel, M. Seibert, and G. J. Small, "The CP43 Core Antenna Complex of Photosystem II Possesses Two

Quasi-Degenerate and Weakly Coupled Q_y-Trap States," *The Journal of Physical Chemistry B*, vol. 104, no. 49, pp. 11805–11815, 2000.

[73] M. Rätsep, R. E. Blankenship, and G. J. Small, "Energy transfer and spectral dynamics of the three lowest energy Q(y)-states of the Fenna-Matthews-Olson antenna complex," *Journal of Physical Chemistry B*, vol. 103, no. 27, pp. 5736–5741, 1999.

[74] H. Wu, M. Ratsep, I. Lee, R. J. Cogdell, G. J. Small, and B. Ring, "Exciton Level Structure and Energy Disorder of the B850 Ring of the LH2 Antenna Complex," *Small*, vol. 5647, no. 97, pp. 7654–7663, 1997.

[75] F. T. H. Den Hartog, C. Van Papendrecht, U. Stoerkel, F. T. H. D. Hartog, C. V. Papendrecht, U. Sto, and S. Vo, "Protein Dynamics in Photosystem II Complexes of Green Plants Studied by Time-Resolved Hole-Burning," *Journal of Physical Chemistry B*, no. Ps Ii, pp. 1375–1380, 1999.

[76] T. Reinot, N. C. Dang, and G. J. Small, "A model for persistent hole burned spectra and hole growth kinetics that includes photoproduct absorption: Application to free base phthalocyanine in hyperquenched glassy ortho-dichlorobenzene at 5 K," *Journal of Chemical Physics*, vol. 119, no. 19, pp. 10404–10414, 2003.

[77] T. Reinot, J. M. Hayes, and G. J. Small, "Laser-induced hole filling and spectral diffusion of aluminum phthalocyanine tetrasulfonate in hyperquenched glassy films," *The Journal of Chemical Physics*, vol. 110, no. 10, pp. 4820–4827, 1999.

[78] H. Oikawa, S. Fujiyoshi, T. Dewa, M. Nango, and M. Matsushita, "How deep is the potential well confining a protein in a specific conformation? A single-molecule study on temperature dependence of conformational change between 5 and 18 K," *Journal of the American Chemical Society*, vol. 130, no. 14, pp. 4580–4581, 2008.

[79] S. P. Love, C. E. Mungan, A. J. Sievers, and J. A. Campbell, "Persistent infrared spectral hole burning of Tb^{3+} in the glasslike mixed crystal $Ba_{1-X-Y}La_xTb_yF_{2+x+y}$," *Journal of the Optical Society of America B*, vol. 9, no. 5, pp. 794–799, 1992.

[80] J. Baier, M. F. Richter, R. J. Cogdell, S. Oellerich, and J. Köhler, "Determination of the spectral diffusion kernel of a protein by single-molecule spectroscopy," *Physical Review Letters*, vol. 100, no. 1, pp. 1–4, 2008.

[81] W. Köhler and J. Friedrich, "Probing of conformational relaxation processes of proteins by frequency labeling of optical states," *The Journal of Chemical Physics*, vol. 90, p. 1270, jan 1989.

[82] W.-H. Kim, T. Reinot, J. M. Hayes, and G. J. Small, "Nonphotochemical hole burning in hyperquenched glassy films of water: A pronounced deuteration effect," *The Journal of Chemical Physics*, vol. 104, p. 6415, may 1996.

[83] T. Monks-Corrigan and H. Riesen, "Host deuteration effects in non-photochemical spectral hole-burning in the R1-line of [Cr(oxalate)3]3- in ethylene glycol/water," *Chemical Physics Letters*, vol. 419, no. 4-6, pp. 321–325, 2006.

[84] A. Lervik, F. Bresme, and S. Kjelstrup, "Heat transfer in soft nanoscale interfaces: the influence of interface curvature," *Soft Matter*, vol. 5, no. 12, p. 2407, 2009.

[85] L. Shu and G. J. Small, "On the mechanism of nonphotochemical hole burning of optical transitions in amorphous solids," *Chemical Physics*, vol. 141, pp. 447–455, mar 1990.

[86] M. Najafi and V. Zazubovich, "Monte Carlo Modeling of Spectral Diffusion Employing Multiwell Protein Energy Landscapes: Application to Pigment-Protein Complexes Involved in Photosynthesis.," *The journal of physical chemistry. B*, vol. 119, no. 25, pp. 7911–21, 2015.

[87] R. Kiyanagi, H. Kimura, M. Watanabe, Y. Noda, T. Mochida, and T. Sugawara, "Indication of Tunneling State of Hydrogen Atom in Hydrogen-Bonded Material 5-Bromo-9-hydroxyphenalenon Studied by X-ray and Neutron Diffractions," *Journal of the Physical Society of Japan*, vol. 77, p. 064602, jun 2008.

[88] W. Hamilton and J. A. Ibers, *Hydrogen bonding in solids*. Wa Benjamin, 1968.

[89] H. Frauenfelder, G. A. Petsko, and D. Tsernoglou, "Temperature-dependent X-ray diffraction as a probe of protein structural dynamics," *Nature*, vol. 280, pp. 558–563, aug 1979.

[90] R. Huber, "Flexibility and Rigidity of Proteins and Protein–Pigment Complexes," *Angewandte Chemie International Edition in English*, vol. 27, pp. 79–88, jan 1988.

[91] J. Zollfrank and J. Friedrich, "Spectral holes under pressure: proteins and glasses," *Journal of the Optical Society of America B*, vol. 9, p. 956, jun 1992.

[92] M. Brecht, H. Studier, V. Radics, J. B. Nieder, and R. Bittl, "Spectral diffusion induced by proton dynamics in pigment-protein complexes.," *Journal of the American Chemical Society*, vol. 130, pp. 17487–93, dec 2008.

[93] K. Fritsch, J. Friedrich, F. Parak, and J. Skinner, "Spectral diffusion and the energy landscape of a protein," *Proceedings of the National Academy of Sciences*, vol. 93, no. 26, pp. 15141–15145, 1996.

[94] M. Brecht, V. Radics, J. B. Nieder, and R. Bittl, "Protein dynamics-induced variation of excitation energy transfer pathways," *Proceedings of the National Academy of Sciences*, vol. 106, no. 29, pp. 11857–11861, 2009.

[95] P. Nelson, *Biological physics*. WH Freeman New York, 2004.